

Development and Implementation of Accelerated Multiple-Quantum-Filtered Sodium  
Magnetic Resonance Imaging Using Compressed Sensing at Ultra-High Field

Von der Medizinischen Fakultät  
der Rheinisch-Westfälischen Technischen Hochschule Aachen  
zur Erlangung des akademischen Grades einer Doktorin der Theoretischen Medizin  
genehmigte Dissertation

vorgelegt von

Qingping Chen  
aus Wenchang (China)

Berichter: Universitätsprofessor Dr. Dr. h.c. Nadim Jon Shah  
Privatdozentin Dr. med. Tanja Veselinovic

Tag der mündlichen Prüfung: 02.04.2025

***Diese Dissertation ist auf den Internetseiten der Universitätsbibliothek online verfügbar.***



Part of the work presented in this dissertation was previously published in Journal of Magnetic Resonance Imaging 2022, 55, 1340-1356, as Compressed Sensing in Sodium Magnetic Resonance Imaging: Techniques, Applications, and Future Prospects by Qingping Chen, N. Jon Shah, and Wieland A. Worthoff.

Part of the work presented in this dissertation was previously published in Magnetic Resonance Imaging, 2024, 107, 138-148, as Accelerated multiple-quantum-filtered sodium magnetic resonance imaging using compressed sensing at 7 T by Qingping Chen,\* Wieland A. Worthoff,\* and N. Jon Shah (\* co-first authors).



**ABSTRACT**

Sodium ( $^{23}\text{Na}$ ) plays a critical role in cellular metabolic processes via the regulation of the sodium-potassium pump, which maintains a large gradient between intracellular and extracellular sodium concentrations at the expense of energy. Cellular dysfunction can lead to an elevated intracellular sodium concentration, whereas the extracellular sodium concentration remains primarily unchanged due to tissue perfusion. Therefore, intracellular sodium, as a direct link to cell integrity and tissue viability, promises means for an insight into pathological processes.

Conventional sodium Magnetic Resonance Imaging (MRI) with a single radiofrequency pulse can only detect total sodium. Based on the quadrupolar nature of the sodium nucleus, an advanced technique, Multiple-Quantum-Filtered (MQF) sodium MRI, is proposed to monitor restricted (mainly intracellular) sodium. However, the clinical application of MQF sodium MRI is hampered by the relatively low image quality and associated long acquisition times.

This thesis aims to mitigate the limitations of MQF sodium MRI by exploiting two aspects: data acquisition and image reconstruction. Regarding data acquisition, this thesis optimised the enhanced SImultaneous Single-quantum and TrIple-quantum-filtered imaging of  $^{23}\text{Na}$  (SISTINA) sequence using a highly efficient non-Cartesian sampling scheme. Qualitative validation of this sequence optimisation was conducted by comparing the optimised sequence with a conventional enhanced SISTINA sequence in phantom measurements at 7T. The optimisation greatly improved the visual performance of ultra-short-echo-time images, while maintaining the visual quality of MQF images and introducing incoherence in raw data for the application of Compressed Sensing (CS) acceleration.

Regarding image reconstruction, this thesis applied CS to accelerate enhanced SISTINA acquisitions by exploiting image sparsity to compensate for incoherent undersampling artefacts. Quantitative validation of the CS acceleration was performed by comparing the undersampled CS-based reconstructions with fully sampled and undersampled standard Non-Uniform Fast Fourier Transform (NUFFT) reconstructions in both phantom and in vivo measurements at 7T. Compared to NUFFT, CS accelerated enhanced SISTINA by up to twofold at 7T in this study with reduced noise levels, while maintaining primary structural information, reasonable weightings towards total and compartmental sodium and relatively accurate in vivo quantification.



CONTENTS

<b>ABSTRACT.....</b>	<b>i</b>
<b>CONTENTS.....</b>	<b>iii</b>
<b>LIST OF FIGURES .....</b>	<b>vii</b>
<b>LIST OF TABLES .....</b>	<b>xi</b>
<b>LIST OF ABBREVIATIONS .....</b>	<b>xiii</b>
<b>1 Introduction and Outline .....</b>	<b>1</b>
<b>2 Physiological Significance of Sodium .....</b>	<b>7</b>
<b>2.1 Sodium in Health .....</b>	<b>7</b>
2.1.1 Membrane Transport – Active Role.....	7
2.1.2 Counter Ions – Passive Role .....	9
<b>2.2 Sodium in Disease .....</b>	<b>10</b>
2.2.1 Brain Diseases.....	10
2.2.2 Other Organ Diseases.....	12
<b>2.3 Motivation for Sodium Imaging.....</b>	<b>14</b>
<b>3 Nuclear Magnetic Resonance.....</b>	<b>15</b>
<b>3.1 Spin and Angular Momentum.....</b>	<b>15</b>
3.1.1 Rotational Angular Momentum .....	15
3.1.2 Spin Angular Momentum.....	17
3.1.3 Combining Angular Momenta .....	17
<b>3.2 Nuclear Spin.....</b>	<b>18</b>
3.2.1 Nuclear Spin States .....	18
3.2.2 Nuclear Zeeman Splitting .....	19
3.2.3 Nuclei with Various Spins .....	20
<b>3.3 Magnetism .....</b>	<b>21</b>
3.3.1 The Electromagnetic Field .....	21
3.3.2 Macroscopic Magnetism .....	21
3.3.3 Microscopic Magnetism.....	22
3.3.4 Spin Precession and Larmor Frequency.....	23
3.3.5 Spin-Lattice Relaxation: Nuclear Paramagnetism.....	24
3.3.6 Transverse Magnetisation and Transverse Relaxation .....	26
3.3.7 NMR Signal .....	27
<b>3.4 Spin-1/2 Dynamics .....</b>	<b>28</b>
3.4.1 Classical Description.....	28
3.4.2 Quantum Mechanical Description.....	30
<b>3.5 Spin-3/2 Dynamics .....</b>	<b>36</b>
3.5.1 Spin-3/2 Energy Levels.....	36
3.5.2 Spin-3/2 Density Matrix.....	37
3.5.3 Electric Quadrupolar Interaction .....	39
3.5.4 Relaxation Mechanisms of Spin-3/2 .....	44
<b>3.6 Physical Properties of Sodium in Biological Tissues .....</b>	<b>47</b>
<b>4 Magnetic Resonance Imaging .....</b>	<b>51</b>
<b>4.1 Scanner Structure.....</b>	<b>51</b>
<b>4.2 Imaging Principles.....</b>	<b>52</b>
4.2.1 Spatial Encoding: Gradient and K-space.....	53

## CONTENTS

---

4.2.2 Excitation in Presence and Absence of Gradients .....	55
4.2.3 Gradient Echoes and T2* .....	56
4.2.4 Data Acquisition Principle: Nyquist Sampling Criterion .....	57
4.2.5 Noise in MRI.....	63
<b>4.3 Data Acquisition .....</b>	<b>64</b>
4.3.1 MRI Sequence Definition: Gradient-Echo Sequence.....	64
4.3.2 Non-Cartesian Sampling .....	66
4.3.3 Ultra-short Echo Time Acquisition .....	71
4.3.4 Multiple-Quantum Filter: Phase Cycling .....	73
<b>4.4 Image Reconstruction.....</b>	<b>75</b>
4.4.1 Density Compensation .....	75
4.4.2 Standard Non-Cartesian Reconstruction: Gridding.....	76
4.4.3 Non-linear Iterative Reconstruction: Compressed Sensing .....	80
4.4.4 Reconstruction Performance Evaluation .....	85
<b>5 Multiple-Quantum-Filtered Sodium MRI at 7T: Optimisation of the Enhanced SISTINA Sequence Using FLORET K-space Trajectories.....</b>	<b>89</b>
<b>5.1 Introduction .....</b>	<b>89</b>
<b>5.2 Materials and Methods .....</b>	<b>90</b>
5.2.1 Multiple-Quantum Filter .....	90
5.2.2 Enhanced SISTINA Sequence Implementation .....	93
5.2.3 Data Acquisition .....	95
<b>5.3 Results.....</b>	<b>96</b>
<b>5.4 Discussion .....</b>	<b>97</b>
<b>5.5 Conclusion .....</b>	<b>98</b>
<b>6 Accelerated Enhanced Simultaneous Single-Quantum and Triple-Quantum-Filtered Sodium Magnetic Resonance Imaging Using Compressed Sensing at 7T .....</b>	<b>99</b>
<b>6.1 Introduction .....</b>	<b>99</b>
<b>6.2 Materials and Methods .....</b>	<b>100</b>
6.2.1 Optimised Enhanced SISTINA Sequence .....	100
6.2.2 Data Acquisition .....	101
6.2.3 Data Undersampling .....	102
6.2.4 Image Reconstruction.....	103
6.2.5 Image Segmentation.....	104
6.2.6 Image Evaluation .....	104
<b>6.3 Results.....</b>	<b>106</b>
6.3.1 Phantom Results.....	106
6.3.2 In Vivo Results.....	108
<b>6.4 Discussion .....</b>	<b>111</b>
<b>6.5 Conclusion .....</b>	<b>114</b>
<b>7 Conclusion .....</b>	<b>115</b>
7.1 Thesis Contribution.....	115
7.2 Future Research.....	116
<b>APPENDIX.....</b>	<b>117</b>
<b>REFERENCES.....</b>	<b>123</b>
<b>LIST OF PUBLICATIONS .....</b>	<b>135</b>
<b>ACKNOWLEDGEMENTS .....</b>	<b>137</b>



## CONTENTS

---

<b>AFFIDAVIT REGARDING DATA RETENTION .....</b>	<b>139</b>
<b>AFFIDAVIT REGARDING ONE’S OWN CONTRIBUTION .....</b>	<b>141</b>
<b>CURRICULUM VITAE.....</b>	<b>143</b>



LIST OF FIGURES

<b>Figure 2.1</b> Schematic representation of the sodium-potassium pump activity. The sodium-potassium pump maintains large sodium and potassium gradients across the cell membrane by moving three sodium ions out of the cell and simultaneously transferring two potassium ions into the cell. This process is powered by the hydrolysis of the third high-energy phosphate bond of adenosine triphosphate.....	8
<b>Figure 3.1</b> Schematic of the nuclear Zeeman sublevels of the $^1\text{H}$ , $^{15}\text{N}$ and $^{23}\text{Na}$ nuclear ground states. ....	20
<b>Figure 3.2</b> Schematic of thermal equilibrium. <b>(a)</b> Longitudinal magnetisation parallel to the external magnetic field $B_0$ . <b>(b)</b> Boltzmann distribution of populations for the spin-1/2 ensemble (positive $\gamma$ ), with the lower energy Zeeman sublevel being more populated.....	25
<b>Figure 3.3</b> Polarisation distribution immediately after an RF pulse. <b>(a)</b> Transverse magnetisation perpendicular to the external magnetic field $B_0$ . <b>(b)</b> Two Zeeman sublevels for spin-1/2 ensemble with equal spin populations and net transfer between them after the RF pulse excitation. ....	26
<b>Figure 3.4</b> The induction of an NMR signal. ....	27
<b>Figure 3.5</b> $B_1$ field induces rotation of magnetisation vector $M$ towards transverse plane in <b>(a)</b> the laboratory frame and <b>(b)</b> the rotating frame. Strength and duration of $B_1$ is set for a $90^\circ$ -rotation, leaving $M$ entirely in the transverse plane. ....	29
<b>Figure 3.6</b> Energy levels of a spin-3/2 nucleus in a homogeneous static magnetic field $B_0$ , in the case of a positive gyromagnetic ratio.....	37
<b>Figure 3.7</b> Multiple quantum coherences for a spin-3/2 ensemble. The red arrow indicates that there is a coherence between the two states. For $p\text{prsqrs}$ , the arrow points from state $s$ to state $r$ . ....	38
<b>Figure 3.8</b> Electric quadrupolar interaction. <b>(a)</b> A spherical spin-1/2 nucleus has a uniform electric charge distribution; thus, its electric quadrupolar interactions vanish. <b>(b)</b> A spin $> 1/2$ nucleus has a non-uniform electric charge distribution and thus, it interacts with the surrounding electric field gradient. ....	41
<b>Figure 3.9</b> Energy levels of a spin-3/2 nucleus, in the case of a positive gyromagnetic ratio. $\omega_0$ is the Larmor frequency of the nucleus. $\omega_Q(1)$ is the first-order quadrupolar coupling. ....	42
<b>Figure 3.10</b> The spectrum of a spin-3/2 ensemble and the corresponding $(-1)$ -quantum coherences. 44	
<b>Figure 3.11</b> Four types of sodium NMR characteristics in different molecular environments. <b>Top row:</b> energy level diagrams. <b>Middle row:</b> schematic SQ spectra corresponding to the mean quadrupolar frequency, $\omega_Q$ ; the $x$ -axis represents frequency, $\omega$ ; the $y$ -axis represents signal intensity. <b>Bottom row:</b> scheme of the time dependence of quadrupolar frequency, $\omega_Q$ , for the four spectral types. The <i>Type d</i> spectrum is a narrow Lorentzian line; the <i>type c</i> spectrum is a superposition of a narrow and a broad Lorentzian line; the <i>type b</i> spectrum consists of a central narrow Lorentzian line with two broad satellite Lorentzian lines; and the <i>type a</i> spectrum comprises three separated narrow Lorentzian lines. <b>Source:</b> Figure reproduced from (Rooney & Springer 1991) with permission from John Wiley and Sons (License No. 5745351153482). ....	49
<b>Figure 3.12</b> Interaction of a sodium cation with its surrounding environment. <b>(a)</b> Homogeneous environment. <b>(b)</b> Inhomogeneous environment. The sodium cation interacts with a negatively charged macromolecule (green area) through the electric field gradient (EFG). ....	50
<b>Figure 4.1</b> Structure of a superconductive magnetic resonance scanner. <b>(a)</b> A representative cross-section of a superconducting scanner. Two types of patient coils: a transmit/receive knee coil and a receive-only spine coil array. <b>(b)</b> The scanner has a superconducting coil that generates a static $B_0$ field, an RF coil that produces a circularly polarised $B_1$ field in the transverse plane ( $xy$ -plane) and three gradient coils that yield a linear alteration of the $z$ -component of the magnetic field depending on the $x$ ,	

## LIST OF FIGURES

$y$ and $z$ positions, $BG$ . Red dot: isocentre. <b>(c)</b> The action of gradient fields. Note that $x$ , $y$ and $z$ -gradients only alter the magnetic field along the $z$ -direction.....	51
<b>Figure 4.2</b> Gradient field and resonance frequency. A small, linearly changing gradient field, $BG$ , is added to the $B_0$ field ( $B_0 = 1.5T$ ) along/against the $z$ -direction. Different positions along the gradient direction ( $x$ , $y$ or $z$ ) possess different resonance frequencies. The isocentre has a resonance frequency of $\omega_0 = -\gamma B_0$ .....	54
<b>Figure 4.3</b> $T_2^*$ and $T_2$ decay. The gradient echo results in a $T_2^*$ decay, whereas the spin echo yields a $T_2$ decay.....	57
<b>Figure 4.4</b> Diagram of a 2D gradient-echo sequence. This sequence performs phase encoding (PE) for $nPE$ times. The number of frequency encoding (FE) steps is $nFE$ . SS = slice selection. ....	65
<b>Figure 4.5</b> An MRI sequence scheme using $k$ -space. In addition to the sampling locations (red dots), the $k$ -space trajectories (coloured lines) are also given. This scheme reflects the cumulative sum of gradient moments and the coverage of the acquired $k$ -space. The colour code from black to magenta represents the phase encoding steps from 1 to 12.....	65
<b>Figure 4.6</b> DISCOBALL radial $k$ -space sampling. The DISCOBALL scheme employs 4452 projections for <b>(a)</b> a homogeneous distribution of points in a sphere and <b>(b)</b> the corresponding $k$ -space trajectories. Points and projections are colour-coded from black to red, indicating that DISCOBALL first acquires $k$ -space lines at the top and bottom of the sphere and then the $k$ -space projections in the middle.....	67
<b>Figure 4.7</b> Representative gradient waveforms for 3D radial sampling. Gradient ramp-up and initial traversal are identical for <b>(a)</b> 3D radial and <b>(b)</b> 3D density-adapted acquisitions up until $k_0$ at $t_0$ indicated by the black dashed line. This line marks the onset of density adaption, achieved by a reduction in gradient strength and a consequent slow-down in $k$ -space traversal speed. Gradient ramp-down is not shown here. ....	67
<b>Figure 4.8</b> 2D Fermat spiral trajectory. By projecting the base 2D Fermat spiral <b>(a)</b> onto a cone, an interleaf of 3D FLORET <b>(b)</b> is generated. The cone is concentric with a given axis shown as the thick black line (here defined as the $kz$ axis) and defined by a certain angle, $\alpha$ , between its surface and the plane (here $kxy$ plane) perpendicular to the given axis. ....	69
<b>Figure 4.9</b> FLORET $k$ -space trajectories. The <b>(a)</b> $kz$ hub, <b>(b)</b> $ky$ hub and <b>(c)</b> $kx$ hub are combined to form a FLORET sphere in $k$ -space. ....	70
<b>Figure 4.10</b> Gradient waveforms of a representative interleaf of the FLORET sphere in $k$ -space.....	70
<b>Figure 4.11</b> Undersampling of FLORET results in incoherent aliasing. A <b>(a)</b> fully sampled and <b>(b)</b> nine-fold undersampled trajectory sets are illustrated, along with 2D cross sections of their respective PSFs <b>(c, d)</b> . <b>Source:</b> Figure reproduced from (Pipe et al. 2011) with permission from John Wiley and Sons (License No. 5745411307698).....	71
<b>Figure 4.12</b> Diagram of a spiral UTE sequence. Gradient and data acquisition are synchronised and commence after the dead time, $t_d$ . ADC readout length is denoted as $TRO$ . The echo time, $TE$ , results from $t_d$ and the RF pulse length, $t_{RF}$ .....	72
<b>Figure 4.13</b> Basic idea of gridding. The data samples (black dots) lie on some trajectory through $k$ -space (dashed line). Each data point is conceptually convolved with a gridding kernel (green cone). The convolution is evaluated at the adjacent grid points (red arrows).....	76
<b>Figure 4.14</b> Overview of the gridding process.....	76
<b>Figure 4.15</b> Schematics of fundamentals of a sparse representation. <b>(a)</b> Transform sparsity produces a set of sparse transform coefficients, $\theta$ , with $k$ non-zero elements after a sparsifying transform, $\Psi$ , operating on a signal, $x$ . <b>(b)</b> An $m \times 1$ $k$ -sparse signal can be converted to an $n \times 1$ set of measurements, $y$ , through an $n \times m$ sampling matrix, $A$ , ( $k \ll n < m$ ). The colours indicate the values of the elements in the matrices. The elements of $\theta$ in white are zeros. <b>Source:</b> (Chen et al. 2021) with permission from John Wiley and Sons (License No. 5745420106236).....	82

## LIST OF FIGURES

<b>Figure 4.16</b> k-space trajectories with two-fold incoherent undersampling. Grey phase-encoded lines or projections are skipped, while red ones are measured. <b>(a)</b> 2D Cartesian trajectories with pseudo-randomly undersampled phase-encoded lines and fully-sampled readouts. <b>(b-f)</b> 3D non-Cartesian UTE k-space trajectories that are often used in sodium MRI: <b>(b)</b> 3D radial, <b>(c)</b> stacks of spirals, <b>(d)</b> 3D cones, <b>(e)</b> TPI and <b>(f)</b> FLORET. <b>Source:</b> (Chen et al. 2021) with permission from John Wiley and Sons (License No. 5745420106236).....	83
<b>Figure 5.1</b> Multiple-quantum filter of the enhanced SISTINA sequence. The filter consists of three $\pi$ -RF hard pulses with an application of a twelve-step phase cycling scheme. The diagram shows two possible coherence transfer pathways to yield signals from TQ coherences. Here, $\tau$ is the preparation time, and $\delta$ is the evolution time. Time points are indicated by numbers within blue circles. ....	90
<b>Figure 5.2</b> Diagrams of enhanced SISTINA sequences. <b>(a)</b> Conventional enhanced SISTINA sequence with DISCOBALL UTE and MGRE MQF readouts. <b>(b)</b> Optimised enhanced SISTINA sequence with FLORET UTE and FLORET MQF readouts. <b>Source:</b> (Chen et al. 2021). ....	93
<b>Figure 5.3</b> k-space trajectories of enhanced SISTINA. <b>(a)</b> DISCOBALL trajectories (4452 projections) for UTE readouts of conventional enhanced SISTINA in the first measurement. FLORET trajectories for <b>(b)</b> UTE readouts (4464 projections) and <b>(c)</b> MQF readouts (372 projections) of the optimised enhanced SISTINA in the third measurement. <b>Source:</b> (Chen et al. 2021). ....	94
<b>Figure 5.4</b> Agarose phantoms. The schematic presents sodium concentrations in mmol/L and agarose concentrations in percent (e.g. 2% indicates 2 grams of agarose powder per 100 ml of deionised water). The 2% and 3% agarose phantoms simulate the less-restricted environment, whereas the 6% and 10% agarose phantoms mimic the restricted environment. <b>Source:</b> (Chen et al. 2021). ....	96
<b>Figure 5.5</b> The first-echo UTE, SQ and TQ images after B0 and B1 correction obtained from three measurements described in Table 5.2. <b>Source:</b> (Chen et al. 2021).....	98
<b>Figure 6.1</b> FLORET k-space trajectories. <b>(a)</b> and <b>(h)</b> present the first (in red), middle (in green) and last (in blue) projections of UTE and MQF FLORET, respectively. Fully sampled <b>(b)</b> UTE and <b>(i)</b> MQF FLORET k-space trajectories were pseudo-randomly and retrospectively undersampled by factors of {1.5, 2, 3, 4, 5}: undersampled <b>(c-g)</b> UTE and <b>(j-n)</b> MQF k-spaces. TA = total acquisition time. <b>Source:</b> (Chen et al. 2024).....	103
<b>Figure 6.2</b> Schematic and first-echo enhanced SISTINA images of a phantom. <b>(a)</b> The schematic displays sodium chloride concentration in mmol/L and agarose weight/deionised water volume in percentage. <b>(b)</b> Visual comparison between NUFFT and CS across all USFs on the first-echo UTE, SQ and TQ images of the phantom. <b>Source:</b> (Chen et al. 2024).....	107
<b>Figure 6.3</b> Image quality measures for NUFFT and CS reconstructions of phantom (Figure 6.2a) data across all USFs and echoes. The fully sampled NUFFT reconstructions were used as references ( <b>green</b> ). NUFFT ( <b>blue</b> ) and CS ( <b>red</b> ) reconstructions with various USFs are represented by different colour gradients. SSIM values were computed over the entire phantom for <b>(a)</b> UTE and <b>(c)</b> SQ images, and over the phantom compartments 3 – 6 for <b>(e)</b> TQ images. SNR was computed over the phantom compartment 6 for <b>(b)</b> UTE, <b>(d)</b> SQ and <b>(f)</b> TQ images. The legend in <b>(d)</b> applies to all other subplots. <b>Source:</b> (Chen et al. 2024). ....	108
<b>Figure 6.4</b> Visual comparison between NUFFT and CS on the first-echo in vivo images across all USFs. The UTE, SQ and TQ data were obtained from the brain of a 32-year-old healthy female. <b>Source:</b> (Chen et al. 2024). ....	109
<b>Figure 6.5</b> Image quality measures for both NUFFT and CS of in vivo data across all subjects, echoes and USFs. SSIM and SNR values were calculated from reference ( <b>green</b> ), undersampled NUFFT ( <b>blue</b> ) and undersampled CS ( <b>red</b> ) reconstructions. The means and standard deviations of SSIM and SNR values over ten healthy subjects are indicated by dots and whiskers, respectively. SSIM <b>(a, c, e)</b> and SNR <b>(b, d, f)</b> were calculated over the whole brain region and the WM region, respectively. An asterisk (*) is marked if the CS-based SSIM or SNR value is significantly ( $p \leq 0.05$ ) higher than that from NUFFT. The legend in <b>(d)</b> applies to all other subplots. <b>Source:</b> (Chen et al. 2024).....	110



LIST OF TABLES

<b>Table 3.1</b> A selection of nuclei and their properties (Levitt 2008).....	19
<b>Table 3.2</b> Irreducible tensor operators for spin-3/2.....	45
<b>Table 5.1</b> Seven SQ coherence pathways.....	92
<b>Table 5.2</b> Enhanced SISTINA sequence parameters for three measurements (repetition time = 213.5 ms, total acquisition time = ~16 min). FWHM: full width at half maximum of the point spread function, calculated using the MIRT toolbox. <b>Source:</b> (Chen et al. 2021). ....	95
<b>Table 6.1</b> Sequence parameters of the optimised enhanced SISTINA. TE = echo time; FOV = field-of-view; FWHM = full width at half maximum; UTE = ultra-short echo time; MQF = multiple-quantum-filtered; Voxel size = nominal resolution of the reconstructed image. ....	101
<b>Table 6.2</b> Summary statistics for quantitative analysis of ten healthy subjects. Quantitative parameters ( $T2f^*$ , $T2s^*$ and TSC) obtained from fully sampled NUFFT-based reconstructions, are provided as reference values. Values in the form of (mean $\pm$ std) represent the means and standard deviations of quantitative parameters over ten healthy subjects. Differences between quantitative estimates and reference values are provided in parentheses. Differences within the range from -15% to 15% are marked in bold. <b>Source:</b> (Chen et al. 2024).....	111





## LIST OF ABBREVIATIONS

Adenosine TriPhosphate (ATP)	Total sodium concentration (TSC)
Alzheimer's disease (AD)	Total Variation (TV)
Analog-to-Digital Converter (ADC)	Triple-Quantum (TQ)
CerebroSpinal Fluid (CSF)	Twisted Projection Imaging (TPI)
Compressed Sensing (CS)	Two-Dimensional (2D)
DIrection SCHEME Obtained By ALigning points on Latitudes (DISCOBALL)	Ultra-short Echo Time (UTE)
Discrete Cosine Transform (DCT)	UnderSampling Factor (USF)
Double Quantum Coherence (DQC)	White Matter (WM)
Echo Time (TE)	
Fast Fourier Transform (FFT)	
Fermat Looped, ORthogonally Encoded Trajectories (FLORET)	
Field-Of-View (FOV)	
Full Width at Half Maximum (FWHM)	
Huntington's disease (HD)	
Magnetic Resonance Imaging (MRI)	
Michigan Image Reconstruction Toolbox (MIRT)	
Multiple sclerosis (MS)	
Multiple-Quantum-Filtered (MQF)	
Non-Uniform Fast Fourier Transform (NUFFT)	
Nuclear Magnetic Resonance (NMR)	
One-Dimensional (1D)	
Osteoarthritis (OA)	
Point Spread Function (PSF)	
RadioFrequency (RF)	
Repetition Time (TR)	
Signal-to-Noise Ratio (SNR)	
SImultaneous Single-quantum and TriPle- quantum-filtered imaging of $^{23}\text{Na}$ (SISTINA)	
Single-Quantum (SQ)	
Structural SIMilarity (SSIM)	
Three-Dimensional (3D)	



### 1 Introduction and Outline

Nuclear Magnetic Resonance (NMR) is a physical phenomenon in which nuclei within a strong static magnetic field are disturbed by a weak oscillating magnetic field and respond by generating an electromagnetic signal with a specific frequency relative to the precession of the nuclear spin. It was first observed in the late 1930s by Isidor Isaac Rabi (Rabi 1937; Rabi et al. 1938) who won the Nobel Prize in Physics in 1944 for this work. NMR was independently demonstrated by Felix Bloch (Bloch et al. 1946) and Edward Mills Purcell (Purcell et al. 1946) in 1946, which was rewarded with the Nobel Prize for Physics in 1952 for the two scientists. In 1973, Paul Lauterbur (Lauterbur 1973) and Peter Mansfield (Mansfield & Grannel 1973) discovered that images can be created from the NMR signal by applying spatial encoding. Nowadays, this innovation is called Magnetic Resonance Imaging (MRI). Its revolutionary medical contributions earned Lauterbur and Mansfield the Nobel Prize for Medicine in 2003. Another MRI pioneer was Raymond Damadian, who discovered that NMR can be used for medical diagnosis in 1971 (Damadian 1971) and built the first whole-body MRI scanner in 1977 (Damadian et al. 1977). In addition, Richard Robert Ernst was awarded the Nobel Prize in Chemistry in 1991 for his contributions to the development of the methodology of Fourier transform NMR spectroscopy in 1976 (Aue et al. 1976). These historical works are the cornerstones of technological and methodological developments with numerous contributions to medical diagnosis, clinical treatment and biomedical research up until today.

MRI is widely used in hospitals and clinics because it does not require ionising radiation and thus is relatively harmless to the patient, distinguishing it from computer tomography and positron emission tomography. In addition, MRI provides better soft tissue contrast than computer tomography, allowing for a better distinction between fat, water, muscle and other soft tissues. However, it may be considered less comfortable by subjects due to the usually louder and longer measurements with the patient in a long and confining tube. MRI experiments can be performed on any nucleus with a non-zero spin quantum number. Hydrogen-1 ( $^1\text{H}$ ) nuclei have the highest natural abundance and NMR sensitivity among all nuclei in biological tissues and are, therefore, the target nucleus in routine clinical practice. The high concentration of hydrogen nuclei within soft tissues and fluids facilitates imaging with a high spatial resolution. MRI techniques can yield information on tissue contrasts and functional parameters by exploiting the complex interaction of nuclei with their environment. Common tissue contrasts include the total number of nuclei (i.e. spin density), NMR-signal-related

properties (e.g. longitudinal and transverse relaxation times) and magnetic susceptibility of various compounds (e.g. blood, iron and diamagnetic calcium). Functional parameters are associated with changes in blood flow, such as blood-oxygen-level-dependent response, arterial spin labelling, diffusion and perfusion.

Despite the great success of hydrogen MRI in clinical routine and scientific research, the standard MRI is relatively limited in providing direct biochemical markers for tissue viability and cell integrity or for tracking temporal changes in tissue viability during medical treatment. On the other hand, MRI based on other nuclei (termed X-nuclei) focuses on revealing the underlying changes in physiological processes, thus providing complementary information to hydrogen MRI. Magnetic resonance observable nuclei that have physiological roles in the human body include Sodium-23 ( $^{23}\text{Na}$ ) with a link to cell vitality, Potassium-39 ( $^{39}\text{K}$ ) and Chlorine-35 ( $^{35}\text{Cl}$ ) relative to the functioning of muscle and neuronal cells and Oxygen-17 ( $^{17}\text{O}$ ) associated with energy metabolism.

The potential of X-nuclei MRI was investigated early. In 1985, only about a decade after the first hydrogen images were produced, sodium was chosen for the first in vivo X-nuclei experiments on the human body (Hilal et al. 1985). This was because sodium yields the second strongest NMR signal among all nuclei within biological tissues, surpassed only by the hydrogen nucleus. Sodium MRI was subsequently applied to investigate brain tumours and ischemia in the late 1980s (Grodd & Klose 1988). Three decades after the first in vivo sodium images (Hilal et al. 1985), the first potassium and chlorine MRI images were published (Nagel et al. 2014; Umatham et al. 2013). Compared with potassium and chlorine MRI, the first in vivo oxygen MRI image was shown earlier (Fiat et al. 2004). Despite these early starts, X-nuclei MRI, particularly sodium MRI, did not witness the same rapid development as hydrogen MRI, primarily due to the interrelated issues of relatively poor quality of sodium images and long measurement times. These issues were mainly caused by technical limitations, relatively low in vivo concentration, low NMR sensitivity and complex NMR properties of sodium nuclei. In the 1990s, interest in sodium MRI grew due to the increased access to stronger magnetic fields (3T or higher) and improved acquisition strategies and hardware. Novel contrasts such as multiple-quantum filtering offered further promise for tissue discrimination and characterisation (Hancu et al. 1999; Wimperis & Wood 1991). This trend has continued and intensified throughout the 2000s until today.

Today, sodium MRI has made remarkable progress with an increasing number of pathological examinations and clinical studies. Nevertheless, sodium MRI still suffers from comparably low

image quality and long acquisition times. Currently, sodium MRI research is conducted in two directions (Madelin et al. 2014): (1) methodological advancements associated with data acquisition and image reconstruction and (2) the application of new techniques over various pathologies. This thesis follows the first direction, i.e. methodological development for sodium MRI, and mainly focuses on data acquisition and image reconstruction. The main interests are an improvement of image quality and image sparsity by implementing an advanced data acquisition scheme (Chapter 5) and reducing data acquisition time by applying an iterative non-linear reconstruction method (Chapter 6).

### Thesis Outline

This thesis is structured in two parts. **Part I**, consisting of three chapters, provides the motivation and theoretical background of sodium MRI. It outlines the physiological basis of sodium ions in biological tissues, relevant NMR physics and the resulting imaging requirements for sodium nuclei.

**Chapter 2 Physiological Significance of Sodium** introduces the biological background of sodium ions in the human body. It provides an overview of the biomedical implications of sodium homeostasis in healthy physiology. In particular, this chapter covers its importance in cell metabolism and integrity regulated by the sodium-potassium pump and its role as a counter ion to large macromolecules in the extracellular space. Furthermore, the association between the disruption of sodium homeostasis and various pathologies is briefly discussed.

**Chapter 3 Nuclear Magnetic Resonance** reviews the fundamental NMR physics based on both classical and quantum mechanical descriptions. This framework is necessary to understand the specific NMR signal characteristics of sodium nuclei. This chapter commences with an introduction to nuclear spin and magnetism, followed by a description of spin-1/2 dynamics. Furthermore, the spin-3/2 dynamics are introduced, with particular attention given to the description of relaxation mechanisms based on Hamiltonians and density matrices. Finally, the characteristics of the NMR spectra of sodium ions in biological tissues are briefly introduced.

**Chapter 4 Magnetic Resonance Imaging** is the last background chapter and closes the circle from physiology to NMR fundamentals and finally imaging. It describes data acquisition and image reconstruction for MRI, particularly sodium MRI. It commences with a brief introduction to the hardware structure of a typical MRI scanner. Then, it outlines the principles of NMR-based imaging, focusing on MRI aspects that are of particular relevance to the

remainder of this work. This chapter proceeds with an overview of sodium MRI-specific imaging approaches. Regarding data acquisition, this chapter describes typical non-Cartesian sampling schemes and sequence timing approaches associated with sodium signal acquisition. Regarding image reconstruction, two common approaches are examined: (1) standard image reconstruction based on gridding and (2) iterative reconstruction based on Compressed Sensing (CS) techniques. The latter approach is of particular interest due to its great potential to accelerate image acquisition.

**Part II** presents the critical novel contributions of this work. Within the scope of this thesis, advances in sodium MRI focusing on multiple-quantum filtering were explored from two different perspectives, each presented in a separate chapter in this part. They are followed by the final concluding chapter.

**Chapter 5 Data Acquisition** investigates the data acquisition aspect of Multiple-Quantum-Filtered (MQF) sodium MRI. In this work, MQF sodium MRI was based on the enhanced Simultaneous Single-quantum and Triple-quantum-filtered imaging of  $^{23}\text{Na}$  (SISTINA), a sodium MRI technique allowing images to be weighted towards restricted (mainly intracellular) sodium. This chapter aimed to optimise the enhanced SISTINA sequence using a high-efficiency non-Cartesian sampling scheme. The optimised sequence was compared with a conventional enhanced SISTINA sequence in phantom measurements. The optimisation greatly improved the Ultra-short Echo Time (UTE) image quality from visual inspection, while maintaining the visual performance of MQF images and satisfying the prerequisite for CS application (Chapter 6) by introducing incoherence to the raw data.

**Chapter 6 Image Reconstruction** explores the reconstruction aspects of MQF sodium MRI. MQF sodium MRI often suffers from low image quality and associated clinically infeasible acquisition times. This study aimed to alleviate the above limitation by applying CS to accelerate enhanced SISTINA acquisitions at 7T without a noticeable loss of information. Compared with standard Non-Uniform Fast Fourier Transform (NUFFT), CS accelerated enhanced SISTINA by up to twofold at 7T in this study with reduced noise levels, while maintaining primary structural information, reasonable weightings towards total and compartmental sodium and relatively accurate in vivo quantification.

**Chapter 7 Conclusion** presents the last chapter of this thesis and summarises the main contributions of this work. In addition, an outlook for future study is given.

# **THEORY AND BACKGROUND**

## **MOTIVATION AND PRINCIPLES OF SODIUM MRI**





## 2 Physiological Significance of Sodium

### *From Physiology to Nuclei*

Sodium is an essential component of the human body. A better understanding of the significance of sodium in physiological processes and functions could shed light on its relation to some pathological conditions. The physiological significance of sodium homeostasis is the cornerstone of scientific research into the potential implications for early diagnosis and medical management. This chapter provides an overview of the physiological significance of sodium homeostasis in human biology and briefly outlines the association between the disruption of sodium homeostasis and various pathologies.

### 2.1 Sodium in Health

Sodium has two primary biological functions in the human body: an active role in the energy-consuming process of membrane transport and a passive role as the primary counter ion that balances charges of anionic macromolecules in tissues.

#### 2.1.1 Membrane Transport – Active Role

In tissues, semi-permeable membranes separate compartments within and between individual cells, and large ionic concentration gradients exist between intracellular and extracellular spaces. Multiple transport mechanisms provide pathways for the influx and efflux of sodium, among which the sodium-potassium pump ( $\text{Na}^+/\text{K}^+\text{-ATPase}$ ) (Rose & Valdes 1994), a membrane-bound protein, plays a primary role in establishing the sodium electrochemical gradient. As shown in Figure 2.1, the sodium-potassium pump maintains the transmembrane sodium and potassium gradients by extruding three sodium ions from the cell while transporting two potassium ions into the cell at the expense of energy given by the hydrolysis of Adenosine TriPhosphate (ATP). In healthy tissues, the intracellular sodium concentration (typically 10 – 15 mmol/L) is about ten times lower than the extracellular sodium concentration (typically 140 – 150 mmol/L); conversely, the intracellular and extracellular potassium concentrations are 140 mmol/L and 5 mmol/L, respectively (Madelin et al. 2014).

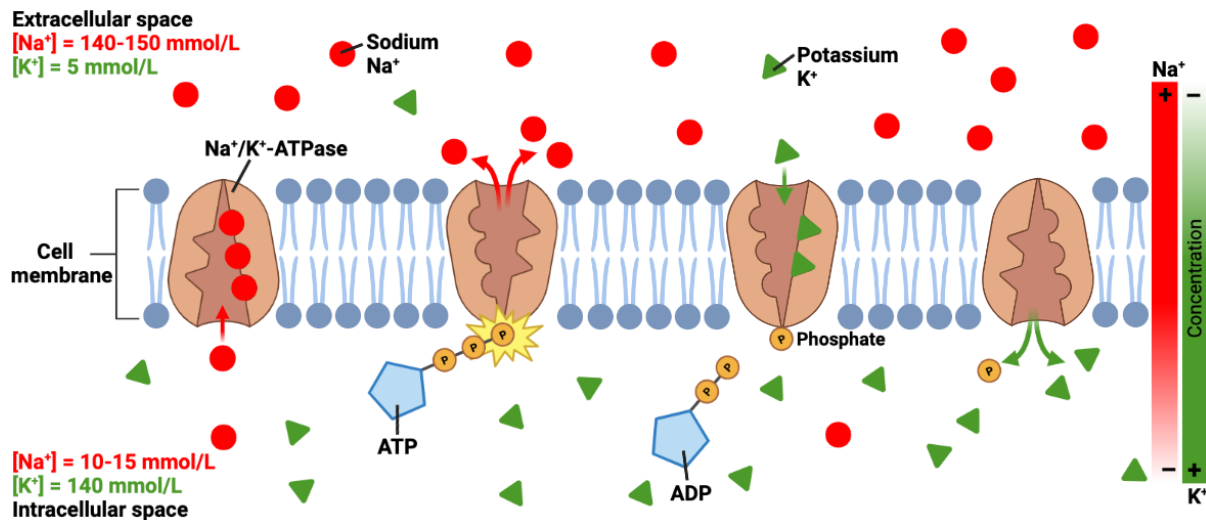


**Figure 2.1** Schematic representation of the sodium-potassium pump activity. The sodium-potassium pump maintains large sodium and potassium gradients across the cell membrane by moving three sodium ions out of the cell and simultaneously transferring two potassium ions into the cell. This process is powered by the hydrolysis of the third high-energy phosphate bond of adenosine triphosphate.

The sodium-potassium pump is of fundamental importance in various physiological processes and thus earned its discoverer, Jens Christian Skou, a Nobel Prize in Chemistry in 1997. In the following, its principal functions are briefly discussed.

### *Controlling Cell Volume*

The osmolarity of a cell is defined as the sum of the concentrations of various ion species, proteins and other organic compounds inside the cell. If the osmolarity of a cell is higher than the osmolarity outside the cell, water flows into the cell through osmosis, causing it to swell and thus increasing its volume. By regulating the balance of sodium and potassium ions across the cell membrane, the sodium-potassium pump helps maintain the normal cell volume in the biological tissues. Failure of this regulation can result in cell swelling and eventual rupture.

### *Molecule Transport*

The concentration gradients established by the sodium-potassium pump provide the driving force for the several secondary active transport proteins, which carry ions (e.g. calcium and proton), metabolites and nutrients (e.g. glucose and amino acids), neurotransmitters (e.g. glutamate) and other molecules across the membrane. For example, in the gut, sodium is transported out of the re-absorbing cell on the blood (interstitial fluid) side through the sodium-potassium pump; however, on the re-absorbing (luminal) side, the sodium-glucose symporter imports both sodium ions and glucose by consuming energy provided by the created sodium

gradient. The sodium-potassium pump is an essential component of membrane transport and plays a vital role in maintaining cell metabolism and function.

### ***Signal Transmission***

The sodium-potassium pump expels three sodium ions and introduces two potassium ions, resulting in a net export of a single positive charge per pump cycle. This establishes a relatively static membrane potential of quiescent cells, called the resting membrane potential ( $-60$  to  $-70$  mV in neurons). This electrical potential is the basis for the action potential in excitable cells, including neurons, muscle cells and some plant cells. Via action potentials, neurons propagate signals along the neuron's axon for communication across cells; other types of cells utilise the signals to activate intracellular processes, such as muscle contraction. Signal transmission is based on the disturbance of the resting membrane potential beyond a threshold voltage that leads to the opening of voltage-gated ion channels and the rapid influx of sodium ions, causing a reversal of electric polarity across the plasma membrane. After the action potential, the ion channels close, and the resting potential is re-established by the sodium-potassium pump.

### **2.1.2 Counter Ions – Passive Role**

Since macromolecules (e.g. proteins and nucleic acids) that contribute to the structural integrity of tissues have electrostatically charged functional groups, counter ions are required to balance the resulting electrostatic interactions. Sodium as a counter ion plays a crucial role in maintaining the structural and functional integrity of these macromolecules in both intracellular and extracellular spaces in all tissues. For example, cartilage comprises an extracellular matrix with cross-linked glycosaminoglycan polymers. Sodium acts as the counter ion to control the bound water and electrostatic repulsion of the glycosaminoglycan network, thereby determining the compressive elasticity for buffer weight bearing in joints. The brain's extracellular matrix differs from that of cartilage – it consists primarily of macromolecules of proteoglycans with variable glycosaminoglycan polymers such as chondroitin sulphate. Nevertheless, the structural principle of the macromolecules and sodium counter ions still applies. The electrostatic effect of the extracellular matrix provides a structural scaffold for controlling tissue integrity while balancing the water distribution between the intracellular and extracellular compartments and buffering cationic concentrations in small interstitial spaces.

### 2.2 Sodium in Disease

Sodium ion homeostasis in the human body is of great significance in ensuring the proper functioning of a cell. Disruption of cell membrane integrity or impairment of energy metabolism can increase the intracellular sodium concentration; in contrast, the extracellular sodium concentration remains largely unchanged due to tissue perfusion. Thus, the elevated intracellular sodium concentration resulting from abnormal sodium ion homeostasis is often considered a sensitive early indicator of various pathological conditions. Multiple reviews have discussed the link between sodium homeostasis breakdown and specific pathologies in various anatomical regions (Bangerter et al. 2016; Francis et al. 2017; Madelin et al. 2014; Shah et al. 2016; Thulborn 2018; Zaric et al. 2021). Since sodium within the brain is of particular interest in this thesis, a couple of neurological applications of sodium imaging will be emphasised in the following overview. In addition, the promising applications of sodium ion detection on other anatomical regions across the human body will be briefly discussed.

#### 2.2.1 Brain Diseases

Many sodium MRI studies have been performed on the human brain to evaluate its possible use in the assessment of various neurological diseases. Sodium MRI can probe the changes in cellular integrity and viability in the brain tissues through the alternations in intracellular sodium concentration and/or extracellular volume.

##### *Stroke*

A stroke is characterised by the impaired blood supply to the brain with rapid onset of neurological symptoms. Strokes can be classified into two major categories: ischemic (i.e. blockage of blood supply to the brain) and hemorrhagic (i.e. blood vessel rupture). Both cases can cause lasting brain damage, long-term disability or even death. Ischemic strokes are more common, constituting about 87% of strokes. The decrease in blood supply can lead to a loss of cellular energy production, which impairs the sodium-potassium pump and thus induces a breakdown of sodium ion balance across the cell membrane. An increase in intracellular sodium due to the loss of cell integrity and an increase in extracellular volume due to cell death could increase Total Sodium Concentration (TSC). Therefore, quantitative sodium MRI can non-invasively provide accurate spatial information on tissue viability and temporal information on stroke onset, which has potential clinical implications for stroke management (Boada et al. 2012; Jones et al. 2006; Thulborn et al. 1999). Advanced sodium MRI techniques based on, for example, multiple-quantum filtering (Hancu et al. 1999) or inversion recovery

preparation (Madelin et al. 2010; Stobbe & Beaulieu 2005), enable images to be weighted towards intracellular sodium content. These techniques may have more clinical significance and are thus worthy of further investigation.

### ***Tumours***

Tumours are characterised by abnormal cell division and proliferation, which can be initiated by changes in  $\text{Na}^+/\text{H}^+$  exchange kinetics and therefore changes in intracellular and extracellular acid-base balance. This mechanism causes reduced sodium-potassium pump activity, leading to an increased intracellular sodium concentration. Similarly, both tumour neovascularisation and increased interstitial space result in an increased extracellular volume fraction. Due to the increased intracellular sodium and extracellular volume, TSC levels in malignant tumours are likely to be elevated and could be non-invasively measured by single-pulse quantitative sodium MRI. Implementation of multiple-quantum filter (Fiege et al. 2013) or inversion recovery (Nagel, Bock, et al. 2011) preparations in sodium acquisitions could provide more specific information on changes in the intracellular content by reducing the weight of fluids and/or extracellular sodium in image contrast.

### ***Multiple Sclerosis***

Multiple Sclerosis (MS) is an inflammatory neurological disease characterised by focal and diffuse inflammation in White Matter (WM) and Grey Matter (GM), demyelination of the axons and neuroaxonal injury and loss (Bjartmar & Trapp 2001). The cellular and molecular mechanisms causing neurodegeneration and neuroinflammation in MS are closely related to sodium. It has been shown that the decreased ATP supply in MS may lead to the breakdown of the sodium-potassium pump and thus toxic sodium accumulation in the intracellular space (Huhn et al. 2019). Consequently, the increased intracellular sodium concentration may provoke a reverse action of the  $\text{Na}^+/\text{Ca}^{2+}$  exchanger followed by calcium accumulation, leading to the activation of neurodegenerative signalling cascades. A preliminary sodium MRI study showed that TSC in acute and chronic lesions was elevated compared to normal-appearing tissues in MS patients (Inglese et al. 2010). Going forward, the compartmental discrimination between intracellular and extracellular sodium using triple-quantum-filtering or inversion recovery techniques may provide additional valuable information for understanding the pathophysiological mechanisms involved in tissue damage in MS (Shymanskaya et al. 2019).

### ***Alzheimer's Disease***

Alzheimer's Disease (AD) is a neurodegenerative disease with a pattern of progressive cognitive and functional impairment. It is the cause of 60 – 70% of dementia cases. There is a significant interest in finding biomarkers for detecting early signs of AD and tracking its progression. Sodium MRI was suggested to have the potential to be a clinically useful tool to detect the neuropathologic changes associated with AD with the hypothesis that the alterations of the sodium levels in the brains of AD patients are related to AD cell death. A slight increase in sodium signal intensity (7.5%) was found in the brains of AD patients compared to healthy controls (Mellon et al. 2009). However, the physiological basis of this increase in sodium content remains unclear. Possible explanations are that the extracellular volume increases due to cell death and fluid invasion and/or the intracellular sodium concentration increases due to amyloid beta channels in the cell membrane or the impairment of the sodium-potassium pump. Advanced sodium MRI techniques allowing fluid suppression and/or intracellular sodium isolation (e.g. inversion recovery or multiple-quantum filter) may provide complementary information on studying the pathophysiological mechanisms underlying AD progression.

### ***Huntington's Disease***

Huntington's Disease (HD) is an autosomal dominant, progressive neurodegenerative disorder clinically characterised by progressive motor dysfunction (e.g. hyperkinesia), cognitive decline and psychiatric impairment. A pilot study found that TSCs of the whole brain in HD patients were elevated compared with healthy controls (Reetz et al. 2012). However, similar to AD, these elevated TSCs have not been satisfactorily explained due to limited data, poor image resolution and lack of differentiation between intracellular and extracellular sodium content. The use of sodium MRI with multiple-quantum filtering (Hancu et al. 1999; Kjemp-Harper et al. 1995) may help explain these observed TSC variations, which are often associated with changes in cellular and metabolic integrity that may contribute to structural degeneration in HD.

### **2.2.2 Other Organ Diseases**

In addition to the brain, sodium provides a valuable marker for diseases in other anatomical regions across the human body. Some of them are briefly outlined below.

#### ***Heart (Myocardial Infarction)***

In myocardial infarction, the sodium-potassium pump function is inhibited due to energy depletion, and the extracellular volume is enlarged due to myocardial oedema formation or

scarring. These pathophysiological conditions can lead to an increase in intracellular sodium concentration. Quantitative sodium MRI is considered a good candidate for the detection of cardiac infarction by measuring localised increased sodium content in cardiac tissues, thereby helping distinguish viable tissues from non-viable tissues (Bottomley 2016). Advanced sodium MRI techniques that enable images to be weighted towards intracellular sodium (e.g. multiple-quantum filter) might better represent infarcted tissues and adjacent areas.

### ***Skeletal Muscle***

The resting membrane potential maintained by the sodium-potassium pump is critical for proper skeletal muscle functioning. Muscle contraction is based on the action potential – the disturbance of resting membrane potential by rapid sodium influx and potassium efflux through sodium- and potassium-gated channels. Many pathological conditions, such as diabetes, starvation and hypothyroidism, can be linked to a reduction in sodium-potassium pump activity in skeletal muscle (Clausen 2003). For example, the number of sodium-potassium pumps is reduced, and the pumping activity is weakened in diabetic patients, resulting in a decrease in the ability to extrude sodium from cells and thus an increase in intracellular sodium content in muscle tissues. Sodium MRI has the potential to provide insights into muscle physiology and disorders by measuring the changes in sodium intensities and relaxation times in muscles after voluntary muscle contractions. Furthermore, Suppression of fluid and/or extracellular sodium signal suppression by multiple-quantum filtering or inversion recovery may provide complementary information for investigating the pathophysiological basis of skeletal muscle.

### ***Cartilage (Osteoarthritis)***

OsteoArthritis (OA) is a degenerative disease of the articular cartilage, characterised by a reduction of fixed charge density concentration, possible changes in the size and organisation of the collagen fibres and aggregation of the proteoglycans. Since there are no known curative or preventive treatments for OA, early detection of OA before irreversible morphological changes and an accurate method to quantify the effects of potential treatments are of fundamental importance. Sodium concentration has been shown to strongly correlate with fixed charge density and glycosaminoglycan content in cartilage, so quantitative sodium MRI can also be used to directly detect glycosaminoglycan loss in early OA (Wheaton et al. 2004). Due to the presence of synovial fluid or joint effusion, applying multiple-quantum filtering or inversion recovery to suppress signals from surrounding fluids can help measure small changes in TSCs within the cartilage.

### ***Kidney***

The kidneys play a critical role in regulating homeostatic functions such as extracellular fluid volume, acid-base balance, electrolyte concentrations and blood pressure (by maintaining salt and water balance) (Zöllner et al. 2016). This role is tightly dependent on the regulation of extracellular sodium in the kidney, resulting in a concentration gradient from the cortex to the medulla. Therefore, by detecting changes in sodium gradient or differences in the relaxation times, quantitative sodium MRI may provide valuable information for assessing renal functions in various diseases such as nephropathy, renal failure and renal transplantation.

### **2.3 Motivation for Sodium Imaging**

In addition to the prevention of diseases, the focus of medical and related research is on the effective management of diseases, which is based on an early and accurate diagnosis and the monitoring of treatments. Many disease manifestations begin at the cellular level, with perturbations in cellular structure and metabolism. Ideally, detection techniques measure the onset of biochemical changes before clinical symptoms appear and facilitate the accurate assessment of physiological parameters during and after treatment.

The appeal of sodium-based imaging lies in its direct link to biochemical information, endowing biomarkers with the potential for diagnostic and monitoring applications. The concept of MRI establishes an approach for the non-invasive in vivo detection of sodium and is therefore of great clinical significance. Compared to the widely used hydrogen MRI, sodium MRI provides a specific marker for cell physiology that enables a distinct interpretation. Furthermore, the intracellular sodium concentration is sensitive to cellular metabolic dysfunctions, whereas the extracellular sodium concentration remains relatively constant due to tissue perfusion. In light of the above, the advancement of restricted (predominantly intracellular) sodium-weighted MRI techniques for applications to the human brain is the primary purpose of this thesis.



### 3 Nuclear Magnetic Resonance

#### *From Nuclei to Signal*

This chapter describes the fundamental physics of Nuclear Magnetic Resonance signal generation. Nuclear spin and magnetism are introduced using quantum mechanical and semi-classical approaches. Further, the origin of the NMR signal is explained in both classical and quantum mechanical treatments. Spin-3/2 Hamiltonians are introduced, and density matrix formalism is used to describe NMR signal generation and relaxation. Finally, the physical properties of sodium ions in biological tissues are discussed. This chapter mainly follows the book of (Levitt 2008).

#### 3.1 Spin and Angular Momentum

Spin is an intrinsic property of particles. It is also a form of angular momentum. A solid understanding of the concept of spin is crucial in this work, as spin provides a wonderful tool for peering into the microscopic and internal structures of objects without disturbing them. This section first introduces the angular momentum of rotating molecules. The specific concept of spin angular momentum is further described. Finally, the combination of multiple angular momenta is discussed.

##### 3.1.1 Rotational Angular Momentum

Fundamentally, matter is made of atoms that consist of a hull containing negatively charged electrons and a nucleus. The atomic nucleus comprises two types of nucleons: charge-free neutrons and positively charged protons. Essential physical properties originate from these elementary particles. The mass of the nucleus accounts for most of the atomic mass. Many other physical properties, such as heat capacity, are strongly dependent on the nuclear mass. The chemical properties of an atom are determined by the number and the configuration of electrons in the hull. The magnetic interactions of atomic nuclei with the molecular environment and an external apparatus can reveal detailed information on the atomic structure, molecular composition and macroscopic structure of an investigated sample. The probe into this information is the spin of the nucleons.

Spin is an intrinsic property of an elementary particle. Due to its quantum mechanical properties, the concept of spin may never be fully grasped without knowledge of quantum mechanics. Formally, spin is also a mathematical form of angular momentum. It has a classical

### 3.1 Spin and Angular Momentum

---

analogue: Any rotating object possesses an angular momentum – a quantity vector. The direction of the vector can be determined using the “right-hand rule”: If the right-hand fingers “wrap around” in the direction of the rotation, the thumb points in the direction of the angular momentum vector. In classical mechanics, the macroscopic angular momentum of a rotating object may take any value.

In quantum mechanics, the microscopic angular momentum of a molecule can only take specific values (i.e. quantised – hence the name “quantum mechanics”). For example, A rotating diatomic molecule possesses a set of rotational states, in which the total angular momentum,  $L_{\text{tot}}$ , has one of the values:

$$L_{\text{tot}} = [J(J+1)]^{1/2} \hbar, \quad (3.1)$$

where  $J$  takes integer values  $J = \{0, 1, 2, \dots\}$ , and  $\hbar$  is the Planck’s constant divided by  $2\pi$ . The value of  $J$  determines the rotational state of the molecule, which depends on the history and environment of the molecule.

The rotational energy of the molecule is proportional to the square of the total angular momentum, and thus the energy is also quantised. The rotational energies,  $E_J$ , of the stable rotational states are:

$$E_J = BJ(J+1), \quad (3.2)$$

where  $B$  is the rotational constant for the molecule, determined by the properties of the molecule.

The total angular momentum of the molecule determines the speed of its rotation but contains no information on the direction of the rotation. This information is given by specifying an additional quantum number,  $m$ , which is sometimes referred to as the azimuthal quantum number. This quantum number takes an integer value from the total  $(2J+1)$  values of  $\{-J, -J+1, \dots, +J\}$ . The quantum number  $m$  makes no contribution to the rotational energy in the absence of an external magnetic field, as can be seen in Eq. (3.2). Therefore, each of the  $(2J+1)$  states with the same value of  $J$  but different values of  $m$  have the same energy; these states are said to be degenerate. However, applying a magnetic field may cause each of the  $(2J+1)$  sublevels to have a slightly different energy. The breakdown of the degeneracy is called the Zeeman effect. The energy separation between the  $m$  sublevels in an external magnetic field is called the Zeeman splitting.

### 3.1.2 Spin Angular Momentum

As mentioned above, spin – as a quantity – can also be described mathematically using angular momentum. However, it is not produced by the actual rotation of the particle but is an intrinsic property of the particle itself. Analogously to Eq. (3.1), the total angular momentum of particles due to spin takes values of the form:

$$L_{\text{tot}} = [S(S + 1)]^{1/2} \hbar. \quad (3.3)$$

Each elementary particle has a specific value for the spin quantum number  $S$ . Here,  $S$  is used to replace  $J$  to distinct between the spin angular momentum and rotational angular momentum. Again, the direction of the spin may be specified with the spin azimuthal quantum number,  $m$ , taking one of the  $(2S + 1)$  possible values. The sublevels are degenerate without an external field but may have different energies with an applied electric or magnetic field. In contrast to  $J$ ,  $S$  can be given a half-integer or integer value. For example, the electron has a spin  $S$  of  $1/2$ , and the photon possesses a spin  $S$  of  $1$ . The spin of an elementary particle (e.g. an electron) is intrinsic and independent of its history and environment. Even at the absolute zero of the temperature scale, an elementary particle (such as an electron) simply has spin; in contrast, all rotational motion disappears and hence  $J = 0$  in Eq. (3.1). However, an electron may have both angular momenta – an “intrinsic” spin angular momentum and a “conventional” angular momentum due to motion such as orbital angular momentum resulting from its circulating motion around the nucleus. How multiple angular momenta are combined is discussed in the next section.

### 3.1.3 Combining Angular Momenta

The combination of multiple angular momenta leads to a total angular momentum. Consider a system with two parts with quantum numbers  $J_1$  and  $J_2$ . Each part is a source of angular momentum that may originate from spin or rotational motion. The total angular momentum of the entire system is given by:

$$L_{\text{tot}} = [J_{\text{tot}}(J_{\text{tot}} + 1)]^{1/2} \hbar, \quad (3.4)$$

where  $J_{\text{tot}}$  is the total angular momentum quantum number of the complete system. It takes one of the following possible values:

$$J_{\text{tot}} = \{|J_1 - J_2|, |J_1 - J_2| + 1, \dots, |J_1 + J_2|\}. \quad (3.5)$$

Two particles of spin  $1/2$ , i.e.  $S_1 = S_2 = 1/2$ , is often used to explain this combination rule in detail. In this case, there are only two possible states for the total angular momentum quantum number, namely  $S_{\text{tot}} = |S_1 - S_2| = 0$  and  $S_{\text{tot}} = |S_1 + S_2| = 1$ . In the former state, the two spins cancel each out, being said as “the spins are anti-parallel”. The latter state is often expressed as the two spins being “parallel”. The anti-parallel configuration has only one state with azimuthal quantum number  $m = 0$  and thus is not degenerate. This state is called a singlet state. The parallel configuration, on the other hand, leads to three substates with azimuthal quantum numbers  $m = \{-1, 0, 1\}$ . These states are often called triplet states to emphasise their threefold degeneracy, which may be broken by applying an external field.

### 3.2 Nuclear Spin

The spin originating from the nucleus is of particular interest in this thesis. Therefore, this section begins with an introduction to the nuclear spin and its ground state. The splitting of energy sublevels within the nuclear ground state is then described. Finally, nuclei with various spins are briefly listed.

#### 3.2.1 Nuclear Spin States

An important example of a system with multiple angular momenta is the nucleus. The nucleus possesses nuclear spin, and the nuclear spin quantum number is conventionally denoted as  $I$ . Except that the nucleus of  $^1\text{H}$  hydrogen contains a single proton and has spin  $I = 1/2$ , the spin of a nucleus is formed by combining the spins of  $1/2$  originating from both the protons and the neutrons, according to the usual rule in Eq. (3.5).

The nucleus containing exactly one proton and one neutron is  $^2\text{H}$  deuterium, which is used here as an example. The combination of the two spin- $1/2$  nucleons results in either nuclear spin  $I = 0$  or nuclear spin  $I = 1$ , as outlined in Section 3.1.3. These two nuclear spin states are found to have an energy difference of  $\sim 10^{11}$  kJ/mol. This figure essentially exceeds the energies available to usual electromagnetic fields or common chemical reactions, exemplified by the available thermal energy at room temperature of  $\sim 2.5$  kJ/mol). Therefore, for NMR experiments, the nuclear-excited states may be ignored, and only the lowest energy nuclear state (i.e. ground state) is considered. The value of  $I$  in ground state is called the ground state nuclear spin, referred to as the “nuclear spin” in this thesis for simplicity. In the case of deuterium, the nuclear spin is  $I = 1$ .

However, large nuclei, consisting of many nucleons, have many possible states, of which the ground state cannot be determined with a simple rule in general. Nevertheless, some properties can be derived from the following three rules:

1. Nuclei with odd mass numbers possess half-integer nuclear spin, and nuclei with even mass numbers possess integer nuclear spin, such as  $^1\text{H}$  ( $I = 1/2$ , 1 proton),  $^2\text{H}$  ( $I = 1$ , 1 proton and 1 neutron) and  $^{23}\text{Na}$  ( $I = 3/2$ , 11 protons and 12 neutrons). This is a direct consequence of Eq. (3.5).
2. If the numbers of protons and neutrons are both even, the nuclear spin is  $I = 0$ . For example, the  $^{16}\text{O}$  nucleus, containing eight protons and eight neutrons, has spin  $I = 0$ .
3. If the numbers of both protons and neutrons are odd, the nuclear spin is an integer larger than zero, such as  $^{40}\text{K}$  nuclear spin  $I = 4$  (19 protons, 21 neutrons).

The ground state nuclear spin and some other properties of some nuclei are shown in Table 3.1.

**Table 3.1** A selection of nuclei and their properties (Levitt 2008).

Nucleus	Ground-state spin	Natural abundance (%)	Gyromagnetic ratio ( $10^6 \text{ rad}\cdot\text{s}^{-1}\cdot\text{T}^{-1}$ )	NMR frequency at 7T (MHz)
$^1\text{H}$	1/2	~100	267.522	298.042
$^2\text{H}$	1	0.015	41.066	45.751
$^{13}\text{C}$	1/2	1.1	67.283	74.959
$^{15}\text{N}$	1/2	0.37	-27.126	-30.221
$^{17}\text{O}$	5/2	0.04	-36.281	-40.420
$^{19}\text{F}$	1/2	~100	251.815	280.543
$^{23}\text{Na}$	3/2	~100	70.808	78.886
$^{31}\text{P}$	1/2	~100	108.394	120.760
$^{35}\text{Cl}$	3/2	75.77	10.610	11.820
$^{129}\text{Xe}$	1/2	24.4	-74.521	-83.023
$^{12}\text{C}$	0	98.9	-	-
$^{16}\text{O}$	0	~100	-	-

### 3.2.2 Nuclear Zeeman Splitting

For all nuclei with nuclear spin  $I$ , there is  $(2I + 1)$ -fold degeneracy in the ground state. This degeneracy is broken if a magnetic field is applied. The splitting between the nuclear spin energy levels is called the nuclear Zeeman splitting. The spectroscopy technique that probes this splitting is NMR, as is discussed in this thesis.

In the presence of a magnetic field along the  $z$ -axis, the projection of the spin angular momentum  $\hat{S}$  on the  $z$ -axis,  $\hat{S}_z$ , is quantised:

$$\hat{S}_z = \hat{I}_z \hbar = m \hbar, \quad (3.6)$$

where  $m$  is the azimuthal quantum number, from the total  $(2I + 1)$  values of  $\{-I, -I + 1, \dots, I - 1, I\}$ ;  $\hbar$  is the reduced Planck constant;  $\hat{I}_z$  is a component of the angular momentum operator of a single spin,  $\hat{I}$ , in the Zeeman eigenbasis (more details in Section 3.4.2). Note that the operators used in quantum mechanics (e.g.  $\hat{S}_z$ ) are denoted by a hat (^) in this thesis. Figure 3.1 sketches the nuclear Zeeman sublevels of a  $^1\text{H}$  nucleus, a  $^{15}\text{N}$  nucleus and a  $^{23}\text{Na}$  nucleus with respect to the applied magnetic field. Both  $^1\text{H}$  and  $^{15}\text{N}$  nuclei possess spin- $1/2$ ; thus, their ground states split into two sublevels in the magnetic field (since  $2 \times (1/2) + 1 = 2$ ). The  $^{23}\text{Na}$  nucleus has spin- $3/2$ ; its ground state splits into four sublevels in the magnetic field (since  $2 \times (3/2) + 1 = 4$ ). The Zeeman splitting (i.e. the energy gap between the energy sublevels) of a  $^1\text{H}$  nucleus is much larger than that of a  $^{15}\text{N}$  nucleus in the same magnetic field. This is because the energy gap is relative to the magnetic properties of the nucleus, which will be discussed in Section 3.3.3.

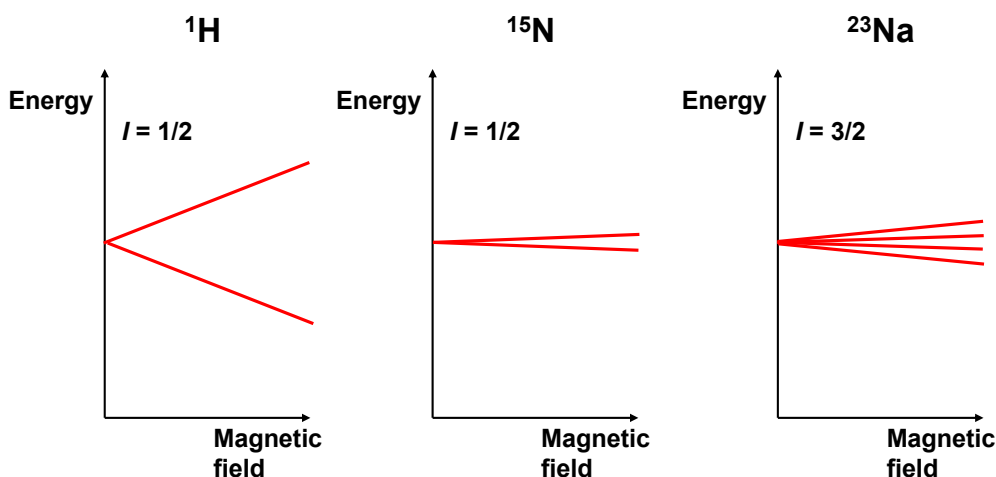


**Figure 3.1** Schematic of the nuclear Zeeman sublevels of the  $^1\text{H}$ ,  $^{15}\text{N}$  and  $^{23}\text{Na}$  nuclear ground states.

### 3.2.3 Nuclei with Various Spins

#### *Zero-spin nuclei*

The periodic table lists 118 elements. A minority of these isotopes have a nuclear spin of  $I = 0$  and display no nuclear Zeeman splitting effect. Therefore, they cannot be detected by NMR. Unfortunately, organic matter contains many spin-free isotopes, such as  $^{12}\text{C}$ ,  $^{16}\text{O}$  and  $^{32}\text{S}$ .

#### *Spin-1/2 nuclei*

For in vivo NMR spectroscopy, other nuclei with non-zero spin in the organic materials must be used, such as  $^1\text{H}$ ,  $^{31}\text{P}$ ,  $^{15}\text{N}$  and  $^{19}\text{F}$ . These are spin- $1/2$  nuclei. Such nuclei are spherical in shape and have convenient magnetic properties. They are typically scattered on the right-hand

side of the periodic table. The  $^1\text{H}$  nucleus is of particular importance; standard clinical applications of NMR and MRI are based on signals from this nucleus.

### ***Quadrupolar nuclei***

Nuclei with spin  $I > 1/2$  are known as “quadrupolar nuclei” because their electric charge distribution is not spherically symmetrical. The NMR of such nuclei is a more prosperous but complicated field than that of spin- $1/2$  nuclei. Quadrupolar nuclei with integer spin are uncommon, the most abundant nucleus of which is  $^{14}\text{N}$  with a natural abundance of almost 100%. The  $^{176}\text{Lu}$  has the highest nuclear spin,  $I = 7$ , in the periodic table. Quadrupolar nuclei with half-integer spin are common, such as  $^{23}\text{Na}$  with  $I = 3/2$ ,  $^{25}\text{Mg}$  with  $I = 5/2$  and  $^{133}\text{Cs}$  with  $I = 7/2$ . With a natural abundance of  $\sim 100\%$ , sodium plays a crucial role in cell physiology, making it an attractive target for in vivo NMR and MRI.

## **3.3 Magnetism**

Magnetism is another intrinsic physical property of particles. Magnetic nuclei interact with magnetic fields. The extremely weak magnetic interactions of atomic nuclei can provide detailed molecular information currently unobtainable by any other methods. This section starts with a brief introduction to the electromagnetic field. Furthermore, macroscopic and microscopic magnetism are introduced, followed by spin precession and Larmor frequency concepts. The longitudinal and transverse magnetisation and relaxation are then discussed in detail. Finally, the creation of the NMR signal is briefly illustrated.

### **3.3.1 The Electromagnetic Field**

Either a classical or a quantum description can be used for electromagnetic fields. In the classical description, the electromagnetic field is represented by two vector fields,  $\mathbf{E}$  and  $\mathbf{B}$ , at each point in space. The electric field,  $\mathbf{E}$ , interacts with electric charges. The magnetic field,  $\mathbf{B}$ , interacts with magnetic moments. The behaviour of these two vector fields in time and space is governed by Maxwell’s equations. The quantum description, where the field is treated as a collection of photons, is accurate but difficult to use. Nevertheless, the discrepancy between these two descriptions is negligible, and the simpler classical formalism is preferable whenever possible.

### **3.3.2 Macroscopic Magnetism**

In general, all matter is magnetic, i.e. has the capability to interact with magnetic fields. Such interaction is usually represented by its associated magnetic moment,  $\mu$ . Some substances have

a permanent magnetic moment, such as a bar magnet or a compass needle. However, most substances exhibit induced magnetism and have a magnetic moment only in an external magnetic field. The magnetic energy,  $E_{\text{mag}}$ , of a small object in a magnetic field,  $\mathbf{B}$ , is given by:

$$E_{\text{mag}} = -\boldsymbol{\mu} \cdot \mathbf{B}. \quad (3.7)$$

The magnetic energy of a large object should be obtained by integrating this equation over its volume. The magnetic energy is lowest (highest) if the magnetic moment is parallel (anti-parallel) to the magnetic field.

For substances with an induced magnetic moment, the equilibrium state of the induced moment,  $\boldsymbol{\mu}_{\text{induced}}$ , in the applied magnetic field,  $\mathbf{B}$ , is given by:

$$\boldsymbol{\mu}_{\text{induced}} = \mu_0^{-1} V \chi \mathbf{B}, \quad (3.8)$$

where  $\mu_0$  is a constant called vacuum permeability;  $V$  is the volume of the object; and  $\chi$  is the magnetic susceptibility of the material. This susceptibility, which can be positive or negative, determines how an applied magnetic field is distorted. Paramagnetic materials with a positive  $\chi$  tend to pull the magnetic field into the material. Most materials are found to have a negative  $\chi$  and are called diamagnetic. In diamagnetic objects, the magnetic field tends to be pushed out of the material.

#### 3.3.3 Microscopic Magnetism

The magnetism of substances has three sources: (1) the circulation of electric currents, (2) the magnetic moments of the electrons and (3) the magnetic moments of the atomic nuclei. The first two electronic contributions are almost always many orders of magnitude larger than the third nuclear contribution. The first source results in a negative value to the susceptibility, whereas the second and third sources add a positive value.

The first contribution can be understood simply from the motion of electrons in their atomic orbits. For example, the electron circulates the proton in a hydrogen atom, forming a small “current loop” that generates a magnetic field. In contrast, the second and third contributions are intrinsic properties. Like elementary particles intrinsically possess a spin, they also intrinsically possess a permanent magnetism. In quantum mechanics, their spin angular momentum,  $\hat{\mathbf{S}}$ , and their magnetic moment,  $\hat{\boldsymbol{\mu}}$ , are proportional to each other:



$$\hat{\mu} = \gamma \hat{S}, \quad (3.9)$$

where the proportionality constant,  $\gamma$ , is called the gyromagnetic ratio. It may have either sign: A positive (negative) value indicates that the magnetic moment is parallel (anti-parallel) to the spin angular momentum. The gyromagnetic ratios of some nuclei commonly employed by in vivo NMR and MRI are shown in Table 3.1.

In the presence of a magnetic field  $\mathbf{B}_0$ , which direction is defined as the  $z$ -direction or longitudinal direction, the projection of  $\hat{\mu}$  on the  $z$ -axis,  $\hat{\mu}_z$ , amounts to  $(2I + 1)$  values according to Eq. (3.6). Each  $\hat{\mu}_z$  corresponds to a nuclear Zeeman sublevel with an azimuthal quantum number,  $m$ . The energy of this sublevel,  $E_m$ , is given by:

$$E_m = -\hat{\mu}_z \cdot B_0 = -\gamma B_0 \hbar \hat{I}_z = -\gamma \hbar m B_0. \quad (3.10)$$

Therefore, the energy gap between the two adjacent nuclear Zeeman sublevels is  $\Delta E = \gamma B_0 \hbar$ , as shown in Figure 3.2b.

### 3.3.4 Spin Precession and Larmor Frequency

Any particle with spin possesses an associated angular momentum. This angular momentum is a vector and may point in any possible direction in space. The direction of this vector is called the spin polarisation axis. The magnetic moment of a nucleus with a positive (negative)  $\gamma$  value points in the same (opposite) direction to the spin polarisation axis. In the absence of a magnetic field, a sample in equilibrium has an isotropic distribution of magnetic moments, meaning that its spin polarisation axes are randomly oriented in space. When an external magnetic field is applied, the magnetic moment of the spin moves around the magnetic field, keeping a constant angle between the spin magnetic moment and the field, as if the magnetic moment is moving around a cone. This motion is called precession. The angle of the precession cone depends only on the initial spin polarisation.

The precession frequency of a particle with spin angular momentum,  $\omega_0$ , is equal to:

$$\omega_0 = -\gamma B_0. \quad (3.11)$$

For nuclear spins,  $\omega_0$  is called the nuclear Larmor frequency. It is proportional to the strength of the applied magnetic field. Consequently, different magnetic field strengths require different RadioFrequency (RF) hardware in NMR or MRI experiments. Similarly, since  $\gamma$  is an intrinsic property of nuclei, different nuclei require different RF hardware at the same field strength.

The Larmor frequencies of some ordinary nuclei in a typical static main field of 7T are given in Table 3.1.

#### 3.3.5 Spin-Lattice Relaxation: Nuclear Paramagnetism

Consider the simple model of  $^1\text{H}$  nuclei in a sample of water. In the absence of an external magnetic field, the nuclei in the sample have spin polarisation axes that point to all possible directions in space. The total magnetic moment of this sample is very close to zero because, due to the enormous number of nuclear spins in the sample, there are approximately the same number of spins pointing in and against a given direction.

If an external magnetic field is applied, all nuclei start executing Larmor precession around the field. This precessional motion alone does not change the total magnetic moment of the sample – it remains zero. This is because the isotropic distribution of spin polarisations does not contribute to the magnetism of the material.

However, each nucleus is part of a larger molecule containing other magnetic particles: Electrons and nuclei are sources of magnetic fields. At room temperature, all molecules undergo violent rotations and collisions. Still, this motion has little effect on the spin precession of the nucleus. Only the local magnetic fields from the molecular environment slightly influence the nuclear spins. These fields are microscopic compared to the external magnetic field and fluctuate rapidly due to the thermal motion of the environment. Consequently, each spin experiences a slightly fluctuating total magnetic field. This fluctuation affects both magnitude and direction; therefore, the spin polarisation axis of every nuclear spin is slightly changed at any given time. As a result, over a long time, the magnetic moment of each spin wanders around, moving between different “precession cones” and eventually sampling all possible orientations. This wandering motion (on the order of seconds) is much slower than the precessional motion (on the order of nanoseconds).

Note that the wandering motion is not completely isotropic. Since the sample is at a finite temperature, the nuclear spin is slightly more likely to be driven towards an orientation with low magnetic energy, i.e. with magnetic moment parallel to the magnetic field (Eq. (3.7)). After sufficient time, the biased wandering motion leads to a stable anisotropic distribution of nuclear spin polarisations, called thermal equilibrium. This anisotropy points in a direction such that the sample has the lowest magnetic energy, e.g.  $^{23}\text{Na}$  ( $^{17}\text{O}$ ) nuclear spins parallel (anti-parallel) to the external magnetic field. As a result, the entire sample acquires a small net magnetic

moment along the external magnetic field, i.e. a longitudinal magnetic moment (Figure 3.2a). This is the microscopic mechanism of nuclear paramagnetism.

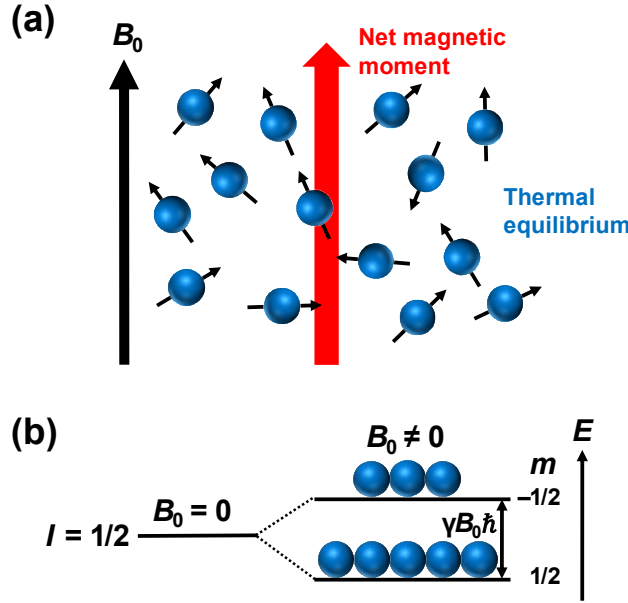


**Figure 3.2** Schematic of thermal equilibrium. **(a)** Longitudinal magnetisation parallel to the external magnetic field  $B_0$ . **(b)** Boltzmann distribution of populations for the spin-1/2 ensemble (positive  $\gamma$ ), with the lower energy Zeeman sublevel being more populated.

Quantum statistical mechanics states that, at any thermal equilibrium temperature,  $T$ , there is no net transfer between the nuclear Zeeman energy sublevels; and the populations of spins in the energy sublevels obey the Boltzmann distribution (Figure 3.2b). As described by Boltzmann distribution, the number of nuclear spins in each energy sublevel is proportional to  $\exp(E_m/kT) = \exp(\gamma \hbar m B_0/kT)$ , where  $k = 1.38066 \times 10^{-23} \text{ J/K}$  is the Boltzmann constant. Therefore, in a sample containing  $N$  nuclear spins, the longitudinal magnetisation in thermal equilibrium,  $M_0$ , is given by:

$$M_0 = N \gamma \hbar \frac{\sum_{m=-I}^I m \exp(\gamma B_0 m \hbar / kT)}{\sum_{m=-I}^I \exp(\gamma B_0 m \hbar / kT)}. \quad (3.12)$$

Assuming the external magnetic field is turned on at  $t_{\text{on}}$  along  $z$ -axis, the temporal evolution of this macroscopic longitudinal magnetisation,  $M_z$ , is formulated as:

$$M_z(t) = M_0 \left( 1 - e^{-\frac{t-t_{\text{on}}}{T_1}} \right), \quad (3.13)$$

for  $t > t_{\text{on}}$ . The exponential time constant  $T_1$  (typically in milliseconds to seconds) is known as either the spin-lattice relaxation time constant or the longitudinal relaxation time constant. The

term “relaxation” indicates the re-establishment of thermal equilibrium after some perturbation is applied.

### 3.3.6 Transverse Magnetisation and Transverse Relaxation

The longitudinal nuclear spin magnetisation along the field, as described above, is almost undetectable due to its small magnitude. Therefore, the voltage induced by the magnetisation perpendicular to the external magnetic field is measured in NMR and MRI experiments. However, such magnetisation does not exist in thermal equilibrium. When the polarisation of every spin is suddenly rotated by  $90^\circ$  by applying an appropriate RF pulse (i.e. an oscillating magnetic field), the entire nuclear magnetisation distribution of the sample is also rotated by  $90^\circ$  (Figure 3.3a). The pulse equalises the spin populations of Zeeman energy sublevels and converts the population difference into net transfer between the Zeeman energy sublevels (Figure 3.3b). As a result, the net spin polarisation along the field (along the  $z$ -axis) is transferred into the net spin polarisation along an axis perpendicular to the magnetic field (along the  $y$ -axis). The resulting net magnetic moment perpendicular to the magnetic field is called transverse magnetisation.

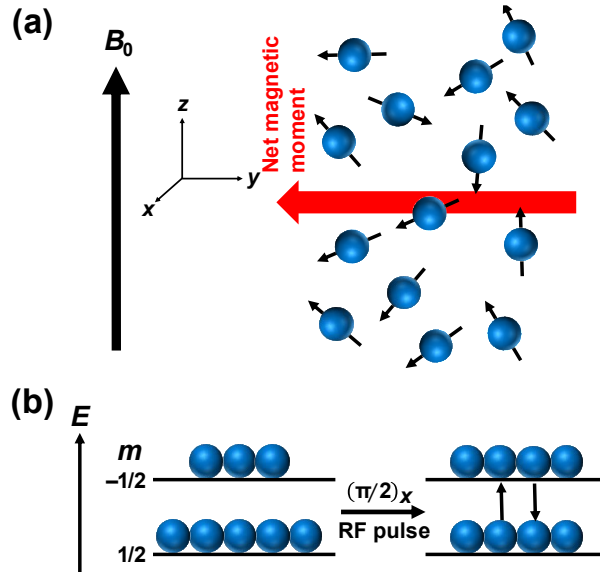


**Figure 3.3** Polarisation distribution immediately after an RF pulse. **(a)** Transverse magnetisation perpendicular to the external magnetic field  $B_0$ . **(b)** Two Zeeman sublevels for spin-1/2 ensemble with equal spin populations and net transfer between them after the RF pulse excitation.

This macroscopic transverse magnetisation,  $M_{xy}$ , rotates in the  $xy$ -plane at the nuclear Larmor frequency,  $\omega_0$ .  $M_{xy}$  at a time,  $t$ , after the RF pulse excitation is expressed as:

$$M_{xy}(t) = M_0 \cdot e^{-i\omega_0 t} \cdot e^{-\frac{t}{T_2}}. \quad (3.14)$$

The equilibrium magnetisation,  $M_0$ , precesses in the  $xy$ -plane at the Larmor frequency  $\omega_0$ , represented by the first complex exponential term. The second exponential term describes the decay of transverse magnetisation. The macroscopic transverse magnetisation decays slowly due to the loss of coherence between the precessing microscopic nuclear magnetic moments. All spin polarisation axes in the sample are perfectly in phase (i.e. coherent) just after the RF pulse; however, due to the surrounding microscopic fluctuating magnetic fields, the different spins precess at slightly different frequencies, so the spins are gradually out of phase with each other (i.e. loss of coherence). This decay process is irreversible. The time constant  $T_2$  is often called the transverse relaxation time constant or spin-spin relaxation time constant. For small molecules in liquids,  $T_2$  is typically of the same order of magnitude as  $T_1$ , i.e. seconds. In other cases, such as for large molecules in liquids or solids,  $T_2$  may be as short as milliseconds.

### 3.3.7 NMR Signal

The precessing transverse magnetisation after the RF pulse excitation is detectable despite its small magnitude because it oscillates at a well-defined frequency – the Larmor frequency. As a rotating magnetic moment, transverse magnetisation produces a rotating magnetic field. The changing magnetic field is associated with an electric field, as described by Faraday's law of induction. Suppose that a wire coil is near the sample. In this case, the electric field moves the electrons in the wire, i.e. an oscillating electric current flows in the wire (Figure 3.4).

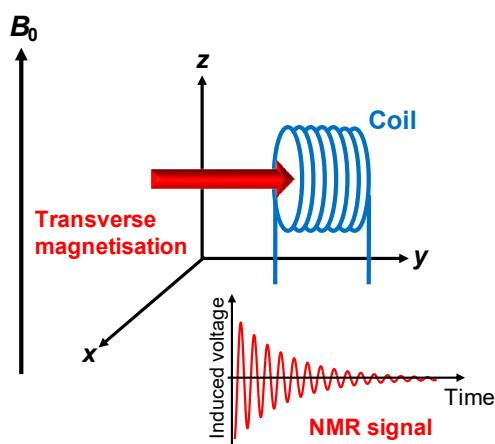


**Figure 3.4** The induction of an NMR signal.

The oscillating electric current induced by the precessing transverse magnetisation is often called an NMR signal or free induction decay. It can be detected using a receiver chain, i.e. the hardware components that convert the received signal into digital data and go through several filtering steps to maximise the Signal-to-Noise Ratio (SNR) from the sample.

In summary, a typical NMR spectrometer is basically a device capable of (1) magnetising nuclear spins with a large external magnetic field; (2) generating transverse nuclear magnetisation by rotating spin polarisation axes with RF pulses; and (3) detecting small oscillating electric currents induced by the precessing transverse magnetisation.

#### 3.4 Spin-1/2 Dynamics

This section provides classical and quantum mechanical descriptions of the spin-1/2 ensemble dynamics. In most cases, a classical treatment adequately describes the macroscopic behaviour of the spin-1/2 ensemble dynamics in a concise manner. However, quantum mechanics provides a rigorous and accurate description of the spin-1/2 ensemble dynamics, which can be generalised to quadrupolar spin systems such as the spin-3/2 ensemble. The quantum mechanical descriptions of spin-1/2 dynamics mainly follow Chapter 2 of the book of (Slichter 1990).

##### 3.4.1 Classical Description

Bloch introduced the magnetisation vector,  $\mathbf{M}$ , to represent the sum of all magnetic moments per unit volume:  $\mathbf{M} = \sum \boldsymbol{\mu}_i / \Delta V$  (Bloch et al. 1946). If the magnetisation vector is placed in an applied external magnetic field,  $\mathbf{B}$ , a torque,  $\mathbf{L} = \mathbf{M} \times \mathbf{B}$ , acts on the magnetisation vector. The motion of  $\mathbf{M}$  is given by:

$$\frac{d\mathbf{M}}{dt} = \gamma \mathbf{L} = \gamma (\mathbf{M} \times \mathbf{B}). \quad (3.15)$$

According to Eq. (3.8), in the presence of a static main external  $\mathbf{B}_0$  field, the magnetisation vector  $\mathbf{M}$  in thermal equilibrium is equal to  $M_0 = \frac{\chi}{\mu_0} B_0$  along the  $z$ -axis. In this case,  $\mathbf{M}$  precesses with a fixed angle around the  $\mathbf{B}_0$  field at the Larmor frequency of  $\omega_0 = -\gamma B_0$ . This motion is given by:

$$\frac{d\mathbf{M}}{dt} = \gamma \mathbf{M} \times \mathbf{B}_0. \quad (3.16)$$

The thermal equilibrium is perturbed by applying an oscillating external magnetic field,  $\mathbf{B}_1$ , in the  $xy$  (transverse) plane at the resonance frequency,  $\omega = -\gamma B_0$ . Effectively,  $\mathbf{B}_1$  applies a torque which rotates  $\mathbf{M}$  by a prescribed angle dependent on the strength of  $\mathbf{B}_1$  (typically a few microteslas) and its duration (typically several milliseconds), as shown in Figure 3.5a. The motion equation in this case is given by:

$$\frac{d\mathbf{M}}{dt} = \gamma \mathbf{M} \times (\mathbf{B}_0 + \mathbf{B}_1). \quad (3.17)$$

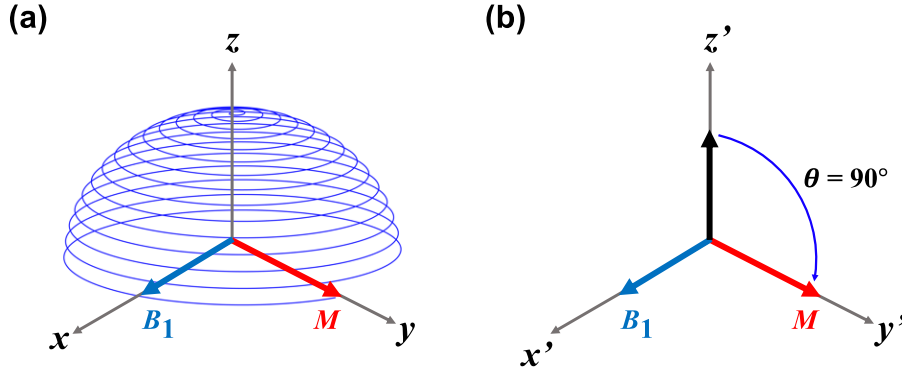


**Figure 3.5**  $B_1$  field induces rotation of magnetisation vector  $M$  towards transverse plane in (a) the laboratory frame and (b) the rotating frame. Strength and duration of  $B_1$  is set for a  $90^\circ$ -rotation, leaving  $M$  entirely in the transverse plane.

Relaxation back to thermal equilibrium also occurs, in which the transverse and longitudinal components of  $M$ ,  $M_{xy}$  and  $M_z$ , do not remain constant over time. As proposed by (Bloch et al. 1946), the longitudinal relaxation time constant,  $T_1$ , is used to characterise the return of  $M_z$ , while the transverse relaxation time constant,  $T_2$ , is used to characterise the decay of  $M_{xy}$ :

$$\begin{cases} \frac{dM_z}{dt} = -\frac{M_z - M_0}{T_1} \\ \frac{dM_{xy}}{dt} = -\frac{M_{xy}}{T_2} \end{cases}. \quad (3.18)$$

Bloch supposed that the behaviour of the magnetisation vector,  $M$ , is governed by the torque from external magnetic fields and longitudinal/transverse relaxation (Bloch et al. 1946). This is described phenomenologically by the so-called Bloch equation:

$$\frac{d\mathbf{M}}{dt} = \gamma(\mathbf{M} \times \mathbf{B}) - \frac{M_x \mathbf{i} + M_y \mathbf{j}}{T_2} - \frac{M_z - M_0}{T_1} \mathbf{k}, \quad (3.19)$$

where  $\mathbf{i}$ ,  $\mathbf{j}$  and  $\mathbf{k}$  are unit vectors in the  $x$ ,  $y$  and  $z$  directions, respectively.  $M_0$  is the equilibrium magnetisation vector arising from the static main field,  $B_0$ .  $\mathbf{B}$  includes the various applied magnetic fields.

For convenience, the laboratory frame is transformed into a frame of reference rotating about the  $z$ -axis at the frequency  $\omega$  of the  $B_1$  excitation field. Figure 3.5, which compares the behaviours in the laboratory and rotating frames, illustrates the simplification afforded by the rotating frame representation. Ignoring the relaxation contribution, the Bloch equation in the rotating frame is given by (more details in Chapter 6 in the book of (Nishimura 2010)):

$$\frac{d\mathbf{M}}{dt} = \gamma \mathbf{M} \times \mathbf{B}_{\text{eff}}, \quad (3.20)$$

where  $\mathbf{B}_{\text{eff}} = \mathbf{B}_0 - \frac{\omega}{\gamma} + \mathbf{B}_1$  is the effective field. This equation indicates that if the rotating frame rotates at the Larmor frequency  $\omega = \omega_0 = -\gamma \mathbf{B}_0$  (i.e. at the magnetic resonance condition),  $\mathbf{B}_0$  is not seen by  $\mathbf{M}$  in the rotating frame. In this case,  $\mathbf{M}$  only rotates around  $\mathbf{B}_1$  that is applied along the  $x$ -axis, as shown in Figure 3.5b. The effective field becomes:

$$\mathbf{B}_{\text{eff}} = \mathbf{B}_1 + \left( \mathbf{B}_0 - \frac{\omega}{\gamma} \right) = B_1 \mathbf{i} + \left( B_0 - \frac{\omega}{\gamma} \right) \mathbf{k}. \quad (3.21)$$

By substituting Eq. (3.21) to Eq. (3.20), the Bloch equation with the contribution of relaxation in the rotating frame becomes:

$$\begin{cases} \frac{dM_x}{dt} = M_y(\omega - \omega_0) - \frac{M_x}{T_2} \\ \frac{dM_y}{dt} = -\omega_1 M_z - M_x(\omega - \omega_0) - \frac{M_y}{T_2} \\ \frac{dM_z}{dt} = M_y \omega_1 + \frac{M_0 - M_z}{T_1} \end{cases} \quad (3.22)$$

Note that the Bloch equation can only adequately represent the magnetisation dynamics in less viscous liquid samples. Quantum mechanics is required to accurately describe the spin ensemble dynamics in highly viscous liquid or solid samples.

### 3.4.2 Quantum Mechanical Description

#### *Schrödinger Equation*

In a quantum mechanical treatment, a spin-1/2 nucleus has two Zeeman eigenstates:  $\left| \frac{1}{2}, +\frac{1}{2} \right\rangle$  and  $\left| \frac{1}{2}, -\frac{1}{2} \right\rangle$ . The angular momentum operator of a single spin-1/2,  $\hat{\mathbf{I}}$ , has three components in the Zeeman eigenbasis:  $\hat{I}_x$ ,  $\hat{I}_y$  and  $\hat{I}_z$ . These three components fulfil the condition:  $\hat{I}^2 = \hat{I}_x^2 + \hat{I}_y^2 + \hat{I}_z^2$ , and obey the Pauli matrices,  $\hat{I}_{x,y,z} = \hbar/2 \cdot \hat{\sigma}_{x,y,z}$ :

$$\hat{I}_x = \frac{1}{2} \begin{pmatrix} 0 & 1 \\ 1 & 0 \end{pmatrix}, \quad \hat{I}_y = \frac{1}{2i} \begin{pmatrix} 0 & 1 \\ -1 & 0 \end{pmatrix}, \quad \hat{I}_z = \frac{1}{2} \begin{pmatrix} 1 & 0 \\ 0 & -1 \end{pmatrix}. \quad (3.23)$$

The quantum state of a spin system at time,  $t$ , is described by a wave function,  $\psi(t)$ . It is either a stationary eigenstate or an un-stationary superposition state. All internal and external interactions on a spin system are represented by a Hermitian operator, known as Hamiltonian,  $\hat{H}$ . For example, the Hamiltonian for the interaction of each spin with the static longitudinal



field  $B_0$  is given by  $\hat{H}^{\text{static}} = -\gamma\hbar B_0 \hat{I}_z$ . The dynamics of the spin system are given by solving the following Schrödinger equation:

$$\frac{d}{dt}\psi(t) = -i\hbar^{-1}\hat{H}\psi(t). \quad (3.24)$$

### *Spin in a Static Field*

As described in Section 3.3.3, a spin in a static field  $B_0$  gives energies,  $E_m = -\gamma\hbar m B_0$ , in terms of the azimuthal quantum number,  $m$ . The energy is an eigenvalue of the component of spin  $\hat{I}_z$  parallel to the static  $B_0$  field. The corresponding eigenfunction (i.e. wave function) of the time-independent Schrödinger equation is denoted by  $u_{I,m}$ . The time-dependent solution corresponding to a particular value of  $m$  is  $\psi_{I,m}(t) = u_{I,m}e^{-(i/\hbar)E_m t}$ . The most general time-dependent solution is therefore:

$$\psi(t) = \sum_{m=-I}^{+I} c_m u_{I,m} e^{-(i/\hbar)E_m t}. \quad (3.25)$$

where  $c_m$ 's are complex constants. The expectation value of any observable may be computed using the wave function,  $\psi(t)$ , as the  $x$ -component of the spin magnetic moment  $\hat{\mu}$ ,  $\hat{\mu}_x$ , is given by:

$$\langle \hat{\mu}_x(t) \rangle = \int \psi^*(t) \hat{\mu}_x \psi(t) d\tau. \quad (3.26)$$

By using the fact that  $\hat{\mu}_x = \gamma\hbar \hat{I}_x$ , and that  $\psi(t)$  is given by Eq. (3.25),  $\langle \hat{\mu}_x(t) \rangle$  is extended as:

$$\langle \hat{\mu}_x(t) \rangle = \sum_{m,m'} \gamma\hbar c_{m'}^* c_m (m'|\hat{I}_x|m) e^{(i/\hbar)(E_{m'} - E_m)t}, \quad (3.27)$$

where  $(m'|\hat{I}_x|m)$  defined as  $(m'|\hat{I}_x|m) \equiv \int u_{I,m'}^* \hat{I}_x u_{I,m} d\tau$  is a time-independent matrix element. Expressions similar to Eq. (3.27) would hold for any operator, such as  $y$ - and  $z$ -components of the spin magnetic moment  $\hat{\mu}$ ,  $\hat{\mu}_y$  and  $\hat{\mu}_z$ . It is denoted that the expectation value will generally be time-dependent, consisting of a number of terms oscillating harmonically, and that the possible frequencies  $\frac{E_{m'} - E_m}{\hbar}$  correspond exactly to the frequency of absorption or emission between states  $m$  and  $m'$ . This denotation is based on the Heisenberg and Born's formulation of the quantum theory in matrix form, with the assumption that observable properties of any quantum system must be given by expressions such as Eq. (3.27).

Since matrix elements  $(m'|\hat{I}_x|m)$  vanish unless  $m' = m \pm 1$ , all the terms of Eq. (3.27) have an angular frequency of either  $-\gamma B_0$  or  $\gamma B_0$ . Their sum must also contain just  $\gamma B_0$ . The expectation value,  $\langle \hat{\mu}_x(t) \rangle$ , therefore oscillates in time at the classical Larmor precession frequency,  $\omega_0 = \gamma B_0$ .

Here, it is convenient to introduce the well-known raising and lowering operators,  $\hat{I}^+ \equiv \hat{I}_x + i\hat{I}_y$  and  $\hat{I}^- \equiv \hat{I}_x - i\hat{I}_y$ , respectively. Accordingly,  $I_x$  and  $I_y$  can be expressed as:  $\hat{I}_x = \frac{1}{2}(\hat{I}^+ + \hat{I}^-)$  and  $\hat{I}_y = \frac{1}{2i}(\hat{I}^+ - \hat{I}^-)$ . The operators are called “raising” or “lowering” because of the effect they produce when they operate on a function  $u_{I,m}$ :

$$\begin{cases} \hat{I}^+ u_{I,m} = \sqrt{I(I+1) - m(m-1)} u_{I,m+1} \\ \hat{I}^- u_{I,m} = \sqrt{I(I+1) - m(m+1)} u_{I,m-1} \end{cases} \quad (3.28)$$

$\hat{I}^+$  (or  $\hat{I}^-$ ) turns  $u_{I,m}$  into a function whose  $m$  value has been raised (or lowered) by one unit. Therefore,  $(m'|\hat{I}^+|m)$  vanishes unless  $m' = m + 1$ , whereas  $(m'|\hat{I}^-|m)$  vanishes unless  $m' = m - 1$ . This indicates that the  $\hat{I}_x$  and  $\hat{I}_y$  operators can induce transfer only between the neighbouring eigenstates.

Consider the form of Eq. (3.27) takes for a spin-1/2. Given that the diagonal matrix elements of  $\hat{I}_x$  vanish,  $\langle \hat{\mu}_x(t) \rangle$  is given as:

$$\langle \hat{\mu}_x(t) \rangle = \gamma \hbar \left[ c_{1/2}^* c_{-1/2} \left( \frac{1}{2} \left| \hat{I}_x \right| - \frac{1}{2} \right) e^{-i\gamma B_0 t} + c_{-1/2}^* c_{1/2} \left( -\frac{1}{2} \left| \hat{I}_x \right| \frac{1}{2} \right) e^{i\gamma B_0 t} \right]. \quad (3.29)$$

Given that the Larmor frequency  $\omega_0 = \gamma B_0$  and  $\left( \frac{1}{2} \left| \hat{I}_x \right| - \frac{1}{2} \right)$  is the conjugate of  $\left( -\frac{1}{2} \left| \hat{I}_x \right| \frac{1}{2} \right)$ ,  $\langle \hat{\mu}_x(t) \rangle$  is simplified as:

$$\langle \hat{\mu}_x(t) \rangle = 2\gamma \hbar \operatorname{Re} \left\{ \left[ c_{1/2}^* c_{-1/2} \left( \frac{1}{2} \left| \hat{I}_x \right| - \frac{1}{2} \right) \right] e^{-i\omega_0 t} \right\}. \quad (3.30)$$

where the symbol “Re” signifies “take the real part of”. According to Eq. (3.28) and  $\hat{I}_x = \frac{1}{2}(\hat{I}^+ + \hat{I}^-)$ ,  $\left( \frac{1}{2} \left| \hat{I}_x \right| - \frac{1}{2} \right)$  is equal to  $\frac{1}{2}$ . Here,  $c_{1/2}$  and  $c_{-1/2}$  is expressed as:  $c_{1/2} = ae^{i\alpha}$  and  $c_{-1/2} = be^{i\beta}$ . The normalisation of the wave function gives  $a^2 + b^2 = 1$ . Therefore,  $\langle \hat{\mu}_x(t) \rangle$  is given in Eq. (3.31). Similarly,  $\langle \hat{\mu}_y(t) \rangle$  and  $\langle \hat{\mu}_z(t) \rangle$  are also given in Eq. (3.31):

$$\begin{cases} \langle \hat{\mu}_x(t) \rangle = \gamma \hbar ab \cos(\alpha - \beta - \omega_0 t) \\ \langle \hat{\mu}_y(t) \rangle = -\gamma \hbar ab \sin(\alpha - \beta + \omega_0 t) \\ \langle \hat{\mu}_z(t) \rangle = \gamma \hbar (a^2 - b^2)/2 \end{cases} \quad (3.31)$$

Eq. (3.31) indicates that both  $\langle \hat{\mu}_x(t) \rangle$  and  $\langle \hat{\mu}_y(t) \rangle$  oscillate in time at the Larmor frequency  $\omega_0 = \gamma B_0$ , whereas  $\langle \hat{\mu}_z(t) \rangle$  is independent of time. Moreover, the maximum amplitude of  $\langle \hat{\mu}_x(t) \rangle$  and  $\langle \hat{\mu}_y(t) \rangle$  are the same. The expectation value of  $\hat{\mu}$  is defined as  $\langle \hat{\mu} \rangle \equiv i \langle \hat{\mu}_x \rangle + j \langle \hat{\mu}_y \rangle + k \langle \hat{\mu}_z \rangle$ . Given that  $\hat{\mu}_x^2 + \hat{\mu}_y^2 = \text{constant}$ , it can be seen that  $\langle \hat{\mu} \rangle$  behaves like a vector that precesses in the  $xy$ -plane at a fixed angle with the  $z$ -direction.

### Equations of Motion of the Expectation Value

The correspondence between the classical and quantum mechanical treatments becomes especially clear by examining a differential equation related to the temporal variations of the expectation values,  $\langle \hat{\mu}_x \rangle$ ,  $\langle \hat{\mu}_y \rangle$  and  $\langle \hat{\mu}_z \rangle$ .

Suppose that a pair of wave functions,  $\psi(t)$  and  $\phi(t)$ , are both solutions of the same Schrödinger equation in Eq. (3.24), i.e.  $-\frac{\hbar}{i} \frac{d\psi}{dt} = \hat{H}\psi$  and  $-\frac{\hbar}{i} \frac{d\phi}{dt} = \hat{H}\phi$ . In case that some operator,  $F$ , has no explicit time dependence, then:

$$\frac{d}{dt} \int \phi^* F \psi d\tau = \int \frac{d\phi^*}{dt} F \psi d\tau + \int \phi^* F \frac{d\psi}{dt} d\tau = \frac{i}{\hbar} \int \phi^* (\hat{H}F - F\hat{H}) \psi d\tau. \quad (3.32)$$

Since  $F$  is time independent, the operator,  $\frac{dF}{dt}$ , is defined by  $\int \phi^* \frac{dF}{dt} \psi d\tau = \frac{d}{dt} \int \phi^* F \psi d\tau$ . Therefore,  $\frac{dF}{dt}$  is given by:

$$\frac{dF}{dt} = \frac{i}{\hbar} [\hat{H}, F], \quad (3.33)$$

where  $[\hat{H}, F]$  is the usual commutator,  $\hat{H}F - F\hat{H}$ . The time derivative of the expectation values of  $\hat{\mu}_x$ ,  $\hat{\mu}_y$  and  $\hat{\mu}_z$  can be computed using this equation. Given that the Hamiltonian of the static  $B_0$  field is  $\hat{H}^{\text{static}} = -\gamma \hbar B_0 \hat{I}_z$  and that three components of spin angular momentum cyclically commute, i.e.  $[\hat{I}_x, \hat{I}_y] = i\hat{I}_z$  (further reading in Section 7.6.1 of (Levitt 2008)), the time derivative of the  $x$ -component of spin angular momentum is given by:

$$\frac{d\hat{I}_x}{dt} = \frac{i}{\hbar} [\hat{H}^{\text{static}}, \hat{I}_x] = -\gamma B_0 i [\hat{I}_z, \hat{I}_x] = \gamma B_0 \hat{I}_y. \quad (3.34)$$

Similarly,  $\frac{d\hat{J}_y}{dt} = \gamma B_0 \hat{J}_x$  and  $\frac{d\hat{J}_z}{dt} = 0$ . These equations are the component equations of the vector operator equation:  $\frac{d\hat{\mathbf{J}}}{dt} = \gamma \hat{\mathbf{J}} \times \mathbf{B}_0$ , where  $\frac{d\hat{\mathbf{J}}}{dt} = \mathbf{i} \frac{d\hat{J}_x}{dt} + \mathbf{j} \frac{d\hat{J}_y}{dt} + \mathbf{k} \frac{d\hat{J}_z}{dt}$ .

Since the magnetic moment of a single spin is  $\hat{\boldsymbol{\mu}} = \gamma \hbar \hat{\mathbf{J}}$ , the expectation value of the magnetic moment is given by:

$$\frac{d\langle \hat{\boldsymbol{\mu}} \rangle}{dt} = \gamma \langle \hat{\boldsymbol{\mu}} \rangle \times \mathbf{B}_0. \quad (3.35)$$

This equation of motion obeys the classical Bloch equation. For a spin ensemble with a magnetic moment,  $\hat{\boldsymbol{\mu}}_k$ , for the  $k^{\text{th}}$  spin, its total magnetic moment is  $\hat{\boldsymbol{\mu}} = \sum_k \hat{\boldsymbol{\mu}}_k$ . If the spins do not interact with one another, Eq. (3.35) also holds for the expectation value of the total magnetisation.

Note that Eq. (3.35) is also valid for a time-dependent magnetic field, not simply a static field. This allows one to use a classical picture for studying the effects produced by alternating magnetic fields.

### *Effect of Alternating Magnetic Fields*

Suppose that an alternating magnetic field,  $\mathbf{B}_1(t) = B_1(\mathbf{i} \cos \omega_1 t + \mathbf{j} \sin \omega_1 t)$ , is applied along the  $x$ -axis.  $\mathbf{B}_1$  oscillates at the frequency  $\omega_1$  along the  $z$ -axis. Then, the equation of motion of a spin, including the effects of both  $\mathbf{B}_1(t)$  and the static field  $\mathbf{B}_0 = k B_0$ , is given by:

$$\frac{d\langle \hat{\boldsymbol{\mu}} \rangle}{dt} = \gamma \langle \hat{\boldsymbol{\mu}} \rangle \times (\mathbf{B}_0 + \mathbf{B}_1(t)). \quad (3.36)$$

The time dependence of  $\mathbf{B}_1$  can be eliminated by using the rotating frame that rotates about the  $z$ -direction at frequency  $\omega_1$ . In such a frame,  $\mathbf{B}_1$  becomes static. Since the axis of rotation coincides with the direction of  $\mathbf{B}_0$ ,  $\mathbf{B}_0$  is also static. Then, Eq. (3.36) becomes:

$$\frac{d\langle \hat{\boldsymbol{\mu}} \rangle}{dt} = \gamma \langle \hat{\boldsymbol{\mu}} \rangle \times \mathbf{B}_{\text{eff}}, \quad (3.37)$$

where  $\mathbf{B}_{\text{eff}} = k \left( B_0 - \frac{\omega_1}{\gamma} \right) + \mathbf{i} B_1$ . This equation indicates that the magnetic moment in an alternating field obeys the classical equation of motion in Eq. (3.20). Physically, this equation states that in the rotating frame, the moment acts as though it effectively experiences a static magnetic field  $\mathbf{B}_{\text{eff}}$ . The moment, therefore, precesses in a cone of fixed angle about the direction of  $\mathbf{B}_{\text{eff}}$  at an angular frequency of  $\gamma B_{\text{eff}}$ .

### Density Matrix

Since a spin ensemble contains a large number of spins, the formalism of the spin density matrix operator is used to calculate a macroscopic quantity, such as magnetisation.

Consider a sample of many non-interacting spins-1/2. There will be a wave function for each spin-1/2, but in general, it will not be in one of the Zeeman eigenstates ( $|r\rangle = \left|\frac{1}{2}, +\frac{1}{2}\right\rangle$  or  $|s\rangle = \left|\frac{1}{2}, -\frac{1}{2}\right\rangle$ ); rather, it will be in some linear combination of these two eigenstates, i.e. a superposition state,  $|\psi\rangle = \begin{pmatrix} c_r \\ c_s \end{pmatrix}$ . For a given spin, there will be a particular set of values for  $c_r$  and  $c_s$  (Eq. (3.25)); these values will differ from spin to spin. According to Eq. (3.26), the expectation value of an operator  $\hat{Q}$  is given by  $\langle\hat{Q}\rangle = \langle\psi|\hat{Q}|\psi\rangle = \text{Tr}\{|\psi\rangle\langle\psi|\hat{Q}\}$ . For an ensemble containing  $N$  non-interacting spins, the macroscopic observation of  $\hat{Q}$  for the entire ensemble of spins is most likely  $\langle\hat{Q}_{\text{macro}}\rangle = \text{Tr}\{\sum_{i=1}^N |\psi_i\rangle\langle\psi_i| \hat{Q}\} = N\text{Tr}\{\hat{\rho}\hat{Q}\}$ , where  $\psi_i$  is the quantum state of the  $i^{\text{th}}$  spin. The operator,  $\hat{\rho} = \frac{1}{N}\sum_{i=1}^N |\psi_i\rangle\langle\psi_i| = \overline{|\psi\rangle\langle\psi|}$ , is known as the spin density operator. The operator  $\hat{\rho}$  describes the quantum state of the entire spin ensemble without referring to the individual spin states. This indicates that any macroscopic observation may be deduced from two spin operators: the observable itself,  $\hat{Q}$ , and the state of the entire spin ensemble,  $\hat{\rho}$ . The matrix representation of the density operator for an ensemble of non-interacting spins-1/2 is given by:

$$\hat{\rho} = \begin{pmatrix} \rho_{|r\rangle} & \overline{\rho_{rsq_{rs}}} \\ \overline{\rho_{srq_{sr}}} & \rho_{|s\rangle} \end{pmatrix} = \begin{pmatrix} \overline{c_r c_r^*} & \overline{c_r c_s^*} \\ \overline{c_s c_r^*} & \overline{c_s c_s^*} \end{pmatrix}. \quad (3.38)$$

Here, the overbars indicate an average over the ensemble. The right-hand-side in this equation is the spin density matrix operator, often referred to as the “density matrix”.

The diagonal elements,  $\rho_{|r\rangle}$  and  $\rho_{|s\rangle}$  are called the populations of state  $|r\rangle$  and state  $|s\rangle$  (i.e.  $\rho_{|r\rangle} = \langle r|\hat{\rho}|r\rangle$ ), giving the probabilities of occupation of the various eigenstates. The difference in populations between the two states indicates net longitudinal spin polarisation. For example, a state with  $\rho_{|r\rangle} > \rho_{|s\rangle}$  indicates there is a net polarisation of the spins in the sample along the external field direction. In the case of thermal equilibrium of spin-1/2 system (Figure 3.2), both  $\rho_{rsq_{rs}}^{\text{eq}}$  and  $\rho_{srq_{sr}}^{\text{eq}}$  are zeros, whereas  $\rho_{|r\rangle}^{\text{eq}}$  and  $\rho_{|s\rangle}^{\text{eq}}$  obey the Boltzmann distribution:

### 3.5 Spin-3/2 Dynamics

$\rho^{\text{eq}}_{|r\rangle} = 1/(1 + \exp(\gamma B_0 \hbar/kT))$  and  $\rho^{\text{eq}}_{|s\rangle} = 1/(1 + \exp(-\gamma B_0 \hbar/kT))$ , where  $k$  is the Boltzmann constant.

The off-diagonal elements,  $\rho_{\boxed{p_{rs}q_{rs}}}$  and  $\rho_{\boxed{p_{sr}q_{sr}}}$ , are called coherences between the two eigenstates, e.g.  $\rho_{\boxed{p_{rs}q_{rs}}} = \langle r|\hat{\rho}|s\rangle$ . The subscript  $p_{rs}$  denotes the coherence order, which is equal to the difference in the azimuthal quantum number  $m$  for the connected states, i.e.  $p_{rs} = m_r - m_s$ . The sub-subscript  $q_{rs}$  is called the satellite order and is equal to the difference in the squares of the azimuthal quantum numbers  $m$  for the connected states, i.e.  $q_{rs} = m_r^2 - m_s^2$ . The presence of coherences indicates transverse spin magnetisation, i.e. a net spin polarisation perpendicular to the external magnetic field. Immediately after  $90^\circ$ -pulse excitation (Figure 3.3), the spin density operator has the form:  $\rho_{|r\rangle} = \rho_{|s\rangle} = \frac{1}{2}$  and  $\rho_{\boxed{p_{rs}q_{rs}}} = \rho_{\boxed{p_{sr}q_{sr}}}^* \neq 0$ .

The temporal evolution of  $\hat{\rho}$  is governed by the Liouville von Neumann equation:

$$\frac{d}{dt}\hat{\rho}(t) = -\frac{i}{\hbar}[\hat{H}, \hat{\rho}]. \quad (3.39)$$

This equation relates the time derivative of the density operator to the Hamiltonian of the system. It can be used to characterise the spin relaxation dynamics.

### 3.5 Spin-3/2 Dynamics

Spin-3/2 dynamics cannot be described using classical physics because the classical understanding of transverse magnetisation as a vector cannot account for the occurrence of biexponential decay in an uncoupled spin-3/2 ensemble. Hence, a more elaborate quantum mechanical treatment is required for spin-3/2 dynamics.

#### 3.5.1 Spin-3/2 Energy Levels

In the case of spin-3/2, there are four eigenstates of angular momentum along the  $z$ -axis, denoted  $|\frac{3}{2}, m\rangle$ , where the azimuthal quantum number,  $m$ , is equal to  $\{+\frac{3}{2}, +\frac{1}{2}, -\frac{3}{2}, -\frac{1}{2}\}$ . The eigenvalues of the Hamiltonian  $\hat{H}$  of the spin system in the static magnetic field  $\mathbf{B}_0$  are the allowed energies,  $E_m = -\gamma \hbar m B_0$ , as shown in Figure 3.6.

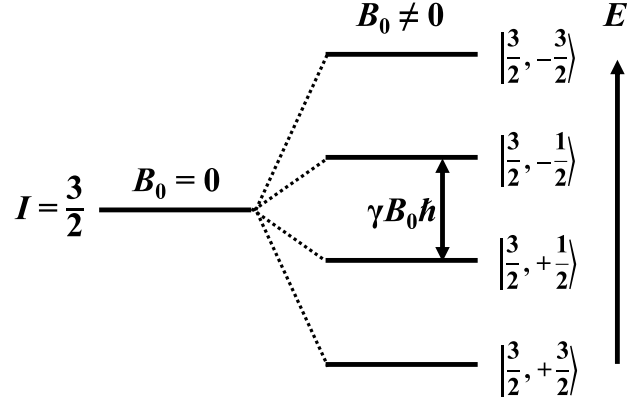


**Figure 3.6** Energy levels of a spin-3/2 nucleus in a homogeneous static magnetic field  $B_0$ , in the case of a positive gyromagnetic ratio.

Similar to Pauli spin-1/2 matrices (Eq. (3.23)), the three components of a spin-3/2 angular momentum operator  $\hat{\mathbf{I}}$  in the Zeeman eigenbasis:  $\hat{I}_x$ ,  $\hat{I}_y$  and  $\hat{I}_z$ , can be expressed with higher dimensional matrices, as follows:

$$\begin{aligned}\hat{I}_x &= \frac{1}{2} \begin{pmatrix} 0 & \sqrt{3} & 0 & 0 \\ \sqrt{3} & 0 & 2 & 0 \\ 0 & 2 & 0 & \sqrt{3} \\ 0 & 0 & \sqrt{3} & 0 \end{pmatrix}, \\ \hat{I}_y &= \frac{1}{2i} \begin{pmatrix} 0 & \sqrt{3} & 0 & 0 \\ -\sqrt{3} & 0 & 2 & 0 \\ 0 & -2 & 0 & \sqrt{3} \\ 0 & 0 & -\sqrt{3} & 0 \end{pmatrix}, \\ \hat{I}_z &= \frac{1}{2} \begin{pmatrix} +3 & 0 & 0 & 0 \\ 0 & +1 & 0 & 0 \\ 0 & 0 & -1 & 0 \\ 0 & 0 & 0 & -3 \end{pmatrix}.\end{aligned}\tag{3.40}$$

### 3.5.2 Spin-3/2 Density Matrix

The quantum state of a spin-3/2 ensemble may be written as a time-dependent 4×4 density matrix, as follows:

$$\hat{\rho}(t) = \overline{|\psi(t)\rangle\langle\psi(t)|} = \begin{pmatrix} \rho_{|+3/2\rangle} & \rho_{\boxed{+1+2}} & \rho_{\boxed{+2+2}} & \rho_{\boxed{+3_0}} \\ \rho_{\boxed{-1-2}} & \rho_{|+1/2\rangle} & \rho_{\boxed{+1_0}} & \rho_{\boxed{+2-2}} \\ \rho_{\boxed{-2-2}} & \rho_{\boxed{-1_0}} & \rho_{|-1/2\rangle} & \rho_{\boxed{+1-2}} \\ \rho_{\boxed{-3_0}} & \rho_{\boxed{-2+2}} & \rho_{\boxed{-1+2}} & \rho_{|-3/2\rangle} \end{pmatrix}.\tag{3.41}$$

The populations of the four Zeeman states are denoted  $\{\rho_{|+3/2\rangle}, \rho_{|+1/2\rangle}, \rho_{|-1/2\rangle}, \rho_{|-3/2\rangle}\}$ . The 12 coherences of the spin-3/2 ensemble are labelled using the coherence order and satellite order,

### 3.5 Spin-3/2 Dynamics

as defined in Section 3.4.2. For example, the coherence  $\rho_{\boxed{+1+2}}$  is given by the density matrix element:  $\rho_{\boxed{+1+2}} = \langle 3/2, +3/2 | \hat{\rho} | 3/2, +1/2 \rangle$ , where  $p = \left(\frac{3}{2}\right) - \left(\frac{1}{2}\right) = +1$  and  $q = \left(\frac{3}{2}\right)^2 - \left(\frac{1}{2}\right)^2 = +2$ . Other order labels in Eq. (3.41) can be derived similarly.

As shown in Figure 3.7, the spin-3/2 ensemble supports six single-quantum (SQ) coherences with order  $p = \pm 1$ ,  $\{\rho_{\boxed{-1-2}}, \rho_{\boxed{-10}}, \rho_{\boxed{-1+2}}, \rho_{\boxed{+1-2}}, \rho_{\boxed{+10}}, \rho_{\boxed{+1+2}}\}$ , four double quantum coherences with order  $p = \pm 2$ ,  $\{\rho_{\boxed{-2-2}}, \rho_{\boxed{-2+2}}, \rho_{\boxed{+2-2}}, \rho_{\boxed{+2+2}}\}$ , and a pair for triple-quantum (TQ) coherences with order  $p = \pm 3$ ,  $\{\rho_{\boxed{-30}}, \rho_{\boxed{+30}}\}$ . The coherences,  $\rho_{\boxed{-10}}$  and  $\rho_{\boxed{+10}}$ , are associated with the central transition of the spin-3/2 system.

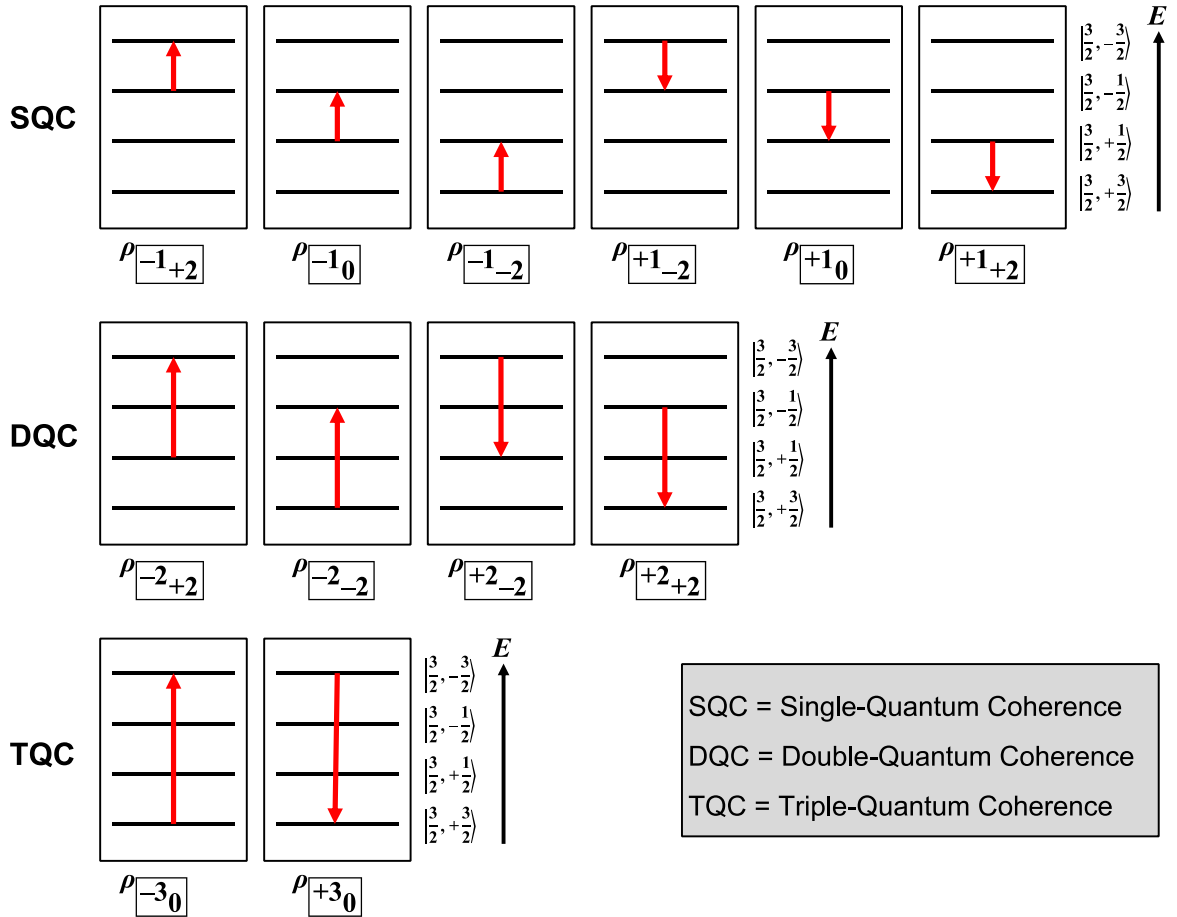


**Figure 3.7** Multiple quantum coherences for a spin-3/2 ensemble. The red arrow indicates that there is a coherence between the two states. For  $\rho_{\boxed{rsqr}}$ , the arrow points from state  $|s\rangle$  to state  $|r\rangle$ .

The coherence order,  $p$ , remains constant during the interaction of the spin-3/2 system with the internal Hamiltonian but can be changed after the application of an RF pulse. The longitudinal



magnetisation has a coherence order of  $p = 0$ . Transverse magnetisation has a coherence order of  $p = \pm 1$ ; and the coherence with  $p = -1$  is the only one that can be directly detected by NMR or MRI instruments (detailed explanation in Session 11.11 of (Levitt 2008)). Coherences with a higher order of  $p = \pm 2$  or  $p = \pm 3$ , are associated with specific tissue properties and are, therefore, of particular interest in clinical practice. Their detection is achieved by using a phase cycling combination (Section 4.3.4).

### 3.5.3 Electric Quadrupolar Interaction

#### *Nuclear Spin Hamiltonian*

As mentioned in Section 3.4.2, the Liouville von Neumann equation involves the motions of all particles in the system of interest, and the Hamiltonian operator contains all interactions between these particles. However, for practical reasons, only the nuclear spin Hamiltonian is considered here, which contains only terms that depend on the orientation of the nuclear spin polarisation. A single atomic nucleus interacts with its environment because (1) it has an electric charge that interacts with electric fields, and (2) it may have a magnetic moment that interacts with magnetic fields. The nuclear spin Hamiltonian operator generally has two terms – an electric spin Hamiltonian and a magnetic spin Hamiltonian:  $\hat{H} = \hat{H}^{\text{elec}} + \hat{H}^{\text{mag}}$ . The magnetic interactions of the spin system with an external static field are described above using the Zeeman Hamiltonian,  $\hat{H}^{\text{static}}$ . In the sample itself, fast-moving electrons in the environment exert averaged magnetic and electrical influences in addition to the influence of external magnetic fields.

#### *Electric Field Gradient*

The rotational motion of nuclei due to the surrounding fields can change the energy of the nucleus, which is of interest in NMR. This is because the nuclear electric charges and magnetic moment adopt a different orientation regarding the surrounding fields.

The electric part of the nuclear spin Hamiltonian is present due to the electric charge distribution in the nucleus. The electric charge distribution is a superposition of electric multipoles, denoted by  $\mathbb{C}(\mathbf{r}) = \mathbb{C}^{(0)}(\mathbf{r}) + \mathbb{C}^{(1)}(\mathbf{r}) + \mathbb{C}^{(2)}(\mathbf{r}) + \dots$ . Here,  $\mathbb{C}^{(0)}$  represents a spherical charge distribution,  $\mathbb{C}^{(1)}$  denotes a dipolar electric charge distribution and  $\mathbb{C}^{(2)}$  signifies a quadrupolar electric charge distribution. The magnitudes of the  $\mathbb{C}^{(0)}$ ,  $\mathbb{C}^{(1)}$  and  $\mathbb{C}^{(2)}$  terms are called the total electric charge of the nucleus, the electric dipole moment of the nucleus and the electric quadrupolar moment of the nucleus, respectively.

The electric potential in a nucleus varies from one side of the nucleus to the other, which influences its rotational motion. The electric potential field is represented as a superposition of terms:  $V(\mathbf{r}) = V^{(0)}(\mathbf{r}) + V^{(1)}(\mathbf{r}) + V^{(2)}(\mathbf{r}) + \dots$ . Here,  $V^{(0)}$  is the electric potential at the centre of the nucleus;  $V^{(1)}$  is the potential gradient at the centre of the nucleus and  $V^{(2)}$  is the gradient of gradient (i.e. the slope) of the potential changes.

The electric interaction energy of the nucleus and the field may be written as  $E_{\text{elec}} = E_{\text{elec}}^{(0)} + E_{\text{elec}}^{(1)} + E_{\text{elec}}^{(2)} + \dots$ . Here, each term comes from the interaction of a single multipole component of the charge distribution with a different aspect of the potential. The first term,  $E_{\text{elec}}^{(0)} = \int \mathbb{C}^{(0)} V^{(0)} d\mathbf{r}$ , represents the electrostatic forces between the nuclei and the electrons; therefore, it is of no direct importance in NMR. The second term,  $E_{\text{elec}}^{(1)} = \int \mathbb{C}^{(1)} V^{(1)} d\mathbf{r}$ , represents the interaction of the nuclear electric dipole moment with the gradient of the electric potential, i.e. the electric field. However, it has been shown that there is no nuclear electric dipole moment within experimental error (Wood et al. 1997). Therefore, the electric terms,  $E_{\text{elec}}^{(1)}, E_{\text{elec}}^{(3)}, E_{\text{elec}}^{(5)}, \dots$ , all disappear. In addition,  $\mathbb{C}^{(n)}$  is zero for  $n > 2I$ , due to a symmetry property that links the shape of the nucleus to the value of the nuclear spin (Chapter 10 of (Slichter 1990)). Hence,  $E_{\text{elec}}^{(n)}$  vanishes for  $n > 2I$ .

Consequently, in the case of spherical spin-1/2 nuclei with a uniform electric charge distribution, all electric multipole moments vanish except  $\mathbb{C}^{(0)}$ . This means that no electric energy terms depend on the orientation or internal structure of the spin-1/2 nucleus. The electric interactions vanish, i.e.  $\hat{H}^{\text{elec}} = 0$  for spin-1/2.

On the other hand, in the case of quadrupolar (i.e. spin  $> 1/2$ ) nuclei (e.g. sodium), the electric charge distribution is not spherically symmetric. The electric energy of the nucleus depends on its orientation relative to the rest of the molecule. The main orientation-dependent electric term,  $E_{\text{elec}}^{(2)} = \int \mathbb{C}^{(2)} V^{(2)} d\mathbf{r}$ , is non-zero, and it represents the interaction of the electric quadrupole moment of the nucleus with the electric field gradient in the surrounding space, as shown in Figure 3.8.

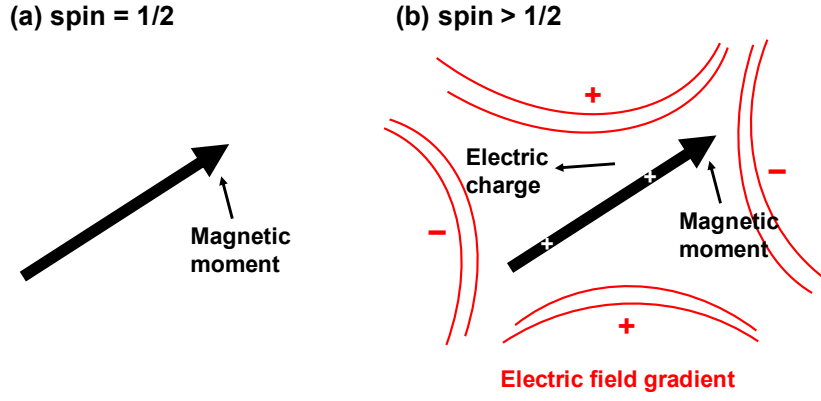


**Figure 3.8** Electric quadrupolar interaction. **(a)** A spherical spin-1/2 nucleus has a uniform electric charge distribution; thus, its electric quadrupolar interactions vanish. **(b)** A spin  $> 1/2$  nucleus has a non-uniform electric charge distribution and thus, it interacts with the surrounding electric field gradient.

### First-order Quadrupolar Coupling

The electric part of the spin Hamiltonian is therefore called the electric quadrupole interaction, i.e.  $\hat{H}^{\text{elec}} = \hat{H}^Q$  for spin  $I > 1/2$ . For spin-3/2,  $\hat{I}$ , the electric quadrupole interaction Hamiltonian for an arbitrary molecular orientation,  $\Theta$ , is given by:

$$\hat{H}_Q^{\text{full}}(\Theta) = \frac{eQ}{2I(2I-1)\hbar} \hat{I} \cdot V(\Theta) \cdot \hat{I}, \quad (3.42)$$

where  $Q$  is the nuclear quadrupole moment;  $I$  is the nuclear spin quantum number;  $e$  is the proton charge; and  $V$  is the electric field gradient. The highest contribution to the quadrupolar interaction Hamiltonian in Eq. (3.42) is given by the first-order term:

$$\hat{H}_Q^{(1)} = \omega_Q^{(1)} \times \frac{1}{6} (3\hat{I}_z^2 - I(I+1)\hat{1}). \quad (3.43)$$

Here,  $\omega_Q^{(1)}$  is the first-order quadrupolar coupling, given by:

$$\omega_Q^{(1)} = \frac{3eQ\bar{V}_{zz}}{2I(2I-1)\hbar}, \quad (3.44)$$

where  $\bar{V}_{zz}$  signifies the average of the secular electric field gradient component,  $V_{zz}(\Theta)$ , over molecular motion.

For spin-3/2 ( $I = 3/2$ ), the first-order quadrupolar Hamiltonian is given by:

$$\hat{H}_Q^{(1)} = \omega_Q^{(1)} \times \frac{1}{6} \left( 3\hat{I}_z^2 - \frac{15}{4}\hat{1} \right). \quad (3.45)$$

The four Zeeman eigenstates of spin-3/2,  $\left| \frac{3}{2}, m \right\rangle$ , are eigenstates of  $\hat{H}_Q^{(1)}$ :

$$\hat{H}_Q^{(1)} \left| \frac{3}{2}, m \right\rangle = +\frac{1}{2} \left( m^2 - \frac{5}{4} \right) \omega_Q^{(1)} \left| \frac{3}{2}, m \right\rangle, \quad (3.46)$$

leading to the following two eigenequations:

$$\begin{cases} \hat{H}_Q^{(1)} \left| \frac{3}{2}, \pm \frac{3}{2} \right\rangle = +\frac{1}{2} \omega_Q^{(1)} \left| \frac{3}{2}, \pm \frac{3}{2} \right\rangle \\ \hat{H}_Q^{(1)} \left| \frac{3}{2}, \pm \frac{1}{2} \right\rangle = -\frac{1}{2} \omega_Q^{(1)} \left| \frac{3}{2}, \pm \frac{1}{2} \right\rangle \end{cases} \quad (3.47)$$

If the first-order quadrupolar coupling,  $\omega_Q^{(1)}$ , is positive, then the energies of the outer states,  $\left| \frac{3}{2}, \pm \frac{3}{2} \right\rangle$ , in Figure 3.6 are shifted upwards in energy by  $\omega_Q^{(1)}/2$ ; in contrast, the energies of the inner states,  $\left| \frac{3}{2}, \pm \frac{1}{2} \right\rangle$ , are shifted down in energy by the same amount (Figure 3.9). The quadrupole coupling,  $\omega_Q^{(1)}$ , is usually much smaller than the Larmor frequency.

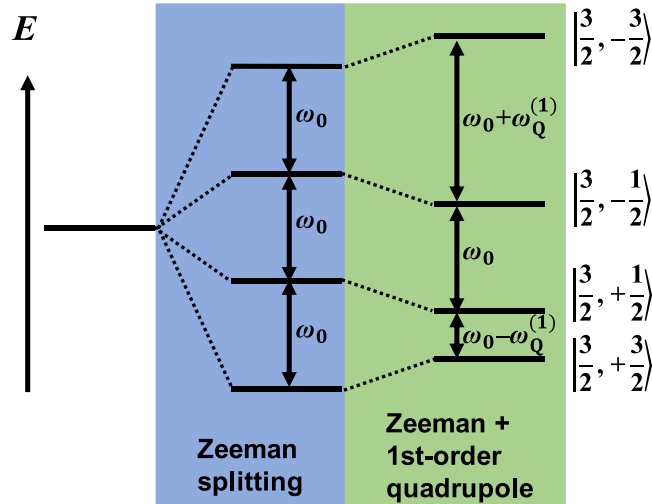


**Figure 3.9** Energy levels of a spin-3/2 nucleus, in the case of a positive gyromagnetic ratio.  $\omega_0$  is the Larmor frequency of the nucleus.  $\omega_Q^{(1)}$  is the first-order quadrupolar coupling.

### *Evolution Frequencies of Coherences*

The evolution frequencies of the spin-3/2 coherences (Figure 3.7) under the influence of the static quadrupolar Hamiltonian (Eq. (3.47)) are given by:

$$\begin{cases} \Omega_{\boxed{-1+2}} = -\Omega_{\boxed{+1-2}} = \Omega^0 - \omega_Q^{(1)} \\ \Omega_{\boxed{-10}} = -\Omega_{\boxed{+10}} = \Omega^0 \\ \Omega_{\boxed{-1-2}} = -\Omega_{\boxed{+1+2}} = \Omega^0 + \omega_Q^{(1)} \\ \Omega_{\boxed{-2+2}} = -\Omega_{\boxed{+2-2}} = 2\Omega^0 - \omega_Q^{(1)} \\ \Omega_{\boxed{-2-2}} = -\Omega_{\boxed{+2+2}} = 2\Omega^0 + \omega_Q^{(1)} \\ \Omega_{\boxed{-30}} = -\Omega_{\boxed{+30}} = 3\Omega^0 \end{cases} \quad (3.48)$$

Here,  $\Omega^0 = -\gamma B_0(\delta - \delta_{\text{ref}})$  is the chemical shift offset frequency, where  $\delta$  is the chemical shift and  $\delta_{\text{ref}}$  is the chemical shift corresponding to the spectrometer reference frequency.

### ***Spin-3/2 NMR Signal***

A complex NMR signal is given by the following expression (more details in Appendix A.5 of the book of (Levitt 2008)):

$$s(t) \sim 2i \langle \hat{I}^+ \rangle \exp\{-i\phi_{\text{rec}}\}. \quad (3.49)$$

where  $\phi_{\text{rec}}$  is the receiver phase and  $\hat{I}^+$  is the raising operator. According to Eq. 3.5.1,  $\hat{I}^+$  of spin-3/2 is given by:

$$\hat{I}^+ \equiv \hat{I}_x + i\hat{I}_y = \begin{pmatrix} 0 & \sqrt{3} & 0 & 0 \\ 0 & 0 & 2 & 0 \\ 0 & 0 & 0 & \sqrt{3} \\ 0 & 0 & 0 & 0 \end{pmatrix}. \quad (3.50)$$

Using  $\langle \hat{I}^+ \rangle = \text{Tr}\{\hat{\rho}\hat{I}^+\}$ , the spin-3/2 NMR signal is given by:

$$s(t) \sim 2i \exp\{-i\phi_{\text{rec}}\} \left( \sqrt{3}\rho_{\boxed{-1-2}}(t) + 2\rho_{\boxed{-10}}(t) + \sqrt{3}\rho_{\boxed{-1+2}}(t) \right). \quad (3.51)$$

Each  $(-1)$ -quantum coherence gives rise to an NMR signal, but the three coherences do not contribute equally. The peak intensity ratio of  $\rho_{\boxed{-1-2}}$ ,  $\rho_{\boxed{-10}}$  and  $\rho_{\boxed{-1+2}}$  is 3:4:3, corresponding to the squares of the  $\hat{I}^+$  matrix elements, which are given by  $\{\sqrt{3}, 2, \sqrt{3}\}$  (Eq. (3.49)). Therefore, the NMR spectrum of a single spin-3/2 ensemble, excited by a strong 90°-RF pulse, is a 3:4:3 triplet, with a splitting of  $\omega_Q^{(1)}$  between adjacent peaks (Eq. (3.48)), as shown in Figure 3.10.

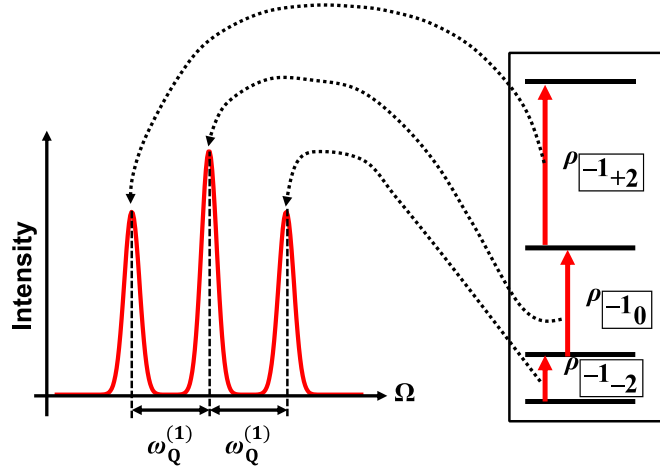


**Figure 3.10** The spectrum of a spin-3/2 ensemble and the corresponding  $(-1)$ -quantum coherences.

The central peak of the spin-3/2 triplet spectrum is of particular importance and is called the central transition. The outer peaks are named satellite transitions.

### 3.5.4 Relaxation Mechanisms of Spin-3/2

In NMR, relaxation was phenomenologically considered by adding additional terms to the spin precession equation. This leads to Bloch's equations (Equations (3.19) and (3.22)) to describe the precession and relaxation of magnetisation in an external magnetic field. However, in the case of spin-3/2 nuclei, the quadrupolar interactions also contribute to the relaxation behaviour.

#### *Irreducible Tensor Operators*

To describe the spin-3/2 dynamics, extensive use of the irreducible tensor operator representation will be made. The advantage of this representation is that it is relatively easy to follow the rank and coherence order of the density operator in a complicated sequence of RF pulses and evolution periods.

Table 3.2 lists the spin-3/2 irreducible tensor operators,  $T_{lm}$ , where  $l$  is the rank and  $m$  is the coherence order. The orthonormal unit tensor operators,  $\hat{T}_{lm}$ , are related to their  $T_{lm}$  counterparts according to  $\hat{T}_{00} = 1/2 T_{00}$ ,  $\hat{T}_{1m} = 1/\sqrt{5} T_{1m}$ ,  $\hat{T}_{2m} = 1/2 \sqrt{2/3} T_{2m}$  and  $\hat{T}_{3m} = 1/3 \sqrt{2} T_{3m}$ . The rank-1 operators are proportional to longitudinal ( $\hat{T}_{10}$  operator) and transverse (symmetric and antisymmetric  $\hat{T}_{11}$  operators) magnetisations.  $\hat{T}_{20}$  represents the quadrupolar spin polarisation. The symmetric and antisymmetric  $\hat{T}_{21}$  ( $\hat{T}_{22}$ ) operators represent rank-2 single- (double-) quantum coherences. The symmetric and antisymmetric  $\hat{T}_{31}$ ,  $\hat{T}_{32}$  and  $\hat{T}_{33}$  operators represent rank-3 single-, double- and triple-quantum coherences, respectively. Therefore, the density matrix can be expanded to 16 basis operators.

**Table 3.2** Irreducible tensor operators for spin-3/2.

$T_{00} = 1$	$T_{20} = 1/\sqrt{6} (3I_z^2 - I(I+1))$	$T_{30} = 1/\sqrt{10} (5I_z^3 - (3I(I+1)-1)I_z)$
$T_{10} = I_z$	$T_{2\pm 1} = \mp 1/2 [I_z, I_{\pm}]_{+}$	$T_{3\pm 1} = \mp 1/4 \sqrt{3/10} [5I_z^3 - I(I+1) - 1/2, I_{\pm}]_{+}$
$T_{1\pm 1} = \mp 1/\sqrt{2} I_{\pm}$	$T_{2\pm 2} = 1/2 I_{\pm}^2$	$T_{3\pm 2} = 1/2 \sqrt{3/4} [I_z, I_{\pm}^2]_{+}$
		$T_{3\pm 3} = \mp 1/2 \sqrt{1/2} I_{\pm}^3$

### Time Evolution of Spin-3/2 System

The spin-3/2 system evolves under the action of the Zeeman, RF, static and fluctuating quadrupolar Hamiltonians (Van Der Maarel 2003). The Zeeman Hamiltonian  $H_z = \omega_0 T_{10}$  in the rotating frame vanishes. With the RF field applied exactly on resonance along the  $x$ -axis with field strength  $\omega_1 = -\gamma B_1$ , the corresponding Hamiltonian is time-independent:  $H_1 = \sqrt{5}\omega_1 \hat{T}_{11}(a)$ . The static quadrupolar Hamiltonian originates from the static quadrupolar interaction:  $H_{QS} = \omega_Q \hat{T}_{20}$ , where  $\omega_Q$  denotes the residual quadrupolar interaction parameter. The fluctuating quadrupolar Hamiltonian,  $H_{QF}$ , arises from the zero-average fluctuating component of the quadrupolar interaction (Van Der Maarel 2003):

$$H_{QF}(t) = C_Q \sum_{m=-2}^2 (-1)^m T_{2m} \times \exp(im\omega_0 t) [F_{2-m}(t) - \langle F_{2-m} \rangle]. \quad (3.52)$$

Here,  $C_Q = eQ/\hbar\sqrt{6}$ , where  $Q$  is the quadrupolar moment of the nucleus and other symbols have their usual meaning. The electric field gradient tensor components,  $F_{2m}$ , takes the form  $F_{20} = 1/2 V_{zz}$ ,  $F_{2\pm 1} = 1/\sqrt{6} (V_{xz} \pm iV_{yz})$  and  $F_{2\pm 2} = 1/2\sqrt{6} (V_{xx} - V_{yy} \pm 2iV_{xy})$ ; and  $\langle F_{2m} \rangle$  represents their average values. The electric field gradient components are time-dependent due to molecular motion. The influence of fluctuating quadrupolar interaction can be considered in the Redfield regime, where relaxation is described by second-order perturbation theory. This theory is valid under the condition that changes in the density operator are small on the correlation time  $\tau_c$  of the lattice motions:  $\langle H_{QF}^2 \rangle \tau_c^2 \ll 1$  (Van Der Maarel 2003).

The time evolution of the density operator is governed by the Liouville von Neumann equation. This equation relates the time derivative of the spin density operator to the Hamiltonian of the spin system and a relaxation superoperator,  $f(\hat{\rho})$ :

$$\frac{d}{dt} \hat{\rho}(t) = -\frac{i}{\hbar} [\hat{H}_1 + \hat{H}_{QS}, \hat{\rho}] + f(\hat{\rho}). \quad (3.53)$$

Here,  $f(\hat{\rho}) = -\int_0^\infty \langle [\hat{H}_{\text{QF}}(t), [\exp(-i(\hat{H}_1 + \hat{H}_{\text{QS}})\tau)\hat{H}_{\text{QF}}(t-\tau)\exp(i(\hat{H}_1 + \hat{H}_{\text{QS}})\tau), \hat{\rho}(t)]] \rangle d\tau$ .

The Zeeman Hamiltonian,  $\hat{H}_0 = \omega_0 T_{10}$ , vanishes in Eq. (3.53) due to the use of the Larmor frequency-rotating frame.

### *Thermal Relaxation in an Isotropic Environment*

Suppose only static and fluctuating quadrupolar interactions exist (i.e. in the absence of an RF field); in that case, the static Hamiltonian  $\hat{H}_{\text{QS}}$  commutes with  $\hat{H}_{\text{QF}}(t)$  and accordingly, is seen as vanishing in the relaxation superoperator (Eq. (3.53)). Furthermore, if the electric field gradient is completely averaged to zero by molecular motion on a timescale faster than the inverse Larmor frequency (i.e. in an isotropic environment,  $\langle F_{2m} \rangle = 0$ ),  $\hat{H}_{\text{QS}}$  is equal to zero and the time dependence is given by the relaxation contribution only. In an isotropic environment, with the fluctuating Hamiltonian in Eq. (3.52), the Liouville von Neumann equation in Eq. (3.53) is simplified as:

$$\frac{d}{dt}\hat{\rho}(t) = -\sum_{m=-2}^2 [T_{2m}, [T_{2m}^\dagger, \hat{\rho}]] \times (J_m(m\omega_0) + iK_m(m\omega_0)). \quad (3.54)$$

$J_m(m\omega_0)$  and  $K_m(m\omega_0)$  are the real and imaginary parts of the Fourier transform of the electric field gradient correlation function:

$$J_m(m\omega_0) = (eQ/\hbar)^2 \text{Re} \int_0^\infty \langle [F_{2m}(t) - \langle F_{2m} \rangle] \times [F_{2m}(t-\tau) - \langle F_{2m} \rangle] \rangle \exp(im\omega_0\tau) d\tau, \quad (3.55)$$

$$K_m(m\omega_0) = (eQ/\hbar)^2 \text{Im} \int_0^\infty \langle [F_{2m}(t) - \langle F_{2m} \rangle] \times [F_{2m}(t-\tau) - \langle F_{2m} \rangle] \rangle \exp(im\omega_0\tau) d\tau. \quad (3.56)$$

Due to the symmetry properties of the double commutator in the relaxation superoperator in Eq. (3.54), the coherence order is conserved under relaxation, whereas the rank can change; additionally, the rank-2 coherence can never be created by relaxation or by coherence transfer (Van Der Maarel 2003).

The complete derivation of the relaxation rates  $R_1^{(1)}$  and  $R_2^{(1)}$  can be found in (Mclachlan 1964; Van Der Maarel 2003). They both depend on  $J_m(m\omega_0)$ :  $R_1^{(1)} = J_0 + J_1$  and  $R_2^{(1)} = J_1 + J_2$ . The derivation is based on the line descriptions of each resonance line in the spectrum, with negligible hyperfine interactions. This means that the static quadrupolar interaction has no contribution to the spin dynamics in the case of an isotropic environment. Two transverse relaxation rates arise from the derivation, representing the fast and slow relaxation times in the presence of a zero-average fluctuating Hamiltonian. Based on the Redfield relaxation matrix



(Jaccard et al. 1986), the fast and slow relaxation times are defined as:  $1/T_{2f} \propto R_1^{(1)}$  and  $1/T_{2s} \propto R_2^{(1)}$ .

### ***Thermal Relaxation in an Anisotropic Environment***

So far, the formalism is strictly valid for nuclei in an isotropic environment, where the nuclei experience a zero-average electric field gradient. In many important systems, such as biological tissue and lyotropic liquid crystals, the quadrupolar interaction is not completely averaged by molecular motion (i.e. in an anisotropic environment). Accordingly, to extend the range of applications to this important class of materials, it is necessary to include the static quadrupolar Hamiltonian in the calculation of the time evolution of the density operator.

In the case of an anisotropic environment, the time dependence of the density operator now reads:

$$\frac{d}{dt}\hat{\rho}(t) = -i\omega_Q/\sqrt{6} [T_{20}, \hat{\rho}] - \sum_{m=-2}^2 [T_{2m}, [T_{2m}^\dagger, \hat{\rho}]] \times (J_m(m\omega_0) + iK_m(m\omega_0)). \quad (3.57)$$

Due to the evolution under the static quadrupolar Hamiltonian, the decoupling of the odd and even rank tensor operators is lifted. This phenomenon allows for the creation of rank-2 coherence, providing for a unique experimental method to probe the existence of higher-order coherences.

The complete derivation of the relaxation rates  $R_1^{(1)}$  and  $R_2^{(1)}$  can again be found in (Mclachlan 1964; Van Der Maarel 2003). In the presence of a static quadrupolar interaction,  $R_1^{(1)}$  depends on both  $J_m(m\omega_0)$  and the quadrupolar coupling:  $R_1^{(1)} = J_0 + J_1 + J_2 - (J_2 - \omega_Q^2)^{1/2}$ , whereas  $R_2^{(1)} = J_1 + J_2$ . For  $\omega_Q = 0$ , these expressions reduce to those in the case of an isotropic environment.

## **3.6 Physical Properties of Sodium in Biological Tissues**

The previously described effects of spin-3/2 are of interest primarily for in vivo NMR and MRI using the sodium nucleus. As discussed in Chapter 2, sodium plays a significant role in maintaining the proper cellular physiology in the human body. Systemic hyponatremia or hypernatremia is a life-threatening condition. In addition, local deviations from normal sodium levels also indicate specific pathologies. Thus, spatially resolved detection of sodium levels is

highly desirable. Of significant interest is the intracellular sodium concentration because it is a sensitive biomarker for the cell's health.

Therefore, a mechanism for the suppression of extracellular sodium is highly desirable. Taking advantage of the sensitive interaction of spin-3/2 sodium nuclei with their local environment, various approaches have been proposed to selectively monitor the intracellular sodium ions via sodium MRI. One approach utilised shift reagents to create a resonance frequency offset for the extracellular sodium ions. Hence, it can differentiate intra- and extracellular sodium signals by chemical-shift-selective NMR measurements. However, its clinical application is not readily feasible due to the reagents' high toxicity and inability to cross the blood-brain barrier (Bansal et al. 1992; Naritomi et al. 1987; Winter et al. 1998). Second, given that the intracellular sodium was reported to exhibit shorter relaxation times (Madelin et al. 2014), inversion recovery techniques can suppress the sodium NMR signal for a weighting towards intracellular sodium, although the residual signal from the extracellular compartment remains unclear (Nagel et al. 2011). Another approach performed tissue compartment mapping using a bi-exponential transverse decay model based on the assumption that 60% and 40% of the tissue sodium signal represent short and long transverse components, respectively (Blunck et al. 2018). Nevertheless, whether the ratio of these two components can be constrained to 60:40 requires further investigation.

The approach used in this thesis is based on the multiple-quantum filtering technique, which probes the multiple quantum coherences that evolve primarily in the intracellular space characterised by slow-moving molecular (i.e. restricted) environments (Seshan et al. 1997; Tauskela et al. 1997). However, several experimental studies found that extracellular sodium also contributed to multiple quantum coherences due to the labile macromolecular interactions (Hutchison et al. 1990; Jelicks & Gupta 1989, 1993); thus, (Burstein & Springer 2019) claimed that extracellular and intracellular sodium cannot be discriminated by the spin dynamics due to the similarity of MR properties. Nevertheless, this thesis assumes that multiple quantum coherences originate from restricted (primarily intracellular) environments. A mathematical treatment of the multiple quantum coherence phenomenon is given in Section 3.5.3. The time dependence of the quadrupolar coupling frequency,  $\omega_Q$ , determines the spectrum of the sodium nuclei. As introduced by (Rooney & Springer 1991), four types of SQ spectra, termed *type a*, *b*, *c* and *d*, may arise from different molecular environments. Figure 3.11 depicts the energy level diagrams (top row), representative spectra (middle row) and quadrupolar time

dependence (bottom row) of sodium spin ensembles in these four different molecular environments.

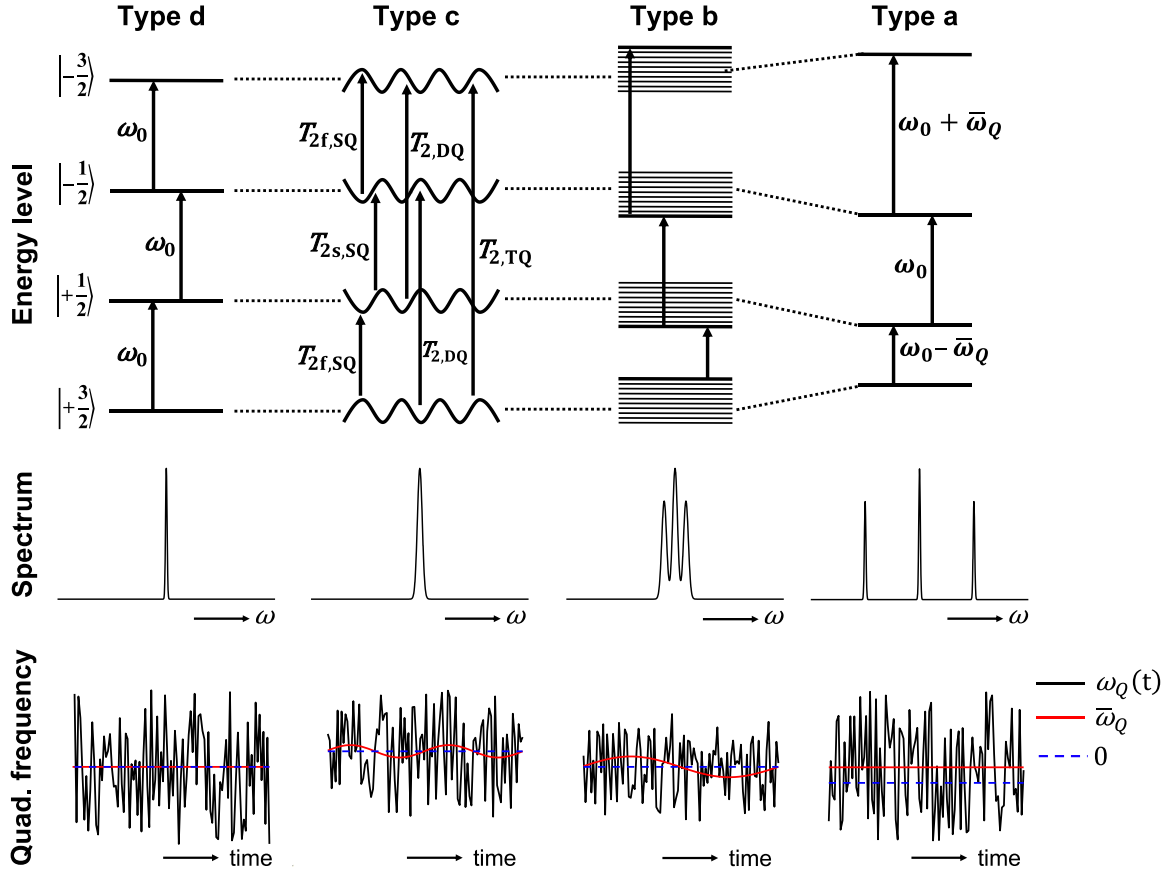


**Figure 3.11** Four types of sodium NMR characteristics in different molecular environments. **Top row:** energy level diagrams. **Middle row:** schematic SQ spectra corresponding to the mean quadrupolar frequency,  $\bar{\omega}_Q$ ; the x-axis represents frequency,  $\omega$ ; the y-axis represents signal intensity. **Bottom row:** scheme of the time dependence of quadrupolar frequency,  $\omega_Q$ , for the four spectral types. The *Type d* spectrum is a narrow Lorentzian line; the *type c* spectrum is a superposition of a narrow and a broad Lorentzian line; the *type b* spectrum consists of a central narrow Lorentzian line with two broad satellite Lorentzian lines; and the *type a* spectrum comprises three separated narrow Lorentzian lines. **Source:** Figure reproduced from (Rooney & Springer 1991) with permission from John Wiley and Sons (License No. 5745351153482).

In the *type d* environment, the quadrupolar fluctuations are so fast that the correlation times are short compared with the Larmor period,  $1/\omega_0$ . In this case, the quadrupolar splitting of the sodium nucleus can be ignored, i.e.  $\omega_Q = 0$ . Consequently, the three SQ coherences yield three isochronous spectral peaks of equally narrow widths; and multiple quantum coherences do not arise. Practically, this case was observed from the sodium cations in a homogeneous aqueous environment, e.g. solutions of up to moderate sodium concentrations (Figure 3.12a). However, this phenomenon usually is not observed in biological tissues.

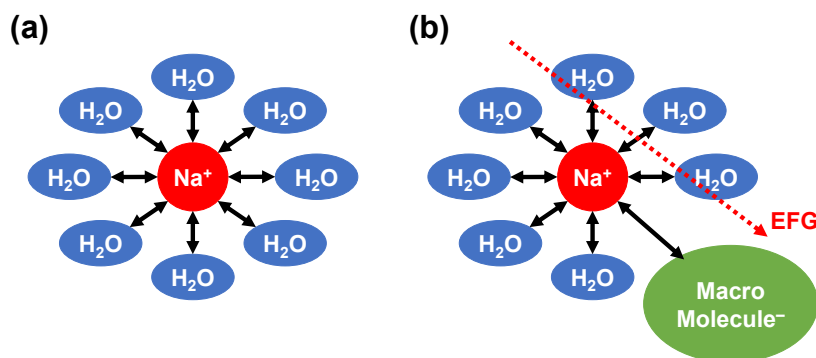


**Figure 3.12** Interaction of a sodium cation with its surrounding environment. **(a)** Homogeneous environment. **(b)** Inhomogeneous environment. The sodium cation interacts with a negatively charged macromolecule (green area) through the electric field gradient (EFG).

In biological tissues, sodium aquocations exist in compartmentalised spaces. However, in both intracellular and extracellular environments, the cation encounters many negatively charged macromolecules, such as polyelectrolytes, in its diffusional excursions (Figure 3.12b). This interaction primarily produces a slower  $\omega_Q$  modulation that is superimposed on the modulation generated by the rapid fluctuations of the hydration shells, as shown in the corresponding time course in Figure 3.11. The non-zero  $\bar{\omega}_Q$  can be observed on a short time scale, but it stays zero for longer period. The resulting SQ spectrum comprises three isochronous homogeneous resonances. The narrow central SQ coherence ( $|1/2\rangle \rightarrow |-1/2\rangle$ ) is superimposed on the broader resonances of the two satellite SQ coherences ( $|3/2\rangle \rightarrow |1/2\rangle$  and  $|-1/2\rangle \rightarrow |-3/2\rangle$ ). In this case, sodium nuclei exhibit biexponential transverse relaxation: the central SQ transition yields a slow  $T_2$  value, whereas the two satellite SQ transitions result in a fast  $T_2$  value.

If the electric field fluctuations become more prominent, such that sodium ions remain in regions with a non-zero  $\bar{\omega}_Q$  for a period longer than the Larmor period, a *type b* spectrum (so-called powder spectrum) is generated. The spectrum comprises the homogeneous central resonance and the two different inhomogeneous “powder” patterns of the satellite resonances.

If the value of  $\bar{\omega}_Q$  is always non-zero, a *type a* spectrum is yielded. It occurs in the case of anisotropic samples on the macroscopic scale, single crystals or oriented liquid crystals. The well-known triplet spectrum with an intensity ratio of 3:4:3 is observed.

In the human body, *type d* spectra are commonly observed in aqueous solutions such as CerebroSpinal Fluid (CSF) and are typical for extracellular sodium. *Type b* and *c* are typical for intracellular sodium. The *type a* spectrum is less likely to occur in biological tissues.

## 4 Magnetic Resonance Imaging

### *From Signal to Image*

This chapter aims to introduce the generation of Magnetic Resonance Imaging images based on the Nuclear Magnetic Resonance signal. First, the MRI scanner structure is briefly introduced. Second, the fundamental concepts and rules of MRI closely relative to the remainder of this thesis are introduced. Furthermore, the principles of k-space sampling are described. Finally, the image reconstruction strategies are explained.

### 4.1 Scanner Structure

The structure of clinical superconductive magnetic resonance scanners is similar to Figure 4.1.

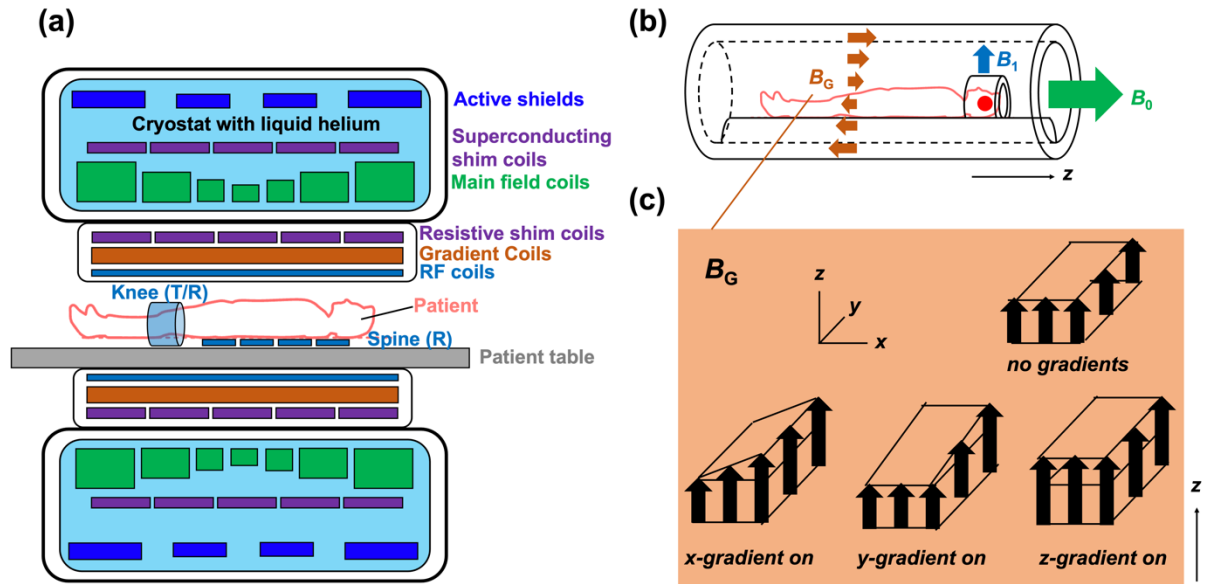


**Figure 4.1** Structure of a superconductive magnetic resonance scanner. **(a)** A representative cross-section of a superconducting scanner. Two types of patient coils: a transmit/receive knee coil and a receive-only spine coil array. **(b)** The scanner has a superconducting coil that generates a static  $B_0$  field, an RF coil that produces a circularly polarised  $B_1$  field in the transverse plane ( $xy$ -plane) and three gradient coils that yield a linear alteration of the  $z$ -component of the magnetic field depending on the  $x$ ,  $y$  and  $z$  positions,  $B_G$ . Red dot: isocentre. **(c)** The action of gradient fields. Note that  $x$ ,  $y$  and  $z$ -gradients only alter the magnetic field along the  $z$ -direction.

The current passing through a superconducting coil within the helium-filled cryostat generates the main static  $B_0$  magnetic field, which creates an initial longitudinal magnetisation in the subject. The  $B_0$  field is created in the scanner bore with the highest field homogeneity around the isocentre (red dot in Figure 4.1b), which is usually a specific point within the anatomical region of interest. Active shielding coils can reduce the static fringe field produced by the main magnet, which are typically located within the cryostat just outside the main field coils.

However,  $B_0$  field inhomogeneities in the scanner bore may occur due to susceptibility effects in the patient or surrounding environment, as well as manufacturing imperfections. Shimming, which can be passive or active, is used to correct the  $B_0$  field. Passive shimming is performed by placing small pieces of ferromagnetic materials (typically iron or steel) in a regular pattern at specific locations along the inner bore of the magnet. Active shimming uses currents directed through specialised shim coils to generate a magnetic field that compensates for the  $B_0$  field inhomogeneities. There are two types of active shim coils: (1) superconducting coils located inside a cryostat containing liquid helium and (2) resistive coils mounted along with the gradient coils inside the room-temperature inner walls of the scanner.

The gradient coils are primarily used for spatial encoding of the NMR signal. They are placed just inside the bore of a scanner and generate a secondary magnetic field. This gradient field slightly alters the main magnetic field along the  $z$ -direction, causing the resonance frequency of target nuclei to vary as a function of position in the scanner. Note that the  $x$ - and  $y$ -gradients do not yield transverse components that rotate  $B_0$  by a certain angle (Figure 4.1c). The rapidly changing gradients can induce eddy currents in metallic parts of the scanner. Actively shielded gradient coils just superficial to the imaging gradients can dynamically eliminate changing magnetic fields and decrease eddy currents produced in the main magnet structure.

The RadioFrequency coils can act as transmitters, receivers or both. When used as a transmitter, the RF coil generates an oscillating  $B_1$  field perpendicular to  $B_0$  field. If the oscillations closely match the intrinsic precession of the nuclear spins around the Larmor frequency, energy is deposited into the spin system, causing a change in its net alignment. The  $B_1$  field is generated by the transmit RF coil in response to the strong current generated by the scanner's transmit circuitry.  $B_1$  is usually turned on for a short time (typically a few msec), called an "RF pulse". By adjusting the magnitude or duration of the RF pulse, the nuclear spin system can be rotated by a variable flip angle, such as  $90^\circ$  or  $180^\circ$ . When used as a receiver, the RF coil detects the NMR signal. The oscillating net magnetic flux from the excited nuclear spin system can be captured by the coil. Consequently, an induced electric current is generated in the RF coil. Then, this current is amplified, digitised and filtered to obtain frequency and phase information.

### 4.2 Imaging Principles

This section presents the fundamental concepts and rules of MRI, which are of particular interest to sodium MRI and are of importance for the second part of this thesis. The explanations mainly follow the book of (Brown et al. 2014).

### 4.2.1 Spatial Encoding: Gradient and K-space

As described in Section 3.3.7, the origin of the NMR signal is a voltage that is induced in the receiver coil,  $V_{\text{ind}}$ , due to a change in the magnetic flux,  $\Phi$ :

$$V_{\text{ind}} = -\frac{d}{dt}\Phi = -\dot{\Phi}. \quad (4.1)$$

The magnetic flux  $\Phi$  varies with time due to the oscillating magnetic moments, i.e. the magnetisation vectors. According to (Brown et al. 2014), the bulk signal measured by the receiver coils is proportional to the transverse magnetisation vector. For imaging, the measured bulk signal of a spin ensemble needs to be disentangled regarding the spatial distribution. On that account, the magnetic field gradient is introduced to spatially encode the received signal using the concept of k-space.

According to the magnetic resonance condition:  $\omega = \omega_0 = -\gamma\mathbf{B}_0$ , if a small, changing magnetic field (i.e. gradient field) is added to the  $\mathbf{B}_0$  field along/against the  $z$ -direction, the uniformity of the  $\mathbf{B}_0$  field is degraded, with different resonance frequencies at different positions along the gradient direction ( $x$ ,  $y$  or  $z$ -direction) (Figure 4.2). For example, the additional magnetic gradient field changing along the  $x$ -direction,  $B_{G_x} = x \cdot G_x$ , provides the resonance frequency,  $\omega_x$ :

$$\omega_x = -\gamma(\mathbf{B}_0 + x \cdot G_x) = \omega_0 + \Delta\omega_x. \quad (4.2)$$

In this way, the spatial displacement,  $x$ , is converted into the resonance frequency shift,  $\Delta\omega_x$ , so as to obtain the spatial information inside the object. This process is known as spatial encoding. The MRI scanner is equipped with three sets of gradient coils to generate gradient fields in the  $x$ ,  $y$  and  $z$  directions (Figure 4.1c). The total gradient is given as  $\mathbf{G} = (G_x, G_y, G_z)$ , and the corresponding total gradient field is given as  $\mathbf{B}_G = \mathbf{G} \cdot \mathbf{r} = (x \cdot G_x, y \cdot G_y, z \cdot G_z)$ , resulting in a resonance frequency shift  $\Delta\omega = -\gamma\mathbf{B}_G$ .  $\mathbf{r} = (x, y, z)$  is the position with respect to the isocentre.

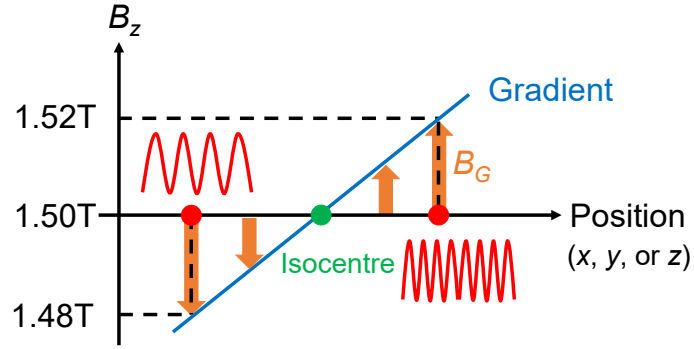


**Figure 4.2** Gradient field and resonance frequency. A small, linearly changing gradient field,  $\mathbf{B}_G$ , is added to the  $\mathbf{B}_0$  field ( $B_0 = 1.5\text{T}$ ) along/against the  $z$ -direction. Different positions along the gradient direction ( $x$ ,  $y$  or  $z$ ) possess different resonance frequencies. The isocentre has a resonance frequency of  $\omega_0 = -\gamma\mathbf{B}_0$ .

In the absence of gradient fields, if the relaxation effect is neglected, the transverse magnetisation after RF pulse excitation is given as:

$$M_{xy}(\mathbf{r}, t) = e^{-i\omega_0 t} \cdot M_{xy}(\mathbf{r}, t = 0). \quad (4.3)$$

The phase of  $M_{xy}$  is  $\omega_0 t$ .

In the presence of additional magnetic gradient fields,  $M_{xy}$  produces an additional phase accumulation,  $\varphi(\mathbf{r}, t)$ :

$$\varphi(\mathbf{r}, t) = \int_0^t \omega_G(\mathbf{r}, \tau) d\tau = \int_0^t \gamma \mathbf{B}_G(\mathbf{r}, \tau) d\tau = \int_0^t \gamma \mathbf{G}(\tau) \cdot \mathbf{r} d\tau = \gamma \cdot \mathbf{r} \cdot \int_0^t \mathbf{G}(\tau) d\tau. \quad (4.4)$$

Here, define  $\mathbf{k}(t)$  as:

$$\mathbf{k}(t) = \frac{\gamma}{2\pi} \int_0^t \mathbf{G}(\tau) d\tau, \quad (4.5)$$

and substitute Eq. (4.5) to Eq. (4.4), the phase term becomes:

$$\varphi(\mathbf{r}, t) = 2\pi \cdot \mathbf{k}(t) \cdot \mathbf{r}. \quad (4.6)$$

Add the phase term to Eq. (4.3),  $M_{xy}$  becomes:

$$M_{xy}(\mathbf{r}, t) = e^{-i\omega_0 t} \cdot e^{-i2\pi \mathbf{k}(t) \cdot \mathbf{r}} \cdot M_{xy}(\mathbf{r}, t = 0). \quad (4.7)$$

The signal measured by the receiver coils,  $U(t)$ , is determined by the transverse magnetisation of every excited spin. Therefore,  $U(t)$  is proportional to all transverse magnetisations within the sample:



$$\begin{aligned}
 U(t) &= c \cdot \int M_{xy}(\mathbf{r}, t) d\mathbf{r} = c \cdot \int e^{-i\omega_0 t} \cdot e^{-i2\pi \mathbf{k}(t) \cdot \mathbf{r}} \cdot M_{xy}(\mathbf{r}, t=0) d\mathbf{r} \\
 &= \hat{c} \cdot e^{-i\omega_0 t} \cdot \int e^{-i2\pi \mathbf{k}(t) \cdot \mathbf{r}} \cdot \rho(\mathbf{r}) d\mathbf{r}.
 \end{aligned} \tag{4.8}$$

According to Eq. (3.12), the spin density  $\rho(\mathbf{r})$  is proportional to  $M_{xy}(\mathbf{r}, t=0)$ , so the scaling constant,  $c$ , is updated as  $\hat{c}$  with respect to  $\rho(\mathbf{r})$ . After signal demodulation, the  $e^{-i\omega_0 t}$  term in Eq. (4.8) is removed. The signal,  $S(t)$ , is seen in a rotating frame:

$$S(t) = e^{i\omega_0 t} \cdot U(t) = \hat{c} \cdot \int e^{-i2\pi \mathbf{k}(t) \cdot \mathbf{r}} \cdot \rho(\mathbf{r}) d\mathbf{r}. \tag{4.9}$$

Substitute  $t$  with  $\mathbf{k}$  in Eq. (4.9), the received signal is proportional to the Fourier transform of the spin density,  $\rho(\mathbf{r})$ :

$$S(\mathbf{k}) = \hat{c} \cdot \int e^{-i2\pi \mathbf{k} \cdot \mathbf{r}} \cdot \rho(\mathbf{r}) d\mathbf{r} = \hat{c} \cdot \text{FT}[\rho(\mathbf{r})]. \tag{4.10}$$

This Fourier space is called k-space and is denoted as  $\mathbf{k}$  (Eq. (4.5)). The spatial information collected at time  $t$  is placed at the corresponding  $\mathbf{k}(t)$  in the k-space. In practice, the received signal is affected by relaxation. For an accurate representation of  $S(t)$ , a relaxation term should be included in Eq. (4.10). For most samples,  $T_1$  and  $T_2$  relaxation times are spatially correlated. Therefore, the relaxation term should be placed within the integral of Eq. (4.10).

#### 4.2.2 Excitation in Presence and Absence of Gradients

Gradients are primarily used to traverse k-space after signal induction through an RF pulse. However, the spatial encoding capacities of gradients are also of interest during the RF excitation process.

In the presence of gradients, the spin density in Eq. (4.10) is weighted by the spectral profile of the RF pulse,  $P(\omega)$ . This factor is obtained by the Fourier transform of the RF pulse in time domain,  $P(t)$ . In this case, Eq. (4.10) becomes:

$$S(\mathbf{k}) = \hat{c} \cdot \text{FT}[\rho(\mathbf{r}) \cdot P(\omega)]. \tag{4.11}$$

Since  $\omega = \gamma \mathbf{G} \cdot \mathbf{r}$ , Eq. (4.11) further becomes:

$$S(\mathbf{k}) = \hat{c} \cdot \text{FT}[\rho(\mathbf{r}) \cdot P(\mathbf{r})]. \tag{4.12}$$

It should be noted that  $P$  can also depend on  $\mathbf{k}$  in the case of varying gradients during RF excitation.

According to Eq. (4.12), the RF pulse acts as a filter in the range of spin precession frequencies resulting from the applied gradient. This mechanism provides a useful tool for spatial selectivity. MRI scanners offer a variety of spatially selective effects on RF excitation, which can be broadly grouped into two categories: non-slice-selective excitation in the absence of gradients and slice-selective excitation in the presence of gradients.

In the absence of gradients, excitations with a rectangular hard pulse are non-slice-selective. The hard pulse has a shorter time course compared to the abovementioned sinc pulse, and the corresponding spectral profile is sinc-shaped. For a fast-sampling onset, the acquisition of fast decaying NMR signals (e.g. sodium signals) is commonly based on the more efficient hard pulse with a non-slice-selective excitation. In the presence of gradients, two steps are required to uniquely excite a slice in Two-Dimensional (2D) MRI, as discussed in Appendix A1.

### 4.2.3 Gradient Echoes and $T_2^*$

As indicated in Eq. (4.4), gradients lead to a spatially dependent phase accumulation across the entire excited spin ensemble, i.e. increasing  $k$ , as described in Eq. (4.5). Consequently, the application of gradients results in a reduction in the net NMR signal by dephasing. This signal loss can be recovered by applying a counteracting gradient, i.e. a gradient of opposite polarity that refocuses the introduced field inhomogeneity. For such a signal refocusing, these two gradients,  $\mathbf{G}$  and  $\mathbf{G}_{\text{ref}}$ , should fulfil:

$$\varphi_G - \varphi_{G_{\text{ref}}} = \gamma \cdot \mathbf{r} \cdot \int_{t_0}^{t_1} \mathbf{G}(\tau) d\tau - \gamma \cdot \mathbf{r} \cdot \int_{t_1}^{t_2} \mathbf{G}_{\text{ref}}(\tau) d\tau = 0, \quad (4.13)$$

i.e. the cumulative phase produced by the first gradient should be cancelled out by the following refocusing gradient. At time  $t_2$ , the signal is completely refocused, and a so-called gradient echo is generated. The time interval from time  $t_0$  to time  $t_2$  is called the Echo Time (TE).

It should be noted that only gradient-induced inhomogeneities are reverted. Inherent dephasing through other mechanisms, e.g. microscopic magnetic field fluctuation (Section 3.3.6) or quadrupole interactions (Section 3.5.3), are irreversible. Therefore, the echo underlies signal loss through  $T_2$  transverse relaxation. In the presence of additional external macroscopic inhomogeneities, such as  $B_0$  field inhomogeneity, the signal decay should consider another relaxation time constant, commonly termed  $T_2'$ . Hence, the total echo signal generated by the refocusing gradient is governed by two decay processes, resulting in a relaxation time constant,  $T_2^*$ :

$$\frac{1}{T_2^*} = \frac{1}{T_2} + \frac{1}{T_2'}, \quad (4.14)$$

where  $\frac{1}{T_2'} = \gamma\Delta B$ , with  $\Delta B$  denoting the local macroscopic field inhomogeneity.

In addition to gradients, the phase dispersion of spins can be unravelled through a refocusing RF pulse (typically a  $180^\circ$ -pulse). The refocusing pulse flips all spins by  $180^\circ$ ; thus, the phase is inverted. Every spin ends up experiencing effects from the opposite macroscopic field inhomogeneity spectrum. This pulse-based refocusing of the dephasing signal is known as spin echo. Its primary advantage over gradient echo is that the spin-flipping also cancels dephasing effects induced by the macroscopic field inhomogeneities, i.e. it allows a direct measure of  $T_2$  signal decay (Figure 4.3). However, the application of a refocusing pulse has two disadvantages listed below.

1. The additional RF power disposition accelerates the violation of the Specific Absorption Rate limit, necessitating longer acquisition times, especially at ultra-high field strengths ( $\geq 7\text{T}$ ).
2. Since detecting signal during RF excitation is impossible, the additional time spent on applying the refocusing pulse results in a longer TE, greatly reducing the information content that can be sampled. This is especially detrimental to the detection of rapidly decaying sodium signals.

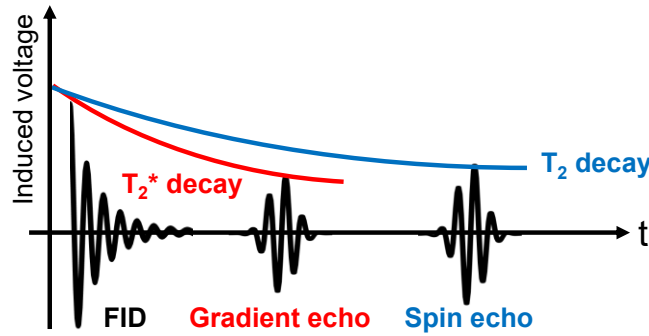


**Figure 4.3**  $T_2^*$  and  $T_2$  decay. The gradient echo results in a  $T_2^*$  decay, whereas the spin echo yields a  $T_2$  decay.

#### 4.2.4 Data Acquisition Principle: Nyquist Sampling Criterion

The Fourier transform serves as a continuous linear mapping between the time and frequency domains. In practice, the acquired signal is neither continuously sampled nor measured for infinite time. The discrete sampling and truncated data acquisition do not preclude the use of the Fourier relationship between the acquired NMR signal and the reconstructed spin density

image. Nevertheless, the data sampling process must obey a certain criterion for artefact-free reconstruction – the Nyquist sampling criterion. This criterion acts as a fundamental bridge between continuous- and discrete-time signals. It sets up a sufficient condition for a sampling rate that allows a discrete sequence of samples to capture all information from a bandwidth-limited continuous-time signal.

### *Infinite Discrete Sampling*

The continuously induced signal in the receiver coil is digitised via an Analog-to-Digital Converter (ADC). This process corresponds to a discrete sampling of k-space. According to Eq. (4.5), the finite sampling interval,  $\Delta t$ , links to the sample spacing in k-space,  $\Delta k$ :

$$\Delta k = \frac{\gamma}{2\pi} \int_0^{\Delta t} G(\tau) d\tau. \quad (4.15)$$

The NMR signal is generally collected over a set of uniformly spaced points in k-space. For a constant readout gradient,  $G_{RO}$ , such sampling is achieved along the readout direction with the k-space spacing,  $\Delta k = \frac{\gamma}{2\pi} G_{RO} \Delta t$ . Denoting each integer sampling step,  $p$ , the infinite data sampling can be described via a “Dirac comb” function,  $iii(k)$ :

$$iii(k) \equiv \Delta k \sum_{p=-\infty}^{\infty} \delta(k - p\Delta k), \quad (4.16)$$

where  $\delta$  corresponds to the Dirac delta function. The discretised signal,  $S_d(k)$ , is given by the multiplication of the continuous-time signal,  $S(k)$ , and the “Dirac comb” function,  $iii(k)$ :

$$S_d(k) = S(k) \cdot iii(k) = \Delta k \sum_{p=-\infty}^{\infty} S(p\Delta k) \delta(k - p\Delta k). \quad (4.17)$$

The inverse Fourier transform of an infinitely sampled NMR signal,  $S_d(k)$ , leads to a reconstructed image,  $\rho_d(r)$ , of the spin density in the object,  $\rho(r)$ :

$$\begin{aligned} \rho_d(r) &= \int_{-\infty}^{\infty} dk S_d(k) e^{i2\pi kr} = \int_{-\infty}^{\infty} dk \left[ \Delta k \sum_{p=-\infty}^{\infty} S(p\Delta k) \delta(k - p\Delta k) \right] e^{i2\pi kr} \\ &= \Delta k \sum_{p=-\infty}^{\infty} S(p\Delta k) e^{i2\pi p\Delta kr}. \end{aligned} \quad (4.18)$$

This expression is an infinite Fourier series, representing a histogram approximation of the continuous inverse transform of the physical spin density,  $\rho(r)$ . If  $\rho(r)$  vanishes outside a finite

interval, the periodic Fourier series produces an infinite set of exact copies of the physical spin density, provided that the period associated with the copies is larger than the interval. A period that is too small gives rise to an “aliasing” problem, which will be discussed in the next section.

$\rho_d(r)$  can be described equivalently by the convolution of  $\rho(r)$  and the inverse Fourier transform of  $III(k)$  in the time domain,  $III(r)$ :

$$\rho_d(r) = \rho(r) * III(r), \quad (4.19)$$

where  $*$  represents the convolution operator and  $III(r)$  is also a “Dirac comb” function:

$$III(r) = \sum_{q=-\infty}^{\infty} \delta(r - q/\Delta k), \quad (4.20)$$

with  $q$  indicating sampling steps.

The convolution of any function  $f(x)$  with a delta function  $\delta(x - x_0)$  is easily seen to be:

$$f(x) * \delta(x - x_0) = \int dx' f(x') \delta(x' - x_0) = f(x - x_0). \quad (4.21)$$

According to Eq. (4.21), the convolution of the infinite sum (Eq. (4.20)) with any function gives an infinite series, in which each term is a copy of the function shifted by the interval  $1/\Delta k$  from the next term. That is, Eq. (4.19) becomes:

$$\rho_d(r) = \sum_{q=-\infty}^{\infty} \rho(r) * \delta(r - q/\Delta k) = \sum_{q=-\infty}^{\infty} \rho(r - q/\Delta k). \quad (4.22)$$

### ***Nyquist Sampling Criterion***

It is observed from Eq. (4.18) that the periodicity corresponds to the fact that  $e^{i2\pi p \Delta k r}$  is unchanged for any  $p$ , if  $r \rightarrow r + 1/\Delta k$ . This replication concept is evident from Eq. (4.22) and demonstrates that  $\rho_d(r)$  is translationally invariant. This is:

$$\rho_d(r) = \rho_d(r + 1/\Delta k). \quad (4.23)$$

Therefore, the periodicity of  $\rho_d(r)$  is given by the reciprocal of the spacing of the delta functions in the Fourier transform of the sampling function,

$$1/\Delta k \equiv L \equiv \text{FOV}. \quad (4.24)$$

The uniform spacing,  $\Delta k$ , between k-space data points is  $1/L$ , where  $L$  is the spatial interval over which the reconstructed image repeats itself. The spatial interval  $L$  is named the Field Of View (FOV).

To construct an image, one of these copies is chosen. If the copies overlap, there will be a significant difference between  $\rho(r)$  and what is displayed as an image. This type of artefact is generally referred to as aliasing. A general requirement, or criterion, can be found for the sampling rate to remove this artefact.

The criterion can be introduced by considering what happens if  $L$  is too small. If the spatial period,  $L$ , of the replica is greater than the length of the object being imaged,  $A$ , there is no aliasing artefact in the reconstructed image. However, if  $L < A$ , then those parts of the image corresponding to the pixels near the edges of the object (which must be assigned somewhere in the image) will be mapped back inside  $L$ . The object is aliased due to the overlap of the copies, with the left edge mapped into the right side of the interval,  $L$ , and vice versa for the right edge. To avoid this type of image error, data must be sampled such that the inverse of the sampling step in k-space,  $1/\Delta k$ , is larger than the size of the object to be imaged,  $A$ . This means that the FOV must be larger than the object size:

$$L > A \quad \text{or} \quad \Delta k < 1/A. \quad (4.25)$$

Eq. (4.25) is referred to as the Nyquist sampling criterion.

### ***Truncated Signal Acquisition***

The measurement of the image space ( $r$ ) itself is discretised and truncated. The reason for the truncation is that no new information can be gained from other copies of the image. The discretisation is performed over spatial steps with a uniform step size,  $\Delta r$ , since there is a lower limit to the spatial information, or resolution, available in the reconstructed spin density. A root cause of the lower limit is the blurring artefacts in the image space that arise from the truncation of the k-space data.

The data truncation, or windowing, is modelled mathematically by multiplying the sampled data by a rectangular function,  $\text{rect}\left(\frac{k + \frac{1}{2}\Delta k}{W}\right)$  (details in Chapter 9 of (Brown et al. 2014)). After data truncation, the “Dirac comb” function in Eq. (4.16) becomes:

$$iii(k) \cdot \text{rect}\left(\frac{k + \frac{1}{2}\Delta k}{W}\right) = \Delta k \sum_{p=-n}^{n-1} \delta(k - p\Delta k), \quad (4.26)$$

where the total number of points is  $N = 2n$  and  $W \equiv 2n\Delta k = N\Delta k$ . An integration over Eq. (4.26) yields  $\Delta k$  for each sampled k-space point. Thus,  $2n\Delta k$  is the total interval covered in k-space, containing  $2n$  total points.

The final expression for the signal distribution corresponding to truncated signal acquisition, or measured signal distribution,  $S_m(k)$ , is the product of three functions (infinite signal, sampling and window) given by:

$$S_m(k) = S(k) \cdot iii(k) \cdot \text{rect}\left(\frac{k + \frac{1}{2}\Delta k}{W}\right) = \Delta k \sum_{p=-n}^{n-1} S(p\Delta k) \delta(k - p\Delta k). \quad (4.27)$$

The result is the expected discrete and finite sum of delta function terms whose coefficients are again the sampled k-space signal,  $S(p\Delta k)$ .

The reconstructed spin density resulting from truncated acquisition is called  $\hat{\rho}_d(r)$ , and it is defined by the inverse Fourier transform of  $S_m(k)$ :

$$\hat{\rho}_d(r) \equiv \int_{-\infty}^{\infty} dk S_m(k) e^{i2\pi kr} = \Delta k \sum_{p=-n}^{n-1} S(p\Delta k) e^{i2\pi p\Delta kr}. \quad (4.28)$$

The periodicity in Eq. (4.23) survives in Eq. (4.28):  $\hat{\rho}_d(r) = \hat{\rho}_d(r + 1/\Delta k)$ . Therefore, the Nyquist criterion also applies to the truncated data.  $\hat{\rho}_d(r)$  arose from the finite discrete sampling is an approximation of  $\rho_d(r)$  from the infinite discrete sampling in Eq. (4.18).

The total number of sampling points,  $N = 2n$ , provides the basis for the spatial resolution of the reconstructed image due to:

$$\Delta r = \frac{\text{FOV}}{N} = \frac{1}{N\Delta k} = \frac{1}{2n\Delta k} = \frac{1}{2k_{\max}}, \quad (4.29)$$

with  $n\Delta k = k_{\max}$ . The resolution,  $\Delta r = \frac{\text{FOV}}{N}$ , is thus fixed by  $N$  and FOV, commonly referred to as the *pixel size* or *voxel size* of the image. This concludes that more minor spatial details require more outer k-space sampling.

The finite sampling function in the image domain resembles Eq. (4.16), but with steps  $\Delta r$ , given by:

$$\widehat{M}(r) = \Delta r \sum_{q=-\infty}^{\infty} \delta(r - q\Delta r). \quad (4.30)$$

Consider the number of sampling points equal to  $2n'$  rather than  $2n$  and perform a calculation like that in Eq. (4.27). The measured reconstructed spin density distribution for  $2n'$  sampled points,  $\rho_m(r)$ , counterparts to the measured signal distribution,  $S_m(k)$ , in Eq. (4.27), given by:

$$\rho_m(r) = \rho(r) \cdot \widehat{M}(r) \cdot \text{rect}\left(\frac{r + \frac{1}{2}\Delta r}{\text{FOV}}\right) = \Delta r \sum_{q=-n'}^{n'-1} \rho(q\Delta r) \delta(r - q\Delta r), \quad (4.31)$$

with the relation,  $\text{FOV} = 2n'\Delta r$ , analogous to that for Eq. (4.26).

Therefore, the discrete and finite sampled signal,  $\hat{S}_d(k)$ , is the Fourier transform of  $\rho_m(r)$ .  $\hat{S}_d(k)$  counterparts to the reconstructed spin density,  $\hat{\rho}_d(r)$ , in Eq. (4.28), given by:

$$\hat{S}_d(k) = \int dr \hat{\rho}_m(r) e^{-i2\pi kr} = \Delta r \sum_{q=-n'}^{n'-1} \rho(q\Delta r) e^{-i2\pi kq\Delta r}. \quad (4.32)$$

### Point Spread Function

Suppose that the k-space data,  $S(k)$ , collected continuously but only from  $-n\Delta k$  to  $(n-1)\Delta k$ . Then, the collected data are said to be truncated by the filter given by the rectangular function  $H_w(k) \equiv \text{rect}\left(\frac{k + \frac{1}{2}\Delta k}{W}\right)$ . The collected data,  $S_w(k)$ , are computed by:

$$S_w(k) = S(k) \cdot H_w(k), \quad (4.33)$$

where  $S(k)$  is the untruncated continuous Fourier transform of the physical spin density,  $\rho(r)$ . The reconstructed image from this data is given by:

$$\rho_w(r) = \text{FT}^{-1}[S(k) \cdot H_w(k)] = \rho(r) * h_w(r). \quad (4.34)$$

Here,  $h_w(r)$  is defined to be the inverse Fourier transform of the  $H_w(k)$ , or the Point Spread Function (PSF). It defines the associated convolutional effects in the image domain, given by:

$$\text{PSF} = h_w(r) = W \text{sinc}(\pi W r) e^{-i\pi \Delta k r}. \quad (4.35)$$

Hence, the truncated acquisition of k-space yields a sinc-shaped point spread profile, i.e. the information in each image location comes from a weighted contribution across the entire acquisition space.



Other factors that modify the MRI signal may also be modelled as filters, such as relaxation exponentials. Furthermore, additional filters may be applied to the data after collection (i.e. post-processing) in order to, for example, enhance certain image features. These additional filters also have an effect on PSF (more details in Chapter 13 in the book of (Brown et al. 2014)).

#### 4.2.5 Noise in MRI

In MRI, the Signal-to-Noise Ratio is a critical parameter in determining the effectiveness of any given imaging experiment. If the SNR is not high enough, it will be impossible to distinguish tissues from each other or the background. Since the signal has been discussed to some extent in previous sections, the study of the noise properties and the development of expressions of SNR that depend on imaging parameters are the primary focus of this section.

Generally, the noise voltage mainly derives from random fluctuations in the receive coil electronics and the sample (Appendix A2). The measured k-space signal is the sum of the true k-space signal,  $S(k)$ , with white noise  $\varepsilon(k)$  added to it to give the noisy measured signal,  $S_m(k)$ :

$$S_m(k) = S(k) + \varepsilon(k). \quad (4.36)$$

Noise  $\varepsilon(k)$  is typically Gaussian distributed with zero mean and variance  $\sigma_{\text{thermal}}$ :  $\varepsilon(k) \sim \mathbf{n}(0, \sigma_{\text{thermal}})$ . This leads to an image noise variation of  $\sigma_I^2 = \sigma_{\text{thermal}}^2/N$  in the image domain, with  $N$  denoting the total number of sampling points. This relationship implies two significant properties between data acquisition and image noise:

1. The variance measured in any voxel in the image domain is the same for all voxels and is  $N$  times smaller than that of the detected signal.
2. As  $N$  increases to  $aN$  ( $a > 1$ ), e.g. longer sampling, the standard noise deviation in the resulting image decreases by a factor of  $1/\sqrt{a}$ .

SNR can be improved by repeating an entire imaging experiment  $N_{\text{acq}}$  times and averaging the signal over these  $N_{\text{acq}}$  measurements (Appendix A2). The averaged k-space signal,  $S_{m,\text{av}}(k)$ , of  $S_m(k)$  is:

$$S_{m,\text{av}}(k) = \frac{1}{N_{\text{acq}}} \sum_{i=1}^{N_{\text{acq}}} S_{m,i}(k). \quad (4.37)$$

The SNR of the k-space signal becomes:

$$\text{SNR}(k) = \frac{\overline{S_{m,av}(k)}}{\sigma_{\text{thermal},av}(k)} = \sqrt{N_{\text{acq}}} \frac{S(k)}{\sigma_{\text{thermal}}(k)}. \quad (4.38)$$

Hence, if the noise is uncorrelated from one experiment to the next, the standard noise deviation is reduced by a factor of  $1/\sqrt{N_{\text{acq}}}$ . This yields an increase in SNR by a factor of  $\sqrt{N_{\text{acq}}}$ .

The image data is complex, with white noise in real and imaginary components. In MRI, the magnitude image is typically used on many occasions. This linear mapping is known to change the noise characteristics (Gudbjartsson & Patz 1995). The signal in magnitude images,  $\tilde{\rho}$ , follows a Rician distribution. The Rician distribution becomes a Rayleigh distribution in the case of a signal-free background. The Rayleigh distribution facilitates the estimation of the standard noise deviation,  $\sigma_{\text{thermal}}$ , from the magnitude image. For an unbiased estimate of SNR, the Rician noise needs to be considered. Typically, this is achieved by a simple correction of the magnitude image intensities, as suggested by (Gudbjartsson & Patz 1995):

$$\rho \approx \sqrt{|\tilde{\rho} - \sigma_{\text{thermal}}^2|}. \quad (4.39)$$

## 4.3 Data Acquisition

The previous sections described the principles of k-space sampling. Various image acquisition approaches exist, each tailored to the individual goals of an MRI experiment. In the case of sodium MRI, the major constraints come from the fast decay of the NMR signal and the complex evolution of multiple quantum coherences. This condition requires dedicated sequence timing concepts and sampling strategies, which are discussed in more detail in this section.

### 4.3.1 MRI Sequence Definition: Gradient-Echo Sequence

An MRI sequence is a specific time scheme of RF excitation pulses, gradients and signal sampling, resulting in a specific image appearance. One typical depiction of an MRI sequence is the sequence diagram, as shown for a gradient-echo sequence in Figure 4.4. This compact depiction shows one block that gets repeated after a Repetition Time (TR). However, the repetitions are not identical since some parameters may vary for each repetition, such as the phase encoding steps (green block), RF phases and receiver phases.

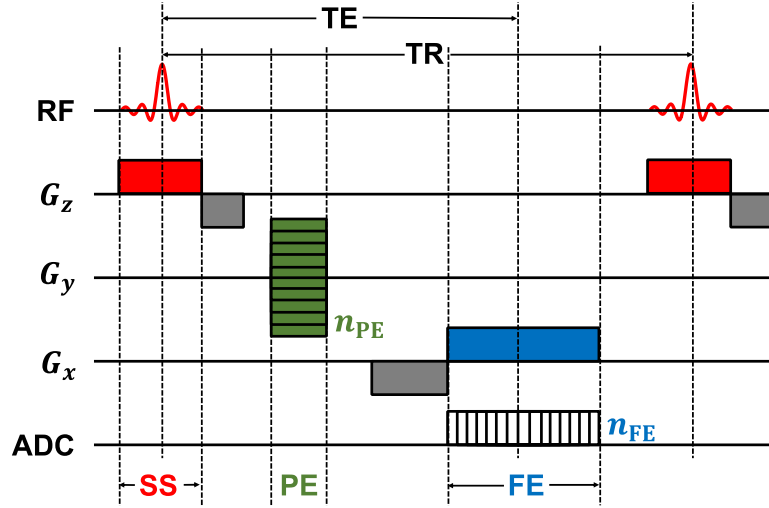


**Figure 4.4** Diagram of a 2D gradient-echo sequence. This sequence performs phase encoding (PE) for  $n_{PE}$  times. The number of frequency encoding (FE) steps is  $n_{FE}$ . SS = slice selection.

The k-space can also be used as a scheme for MRI sequences. The k-space positions traversed during the gradient-echo sequence are shown in Figure 4.5. This map is given by the cumulative sum of the gradient moments in  $x$  and  $y$  directions after each excitation according to Eq. (4.15), called the k-space trajectory of a sequence. In Figure 4.5, the colour code of the k-space line acquisition indicates that this is a centre-reordered gradient-echo sequence with the central k-space lines acquired first, followed by the outer k-space lines. The k-space trajectory of the gradient-echo sequence is a Cartesian grid since the sequence performs Cartesian sampling. In the case of Cartesian sampling, MRI images can be directly reconstructed by performing the inverse Fourier transform (according to Eq. (4.28)) on the acquired raw data.

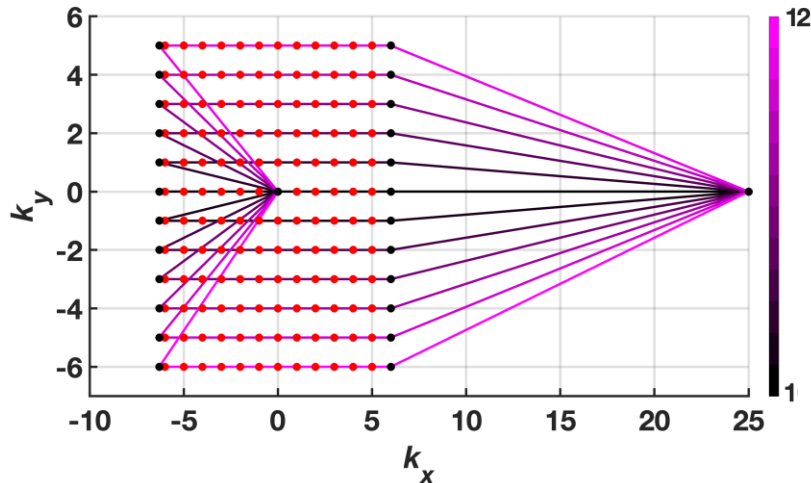


**Figure 4.5** An MRI sequence scheme using k-space. In addition to the sampling locations (red dots), the k-space trajectories (coloured lines) are also given. This scheme reflects the cumulative sum of gradient moments and the coverage of the acquired k-space. The colour code from black to magenta represents the phase encoding steps from 1 to 12.

### 4.3.2 Non-Cartesian Sampling

The fast biexponential sodium NMR signal decay with a rapid component of down to 0.5 msec necessitates a quick onset of data sampling. Therefore, sodium MRI sampling methods usually commence at the centre of the k-space, i.e. right after signal excitation. This centre-out sampling scheme often results in non-Cartesian k-space trajectories. In addition, the non-slice-selective hard pulse is utilised due to its higher efficiency, leading to the Three-Dimensional (3D) acquisition of k-space. The most common of such non-Cartesian 3D sampling patterns are covered below.

#### *Radial*

The shortest (i.e. fastest) trajectory towards high spatial frequencies is a straight line from the centre of k-space,  $k_0$ , to the point of the highest spatial frequency in k-space,  $k_{max}$ . The measurement of k-space is performed through successive trajectories radiating out along different polar and azimuthal angles. This means that the k-space acquisition is conducted in a radial fashion. The recent revival of radial acquisition is mainly due to specialised applications with strict time constraints, i.e. short  $T_2$  species or real-time MRI (e.g cardiac MRI). Each radial spoke describes a projection of an associated plane; therefore, this method is also often called projection imaging. Given the centre-out sampling, each spoke encodes a half-projection.

A uniform sampling of k-space is critical. As shown in Figure 4.6, the work in this thesis employed a 3D radial sampling scheme called DIrection SCHEME Obtained By ALigning points on Latitudes (DISCOBALL) (Stirnberg et al. 2009). This scheme applied a strong simplified version of an approach published by (Saff & Kuijlaars 1997) to achieve a uniform distribution of points on a sphere. The gradient waveforms of a representative projection of this 3D radial sampling scheme are shown in Figure 4.7a.

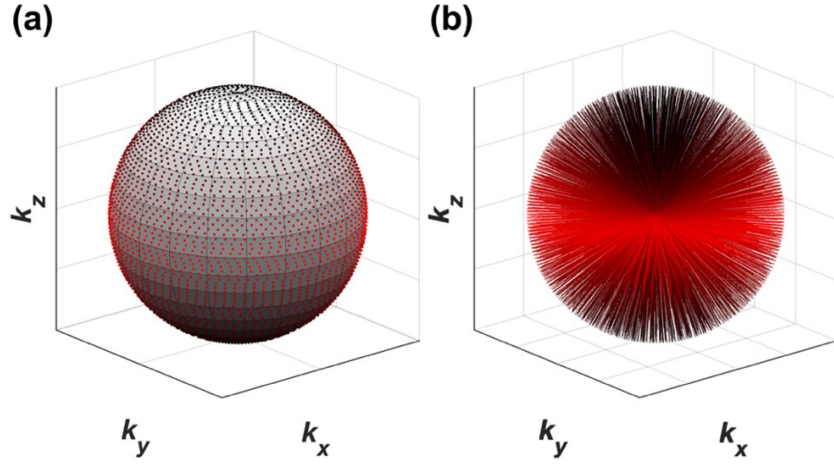


**Figure 4.6** DISCOBALL radial k-space sampling. The DISCOBALL scheme employs 4452 projections for (a) a homogeneous distribution of points in a sphere and (b) the corresponding k-space trajectories. Points and projections are colour-coded from black to red, indicating that DISCOBALL first acquires k-space lines at the top and bottom of the sphere and then the k-space projections in the middle.

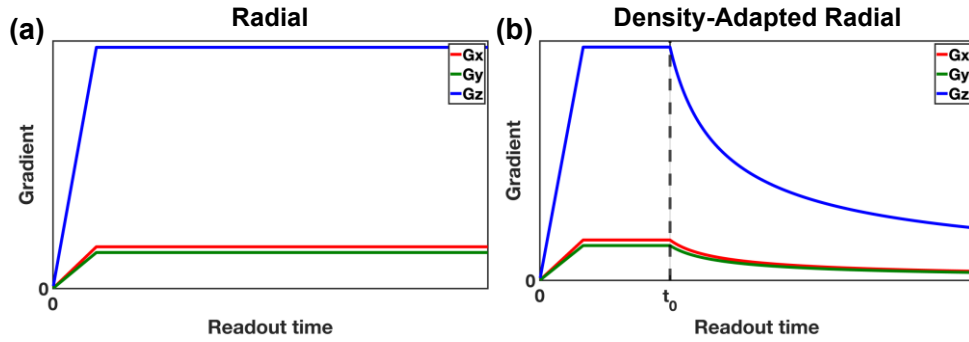


**Figure 4.7** Representative gradient waveforms for 3D radial sampling. Gradient ramp-up and initial traversal are identical for (a) 3D radial and (b) 3D density-adapted acquisitions up until  $k_0$  at  $t_0$  indicated by the black dashed line. This line marks the onset of density adaption, achieved by a reduction in gradient strength and a consequent slow-down in k-space traversal speed. Gradient ramp-down is not shown here.

Whereas radial sampling provides the fastest traversal of k-space from the centre to the periphery, the resulting pattern is characterised by substantial variations in sampling density, with a high oversampling of the k-space centre and a decrease in density towards higher spatial frequencies. This non-uniformity causes a reduction in image SNR due to an inhomogeneous distribution of noise in k-space (Liao et al. 1997).

An improvement in the sampling density of 3D radial trajectories in sodium MRI was proposed by (Nagel et al. 2009). The 3D density-adapted radial sampling approach is based on the modification of the gradient shapes such that the outer part of the k-space maintains a constant sampling density. As shown in Figure 4.7b, the method follows a standard radial trajectory up to  $k_0$  and then density-corrected sampling from  $k_0$  to  $k_{max}$ . The value of  $k_0$  is determined by hardware limitations, such as maximum gradient strength or slew rate. Density-adapted 3D

radial sampling has two main advantages: (1) its implementation is relatively simple and flexible since it is based on a standard radial sequence; (2) for a fixed readout duration, compared with a standard radial sampling, the increased sampling uniformity improves the image SNR.

Various twisted/spiral sampling schemes have also been employed to improve k-space sampling uniformity and efficiency, such as Twisted Projection Imaging (TPI) (Appendix A3), 3D Cones (Appendix A3) and Fermat Looped, ORthogonally Encoded Trajectories (FLORET).

#### ***Fermat Looped, Orthogonally Encoded Trajectories***

When choosing a trajectory, a number of metrics should be considered, such as the time to sample a particular volume of k-space, the relative SNR due to data weighting, off-resonance artefact expression, motion, sensitivity to eddy currents and the nature of undersampling (relevant to parallel imaging and non-linear iterative reconstruction methods). Another desirable characteristic is the ease of trajectory design and sequence implementation.

This thesis adopted a rapid 3D centre-out k-space sampling scheme proposed by (Pipe et al. 2011). This method is based on a Fermat spiral 2D trajectory, called Fermat Looped, ORthogonally Encoded Trajectories (FLORET). The 2D Fermat spiral (Figure 4.8a) is given by:

$$k_r = c * \theta^{1/2}, \quad (4.40)$$

where  $c$  is a constant determining the variable pitch rate;  $k_r$  and  $\theta$  are the trajectory radius and angle in polar coordinates. The Fermat spiral is characterised by substantial undersampling in the centre of k-space, followed by an increase of sampling density towards higher spatial frequencies. This can also be seen by taking the derivative of Eq. (4.40) with respect to  $\theta$ :

$$\frac{dk_r}{d\theta} = \frac{c}{2} \theta^{-1/2} = \frac{c^2}{2} \frac{1}{k_r}. \quad (4.41)$$

A 3D interleaf is played out in each TR by projecting the base 2D spiral trajectory onto a cone concentric with a given axis (e.g. the  $k_z$  axis), as illustrated in Figure 4.8b. The cone is defined by the angle of its surface with a plane perpendicular to this axis (e.g.  $k_x$ - $k_y$  plane),  $\alpha$ .

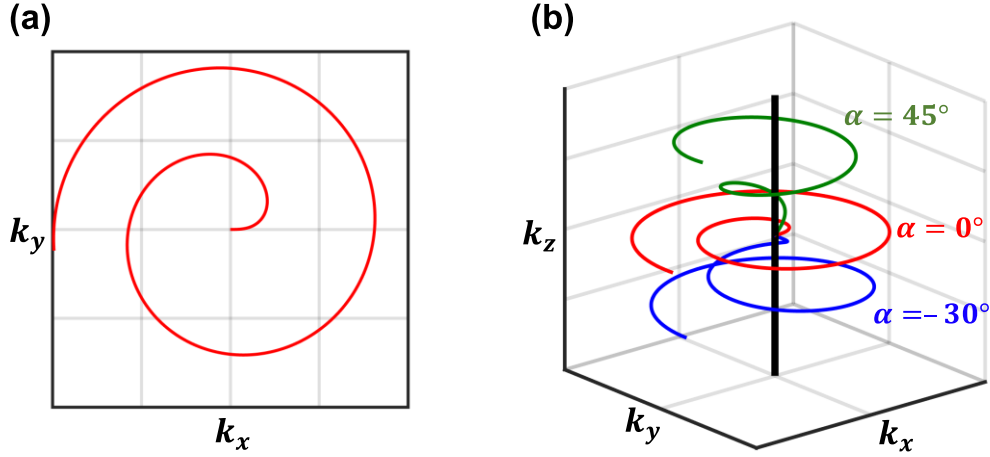


**Figure 4.8** 2D Fermat spiral trajectory. By projecting the base 2D Fermat spiral **(a)** onto a cone, an interleaf of 3D FLORET **(b)** is generated. The cone is concentric with a given axis shown as the thick black line (here defined as the  $k_z$  axis) and defined by a certain angle,  $\alpha$ , between its surface and the plane (here  $k_{xy}$  plane) perpendicular to the given axis.

The interleaf played out on a cone at the angle  $\alpha$  is based on the base 2D Fermat spiral trajectory  $\{b_x(t), b_y(t)\}$  as:

$$\begin{cases} k_x(t) = \cos(\alpha) \cdot b_x(t) \\ k_y(t) = \cos(\alpha) \cdot b_y(t) \\ k_z(t) = \sin(\alpha) \cdot \sqrt{b_x^2(t) + b_y^2(t)} \end{cases} \quad (4.42)$$

In addition, each interleaf is also rotated by an angle,  $\beta$ , about the given axis (e.g. the  $k_z$  axis) by the golden angle (Winkelmann et al. 2007),  $\pi \cdot (3 - \sqrt{5})$ , relative to its neighbours. The set of  $N$  interleaves formed about a given axis is called a hub, with successive interleaves lying on cones with angles linearly changing from  $+\alpha_0$  to  $-\alpha_0$ . Thus, the  $n^{\text{th}}$  interleaf in a hub is played out on a cone at an angle,  $\alpha_n$ :

$$\alpha_n = \alpha_0 \left[ 1 - \frac{2n}{N-1} \right], n \in [0, 1, 2, \dots, N-1], \quad (4.43)$$

and is rotated about, for example, the  $k_z$  axis by:

$$\beta_n = n\pi(3 - \sqrt{5}). \quad (4.44)$$

If the cones are concentric about the  $k_z$  axis, as denoted thus far, this hub is called a  $k_z$  hub (Figure 4.9a). An important feature of this hub is that as the trajectories fan out with  $k_r$ , the overall angular sampling distance becomes proportional to  $k_r$ , while the radial sampling distance is proportional to  $1/k_r$ . This feature, along with the spacing resulting from the golden angle (Eq. (4.44)), leads to a very uniform inter-trajectory spacing.

By rotating the  $k_z$  hub with  $\alpha_0 = 45^\circ$  around  $k_x$  by  $90^\circ$ , the  $k_y$  hub (Figure 4.9b) is generated. Similarly, the  $k_x$  hub (Figure 4.9c) is produced by rotating the  $k_z$  hub around  $k_y$  by  $90^\circ$ . By combining these three hubs, the FLORET can thoroughly sample the entire sphere of k-space twice in orthogonal directions (three times in some small transition regions) (Figure 4.9d). The gradient waveforms of a representative FLORET interleaf of the FLORET sphere are shown in Figure 4.10.

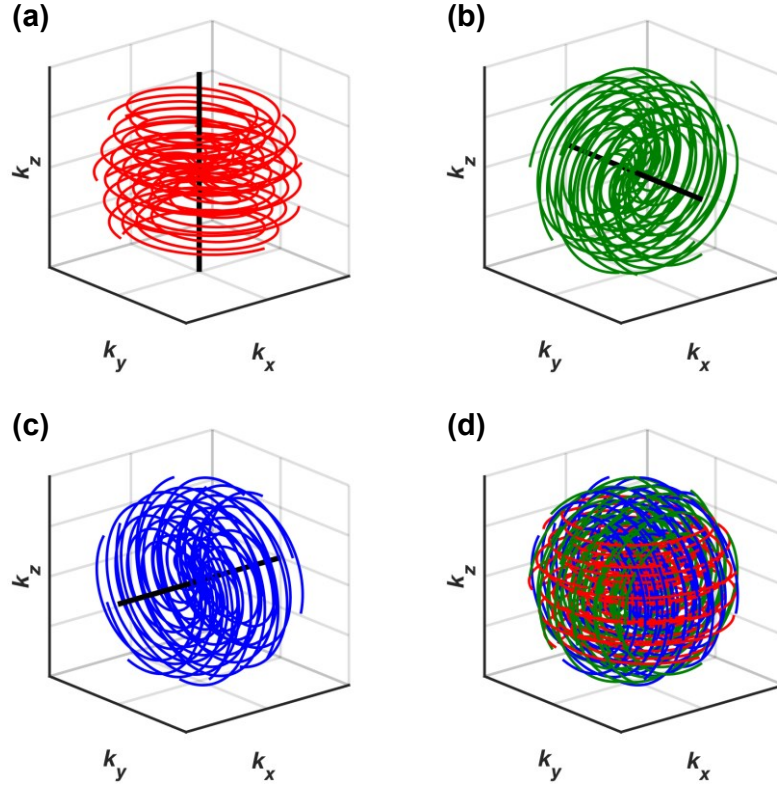


**Figure 4.9** FLORET k-space trajectories. The (a)  $k_z$  hub, (b)  $k_y$  hub and (c)  $k_x$  hub are combined to form a FLORET sphere in k-space.

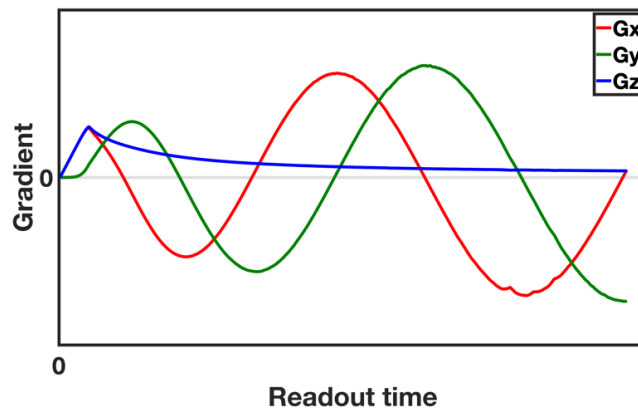


**Figure 4.10** Gradient waveforms of a representative interleaf of the FLORET sphere in k-space.



A unique feature of FLORET is the two-fold oversampling in the orthogonal directions. This feature creates interesting properties in the presence of deliberate data undersampling. The first property is that, in the case of undersampling, the “cross-hatch” sampling pattern keeps the undersampling regions both localised and irregular. Figure 4.11 illustrates the effect of uniform undersampling by a factor of nine on PSFs. The random pattern of the PSFs is desirable both for incoherent representation of undersampling artefacts and for non-linear iterative reconstruction (Lustig et al. 2007). Another unique aspect of undersampling in FLORET is that the inefficiency inherent in FLORET’s design, i.e. two-fold oversampling, decreases as undersampling increases. For example, in the case of Nyquist acquisition, FLORET doubles the number of interleaves of a stack of spirals (Mirkes et al. 2016); however, it requires approximately the same number of trajectories to sample 1/3 of the volume or less (Pipe et al. 2011).

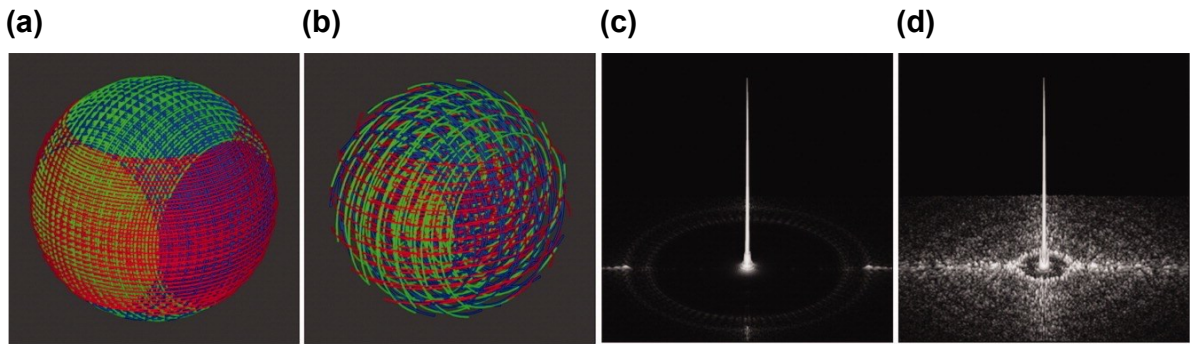


**Figure 4.11** Undersampling of FLORET results in incoherent aliasing. A (a) fully sampled and (b) nine-fold undersampled trajectory sets are illustrated, along with 2D cross sections of their respective PSFs (c, d). **Source:** Figure reproduced from (Pipe et al. 2011) with permission from John Wiley and Sons (License No. 5745411307698).

The FLORET trajectory is gradient-efficient and uniformly spaced, improving SNR and scan time efficiency. It has the beneficial properties of centre-out methods with low gradient moments, which are desirable for acquiring fast-decaying NMR signals such as sodium signals. In addition, FLORET produces very incoherent aliasing artefacts, making it an excellent candidate for CS-based reconstruction. Finally, the design and implementation of FLORET are straightforward, requiring the design of only one base Fermat spiral waveform.

### 4.3.3 Ultra-short Echo Time Acquisition

The acquisition of a fast-decaying NMR signal requires a dedicated sequence with an emphasis on the rapid start of sampling, i.e. ADC onset. The sequence with Ultra-short Echo Time described below is one of the sequence families that focuses on the acquisition of fast  $T_2$  species.

UTE sequences implement a straightforward sequence timing concept where signal acquisition commences immediately after RF excitation, as in a standard pulse-acquire experiment. The k-space traversal is performed with signal detection, i.e. all encoding gradients are turned on during the ADC. This yields a sampling pattern that commences in the centre of k-space with radial or spiral gradient waveforms, as described in Section 4.3.2. For time reasons, RF excitation is performed using a more efficient rectangular hard pulse without slice selection gradients (Section 4.2.2), which results in a 3D acquisition of k-space.

Figure 4.12 depicts the sequence diagram of a spiral UTE acquisition. The hardware constraints affect the switching time between RF excitation and ADC sampling, commonly denoted transmit-receive switch time or dead time,  $t_d$ . For standard clinical systems, this time ranges between 40 to 100  $\mu$ s; and yet the waiting time for sampling onset is often chosen conservatively more to the longer end of this time range. In addition, the limited  $B_1$  field strength results in a finite pulse duration,  $t_{RF}$ , typically on the order of a few hundred microseconds for a  $\pi/2$ -pulse in sodium MRI at 7T. The sampling onset time, TE, is defined as the time interval originating from the system dead time and half the length of the excitation pulse:

$$TE = \frac{1}{2}t_{RF} + t_d, \quad (4.45)$$

where the notation TE is slightly misleading since only a simple free induction decay signal is sampled, and no echo is created. However, this term is conventionally used for the definition of sampling onset in the centre of k-space.

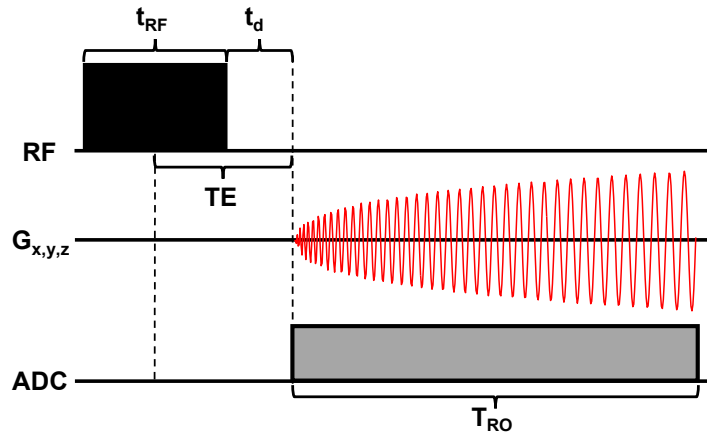


**Figure 4.12** Diagram of a spiral UTE sequence. Gradient and data acquisition are synchronised and commence after the dead time,  $t_d$ . ADC readout length is denoted as  $T_{RO}$ . The echo time, TE, results from  $t_d$  and the RF pulse length,  $t_{RF}$ .

#### 4.3.4 Multiple-Quantum Filter: Phase Cycling

As mentioned in Section 3.5, sodium nuclei experience complex evolution of multiple quantum coherences in various environments. If the difference in the azimuthal quantum numbers of two states is  $\Delta m = \pm 1$ , the coherence is related to the transverse magnetisation. If  $\Delta m \neq \pm 1$ , the coherence does not lead to observable magnetisation and can only be detected indirectly. A sequence of RF pulses that perturbs the equilibrium density matrix, creating transitions with  $\Delta m \neq \pm 1$ , and then converts the multiple quantum coherences into observable signal (i.e. transverse magnetisation) is called a multiple-quantum filter. It consists of three or more non-slice selective RF pulses.

A phase cycling technique (Jaccard et al. 1986) is always associated with a multiple-quantum filter to measure signals from different coherence orders. It allows one to capture the signal from desired coherence transfer pathways and filter out that from undesired pathways. In most MRI experiments, the phase of the transmitter is normally locked to the phase of the receiver. Changing these phases independently through phase cycling results in proper signal pathway creation. The receiver phase is changed during phase cycling, generally between 0 and  $\pi$ . Only the coherences with the same phase shift relative to the receiver will contribute to the signal. Thus, the signals are additionally influenced through the receiver phase,  $\phi_{\text{rec}}$ , and the numerical phase,  $\phi_{\text{num}}$ , which is applied in post-processing. The RF pulses of the sequence possess phases, which are shifted appropriately, and the resulting signals are dedicatedly added.

The effect of the phase  $\phi$  of the RF pulse is to change the axis about which the spin polarisations rotate. The rotation axis is still in the  $xy$ -plane but subtends an angle  $\phi$  with respect to the  $+x$ -axis. For example, a pulse of a phase  $\phi = 0$  (or  $\pi/2$ ) rotates the spin polarisation around the  $+x$ -axis (or  $+y$ -axis) through an angle equal to the flip angle of the RF pulse,  $\theta = -\gamma B_1 \tau_{\text{RF}}$ , where  $\tau_{\text{RF}}$  is the RF duration. The rotating-frame Hamiltonian during the RF pulse is given as:  $\hat{H}_{\text{RF}} = -\gamma B_1 (\hat{I}_x \cos \phi + \hat{I}_y \sin \phi)$  (Levitt 2008). The evolution of the spherical tensor operators  $T_{lp}$  (with rank  $l$  and coherence order  $p$ ) under this RF Hamiltonian is given in terms of the arrow notation by (Sørensen et al. 1984):

$$T_{lp} \xrightarrow{\hat{H}_{\text{RF}}} \sum_{p'=-l}^{p'=l} T_{lp'} d_{pp'}^{(l)}(\theta) e^{-i\Delta p \phi}, \quad (4.46)$$

where  $p'$  denotes the new coherence order;  $\Delta p = p' - p$  is the change of the coherence order under the RF pulse;  $I$  is the nuclear spin quantum number of the nucleus; and  $d_{pp'}^{(I)}$  is the Winder rotation matrix elements presented in (Müller et al. 1987). Free precession in the absence of RF perturbations changes the rank  $l$  of the tensors without affecting the order. The rank indicates the potential of a density operator to evolve for a certain coherence order. For example, rank-3 Single-Quantum can evolve to Triple-Quantum coherences, whereas rank-1 SQ coherences cannot.

Since the longitudinal magnetisation possesses the coherence order  $p = 0$ , the pathways start with this value, and the transverse magnetisation is excited with the first RF pulse and detected with the last RF pulse with  $p = -1$ , which is the only detectable coherence. Under the influence of  $i^{\text{th}}$  RF pulses with phase  $\varphi_i$  ( $i = 1, \dots, N$ ), the pathway is characterised by a vector:  $\Delta p = \{\Delta p_1, \dots, \Delta p_N\}$ . The measured signal  $s(t)$  is a superposition of contributions from all pathways:  $s(t) = \sum_{\Delta p} s^{\Delta p}(t)$ .

For a single pathway,  $\Delta p$ , the signal  $s^{\Delta p}(\Phi, t) = s^{\Delta p}(0, t)e^{-i\Delta p\Phi}$  is associated with a phase shift  $e^{-i\Delta p\Phi}$ , which depends on the phases of  $N$  RF pulses:  $\Phi = \{\varphi_1, \dots, \varphi_N\}$  (Bodenhausen et al. 1984). The separate measurements of the desired coherence pathway,  $s^{\Delta p}$ , is achieved by applying a phase cycling scheme for relative RF phases (Zhu & Smith 1995). The phase cycling scheme implemented for a sequence is a phase cycle with  $M$  steps, with the counter  $j = 0, 1, \dots, M-1$ . This can be used to separate the signals from single pathways using the inverse Fourier transform. To acquire signal from the desired pathway, all combinations of  $j$  for every  $i^{\text{th}}$  of  $N$  RF pulses are combined with single phases being  $\varphi_i = j_i 2\pi/M_i$  as:  $s^{\Delta p}(t) = M_1^{-1} \dots M_N^{-1} \cdot \sum_{j_1=0}^{M_1-1} \dots \sum_{j_N=0}^{M_N-1} s(t) e^{i(\Delta p_1 \varphi_1 + \dots + \Delta p_N \varphi_N)}$ . In a sequence consisting of three RF pulses, the overall phase change accumulated after the coherence transfer is:  $\Psi_{\Delta p}(j) = \varphi_1 \Delta p_1(j) + \varphi_2 \Delta p_2(j) + \varphi_3 \Delta p_3(j) + \varphi_{\text{rec}}(j) + \varphi_{\text{dig}}(j)$ , where  $\varphi_{\text{dig}}$  is the phase offset relative to the hardware. The signal from pathway  $\Delta p$  is detected, if  $M^{-1} \cdot \sum_{j=0}^{M-1} e^{i\Psi_{\Delta p}(j)} = 1$ .

Multiple phase cycling stores the signals from each phase step  $s_m(t)$  separately and combines them in post-processing:  $s^{(P)}(t) = \sum_{j=0}^{M-1} s_j(t) e^{-i\varphi_{\text{num}}^{(P)}(j)}$ . Index  $P$  describes the desired pathway. Therefore, the appropriate choice of the numerical phase  $\varphi_{\text{num}}$  allows for detecting desired pathways.

## 4.4 Image Reconstruction

As described in the previous sections, the relatively complicated signal sampling strategies in sodium MRI result in 3D non-Cartesian raw data, justifying the necessity for elaborate image computation.

Non-Cartesian image reconstruction methods can be broadly classified into (1) standard reconstruction and (2) non-linear iterative reconstruction. The former aims to calculate an image from the measured projections only, whereas the latter determines image formation by solving constrained optimisation problems. Since standard reconstruction methods rely solely on measured raw data, such methods require a sufficiently sampled k-space, as explained in Section 4.2.4. Non-linear iterative approaches can incorporate additional knowledge about the underlying objects, enabling the reconstruction of images from NMR signals sampled below the Nyquist sampling rate.

In the following, an introduction to sodium MRI reconstruction is given. After a short explanation of the required raw data pre-processing – density compensation, the standard reconstruction methods, exemplified by gridding, are described. Furthermore, a typical non-linear iterative reconstruction approach, Compressed Sensing, is discussed. Finally, the evaluation approaches of image reconstruction performance are briefly listed.

### 4.4.1 Density Compensation

Independent of the chosen reconstruction scheme, non-Cartesian raw data requires pre-processing for the sampling inhomogeneity, which is called density compensation. In general, centre-out non-Cartesian trajectory schemes (e.g. 3D radial) suffer from a strong oversampling in the central part of k-space. According to Eq. (4.33) – (4.35), the central oversampling results in a PSF with a larger Full Width at Half Maximum (FWHM). A “wider” PSF results in a degraded localisation performance, which causes blurring and information loss of small structures in the reconstructed image. This leads to the realisation that some weighting must be included to account for the sampling density.

A good description of general inhomogeneity compensation can be found in (Pipe & Menon 1999). In particular, numerical computation of the area associated with each data sample is often used as the density estimate. The area is approximated by the spacing of samples along the trajectory multiplied by the spacing between adjacent trajectories. This thesis used a numerical algorithm called the Voronoi diagram for density estimation (Rasche et al. 1999).

The remarkable thing about the Voronoi diagram is its very efficient algorithms for computation, making it very attractive for density estimation.

#### 4.4.2 Standard Non-Cartesian Reconstruction: Gridding

Generally, non-Cartesian MRI data is reconstructed by using methods that essentially aim to associate the measured data with a Cartesian grid. Using the convenient Fourier relationship between k-space and image space (Eq. (4.10)), uniformly spaced n-dimensional Cartesian data can be reconstructed very efficiently via an n-dimensional Fast Fourier Transform (FFT) (Cooley & Tukey 1965).

For the application of FFT, the sampled data points have to lie on a Cartesian grid. If the acquisition scheme is not inherently Cartesian, a gridding reconstruction method can be used to approximate the measured data samples onto a Cartesian grid. The basic idea of gridding is illustrated in Figure 4.13. Data points lie on certain trajectories through k-space. Each data point is convolved with a gridding kernel, and the results are sampled and accumulated on a Cartesian grid. After all data samples have been processed, an FFT produces a reconstructed image.

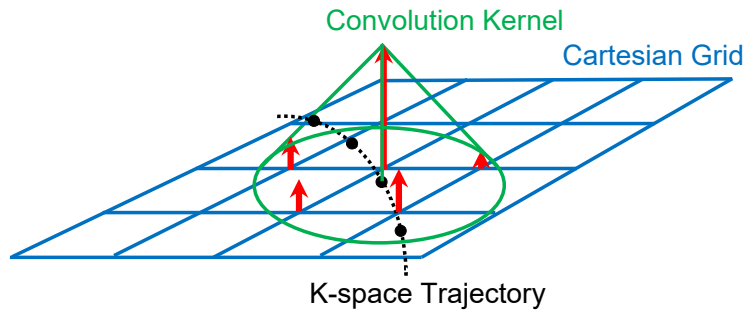


**Figure 4.13** Basic idea of gridding. The data samples (black dots) lie on some trajectory through k-space (dashed line). Each data point is conceptually convolved with a gridding kernel (green cone). The convolution is evaluated at the adjacent grid points (red arrows).

The overview of this gridding framework is displayed in Figure 4.14. The overall concept of gridding can be described with mathematics as follows (Jackson et al. 1991).

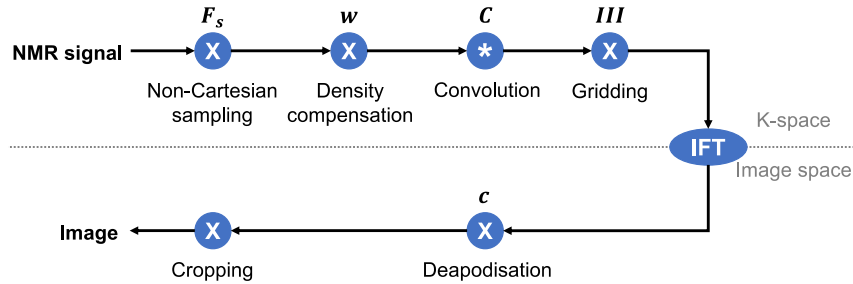


**Figure 4.14** Overview of the gridding process.

### Sampling Data

As described in Eq. (4.10), the NMR-signal acquisition  $S$  in 3D k-space  $(k_x, k_y, k_z)$  is related to the imaged spin ensemble  $\rho$  in 3D image space  $(x, y, z)$  through a Fourier Transform:

$$S(k_x, k_y, k_z) = \int_{-\infty}^{\infty} \rho(x, y, z) \exp[-2\pi i(k_x x + k_y y + k_z z)] dx dy dz. \quad (4.47)$$

According to Eq. (4.17), the sampled signal is denoted  $S_d$  and is measured by a non-Cartesian sampling function,  $F_s$ :

$$S_d(k_x, k_y, k_z) = S(k_x, k_y, k_z) \cdot F_s(k_x, k_y, k_z), \quad (4.48)$$

with  $F_s(k_x, k_y, k_z) = \sum_{i=1}^N \delta(k_x - k_{x,i}, k_y - k_{y,i}, k_z - k_{z,i})$ ,

where  $F_s$  describes a general discrete sampling with variable density. In case of a non-uniform distribution of data samples, the acquired signal,  $S_d$ , needs to be compensated for these density-inhomogeneities. The weighted signal is given as  $S_{dw}(k_x, k_y, k_z) = S(k_x, k_y, k_z) \cdot F_s(k_x, k_y, k_z) \cdot w(k_x, k_y, k_z)$ , where  $w(k_x, k_y, k_z)$  is the density compensation factor of a sampled k-space data point at the position of  $(k_x, k_y, k_z)$ .

### Convolution

The finite image support yields a convolution of the sampling space with a sinc function (Eq. (4.35)). Denoting the sampled and convolved signal,  $S_{dc}$ , this apodisation effect can be incorporated through a convolution kernel,  $C(k_x, k_y, k_z)$ :

$$S_{dwc} = [S(k_x, k_y, k_z) \cdot F_{sw}(k_x, k_y, k_z)] * C(k_x, k_y, k_z), \quad (4.49)$$

where  $F_{sw}(k_x, k_y, k_z)$  is the non-Cartesian sampling function after density compensation. Ideally, the acquired signal would be convolved with a sinc function. The infinite range of the sinc function representing contribution from all measurement points to each grid point makes its implementation impractical. Instead, several other convolution functions (e.g. cosines and Gaussian) have been investigated in (Jackson et al. 1991).

A truncated zero-order prolate spheroidal wave function of the first kind is well band-limited, i.e. it exhibits minimal energy outside the desired bandwidth. However, it is also computationally challenging. The Kaiser-Bessel function approximates this zero-order function and has been shown to be an optimal gridding kernel. It is easy to compute the Kaiser-Bessel in both the frequency and image domains.

The One-Dimensional (1D) Kaiser-Bessel function in the frequency domain is formulated as:

$$C_{KB}(k) = \frac{I_0 \left[ b \sqrt{1 - \left( \frac{2k}{w} \right)^2} \right]}{I_0(b)} \text{rect} \left( \frac{2k}{w} \right), \quad (4.50)$$

where  $I_0$  is the zero-order modified Bessel function of the first kind;  $w$  denotes the kernel width;  $b$  is a tuning parameter; and  $\text{rect}$  is a rectangular function.

In the image domain, 1D Kaiser-Bessel function becomes:

$$C_{KB}(x) = \frac{\sin \left( \sqrt{\pi^2 w^2 x^2 - b^2} \right)}{\sqrt{\pi^2 w^2 x^2 - b^2}}, \quad (4.51)$$

with kernel width,  $w$ , and tuning parameter,  $b$ .

### Gridding

After convolving the sampled data with a finite Kaiser-Bessel kernel, the filtered sampling points are gridded onto a Cartesian grid via a “Dirac comb” function:

$$\text{III} \left( \frac{k_x}{\Delta k_x}, \frac{k_y}{\Delta k_y}, \frac{k_z}{\Delta k_z} \right) = \sum_i \delta \left( \frac{k_x}{\Delta k_x} - i \right) \sum_j \delta \left( \frac{k_y}{\Delta k_y} - j \right) \sum_k \delta \left( \frac{k_z}{\Delta k_z} - k \right). \quad (4.52)$$

The discretised, convolved, and re-sampled signal is given by:

$$S_{\text{dwcs}}(k_x, k_y, k_z) = \left[ \left( S(k_x, k_y, k_z) \cdot F_{\text{sw}}(k_x, k_y, k_z) \right) * C(k_x, k_y, k_z) \right] \cdot \text{III} \left( \frac{k_x}{\Delta k_x}, \frac{k_y}{\Delta k_y}, \frac{k_z}{\Delta k_z} \right). \quad (4.53)$$

### Inverse Fourier Transform

By performing an inverse Fourier transform on Eq. (4.53), a reconstructed image,  $\hat{\rho}$ , is produced:

$$\hat{\rho}(x, y, z) = \left[ \left( \rho(x, y, z) * f_{\text{sw}}(x, y, z) \right) \cdot c(x, y, z) \right] * \text{III} \left( \frac{x}{FOV_x}, \frac{y}{FOV_y}, \frac{z}{FOV_z} \right) \quad (4.54)$$

The elements of Eq. (4.54) have various effects. The ideal image,  $\rho(x, y, z)$ , is first blurred by convolution with the inverse Fourier transform of the sampling function,  $f_{\text{sw}}(x, y, z)$ . In addition, sidelobes are often created due to the pattern of the samples in  $k$ -space (e.g. ring sidelobes caused by spiral sampling). Next, the image is apodised (i.e. higher spatial



frequencies are scaled down smoothly) by the inverse Fourier transform of the gridding kernel,  $c(x, y, z)$ . While this apodisation effect causes attenuation at the image borders, it also has the desirable effect of suppressing the sidelobes generated by the convolution with the sampling function. Finally, the finite discrete sampling in k-space causes replication in the image space. Sidelobes from the first replicas interfere with the desired image.

### ***Deapodisation***

The apodisation effect described above can be corrected by dividing the reconstructed image,  $\hat{\rho}(x, y, z)$ , by the inverse Fourier Transform of the applied gridding kernel. For example, this deapodisation function is given in Eq. (4.51) for a Kaiser-Bessel window.

After deapodisation, the reconstructed image,  $\hat{\rho}$ , of the detected spin ensemble,  $\rho$ , is given as:

$$\hat{\rho}(x, y, z) = \frac{1}{c(x, y, z)} \cdot \left\{ \left[ \left( \rho(x, y, z) * f_{\text{sw}}(x, y, z) \right) \cdot c(x, y, z) \right] * \text{III} \left( \frac{x}{\text{FOV}_x}, \frac{y}{\text{FOV}_y}, \frac{z}{\text{FOV}_z} \right) \right\}. \quad (4.55)$$

Note that the deapodisation occurs after the convolution of the  $\text{III}(\cdot)$  function.

### ***Oversampling***

So far, a severe problem lies in that the adjacent replica sidelobes have the same amplitude as the desired image at the edge of the FOV. This problem is because there is no space for a transition band between the desired image and the replica sidelobes. This is a consequence of reconstructing the image using the same grid as the underlying sampling of the k-space data (referred to as the “1X” grid). It is possible to choose a denser grid at the only cost of increased computation time. Reconstruction on a denser grid,  $\left( \frac{\Delta k_x}{\alpha}, \frac{\Delta k_y}{\alpha}, \frac{\Delta k_z}{\alpha} \right)$ , with  $\alpha > 1$ , allows for a transition band to move the replica sidelobes out of the FOV and significantly reduce both the apodisation and aliasing. Then, the reconstructed image becomes:

$$\hat{\rho}(x, y, z) = \frac{1}{c(x, y, z)} \cdot \left\{ \left[ \left( \rho(x, y, z) * f_{\text{sw}}(x, y, z) \right) \cdot c(x, y, z) \right] * \text{III} \left( \frac{x}{\alpha \text{FOV}_x}, \frac{y}{\alpha \text{FOV}_y}, \frac{z}{\alpha \text{FOV}_z} \right) \right\}. \quad (4.56)$$

After reconstruction, the oversampled image can be cropped to obtain the desired size. In practice, a 2X grid ( $\alpha = 2$ ), i.e. two-fold oversampling, is commonly used and yields good performance for most reasonable convolution kernels. The only disadvantage is the increased

computation time for the discrete Fourier transform and the fact that it becomes expensive in terms of memory requirement in 3D acquisitions. The Non-uniform Fast Fourier Transform can be used to speed up Fourier transform calculations for non-uniformly spaced data. Its detailed theory is presented in (Fessler & Sutton 2003).

Part of the work presented in the following 4.4.3 and 4.4.4 sections were published in: **Chen Q.**, Shah N. J., Worthoff W. A.: Compressed Sensing in Sodium Magnetic Resonance Imaging: Techniques, Applications, and Future Prospects. *J. Magn. Reson. Imaging* (2022) 55: 1340–1356.

### 4.4.3 Non-linear Iterative Reconstruction: Compressed Sensing

In general, non-uniform acquisition of k-space is inefficient because the Nyquist criterion needs to be satisfied in the least densely sampled region of k-space. Consequently, other areas of k-space are oversampled, which is usually associated with increased measurement times. Long MRI scans could lead to motion artefacts, high costs and patient discomfort.

Accurate reconstruction of specific signals or images from raw data sampled below the Nyquist sampling criterion is of central interest in many disciplines. It is the foundation of a sampling and reconstruction scheme called Compressed Sensing. CS is based on the principle that an image with a sparse representation in a transform domain can be recovered from incoherent undersampled k-space data by a non-linear iterative reconstruction.

In the following, the basic concepts of CS and the application of CS to MRI (in particular, sodium MRI) are introduced. The explanation of the theory of CS follows the work of (Candès et al. 2006b, 2006a; Donoho 2006). The introduction of the specific application of this theory to MRI is based on the work published by (Lustig et al. 2007).

Biomedical images are naturally compressible with little or no visual loss of information. Traditionally, image compression is performed after image acquisition to save transfer time and storage space. The image content is transformed to a vector of sparse coefficients through compression tools (e.g. wavelet transform or Discrete Cosine Transform (DCT)). Standard compression strategies are used to encode the few important coefficients and discard the most unimportant or negligible coefficients, thus achieving near-perfect reconstruction of the original data. Since sodium MRI suffers from relatively low image quality and associated long measurement times, reducing scan time without significantly degrading image quality is critical for it to become clinically feasible. The following question naturally arises: Is it possible to directly obtain compressed information from MRI images while retaining most of the reconstructed image quality?

Note that MRI scanners naturally measure Fourier-encoded coefficients (i.e. k-space samples) instead of pixels, wavelet or DCT coefficients (Eq. (4.12)). Thus, the above question can be restated: Can one reconstruct MRI images without significant perceptual loss by sampling a small subset of the k-space? The mathematical theory of CS proposed by (Candès et al. 2006b, 2006a; Donoho 2006) clears the path for MRI acceleration. According to the mathematical results, there are three fundamental requirements for the application of CS to MRI (Lustig et al. 2007), as follows:

1. The image must have a sparse representation in a transform domain so that the noise can be separated and removed from the desired image content.
2. The undersampled k-space data should have low coherence so that the generated artefacts exhibit a noise-like pattern in the image domain and even more so in a properly chosen transform domain.
3. The desired image should be reconstructed using a non-linear iterative reconstruction to balance the sparse representation of the desired image and the data consistency of the reconstructed image with the acquired k-space data.

The above three ingredients are discussed one by one in more detail as follows.

### ***Transform Sparsity***

A vector is “sparse” if most of its coefficients equal zero and only a few contain all information. From the perspective of signal processing, most energy of a sparse signal is contained in a few measurements, while others are zero or negligible. In mathematical terms, the transform sparsity can produce a sparse vector after a specific transformation, defined as follows: If an unknown signal with  $m$  samples is a vector,  $x \in \mathbb{C}^m$ , which can be expressed in terms of an orthonormal basis set  $(\psi_i: i = 1, \dots, m)$  for  $\mathbb{C}^m$  (e.g. orthonormal wavelet basis), as follows:

$$\theta_i = \psi_i^* x, \quad i = 1, \dots, m \quad \text{or} \quad \theta = \Psi x, \quad (4.57)$$

where  $\theta \in \mathbb{C}^m$  is the transform coefficient set of  $x$ ; the orthonormal basis set  $(\psi_i: i = 1, \dots, m)$  in matrix form,  $\Psi \in \mathbb{C}^{m \times m}$ , is known as sparsifying transform operator. Then, the signal,  $x$ , is said to be  $k$ -sparse if only  $k$  elements of  $\theta$  are non-zeroes ( $k \ll m$ ), while the remaining  $(m - k)$  elements are zeroes (as shown in Figure 4.15a).

Sparsifying transform projects an MRI image into a sparse domain based on some transform coefficients, thereby suggesting the number of measurements demanded by exact reconstruction. However, selecting the right sparsifying transform tool to exploit the sparsity

of a particular class of images is a challenging task and an ongoing research field. Fixed sparsifying transform operators are frequently employed in sodium MRI, such as wavelets (Blunck et al. 2019), finite differences (Behl et al. 2016; Lachner et al. 2019; Utzschneider et al. 2021) or the orthogonal DCT (Blunck et al. 2019). Furthermore, it is possible to conduct a sparse representation of sodium MRI images based on a trained dictionary (Behl et al. 2016; Platt et al. 2018; Utzschneider et al. 2020, 2021) or others (Adlung et al. 2021; Utzschneider et al. 2021).

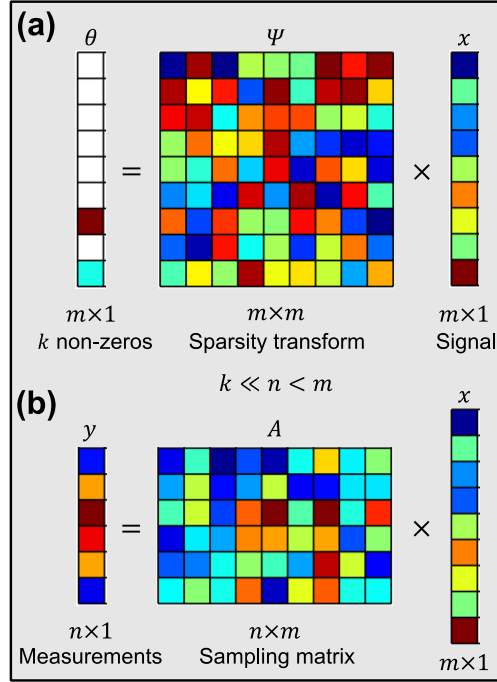


**Figure 4.15** Schematics of fundamentals of a sparse representation. **(a)** Transform sparsity produces a set of sparse transform coefficients,  $\theta$ , with  $k$  non-zero elements after a sparsifying transform,  $\Psi$ , operating on a signal,  $x$ . **(b)** An  $m \times 1$   $k$ -sparse signal can be converted to an  $n \times 1$  set of measurements,  $y$ , through an  $n \times m$  sampling matrix,  $A$ , ( $k \ll n < m$ ). The colours indicate the values of the elements in the matrices. The elements of  $\theta$  in white are zeros. **Source:** (Chen et al. 2021) with permission from John Wiley and Sons (License No. 5745420106236).

### Incoherent Undersampling

A fundamental requirement of CS is that the aliasing artefacts arising from undersampled k-space data due to violation of the Nyquist constraint are incoherent (i.e. noise-like) in the image domain. Given the fast biexponential relaxation behaviour of sodium signals, non-Cartesian UTE k-space sampling schemes are commonly employed in sodium MRI, such as 3D radial (Niellès-Vallespin et al. 2007), stacks of spirals (Mirkes et al. 2016), density-adapted 3D projection (Nagel et al. 2009), Twisted Projection Imaging (TPI) (Appendix A3) (Boada et al. 1997, 1997a), flexible TPI (Lu et al. 2010), 3D cones (Appendix A3) (Gurney et al. 2006) and FLORET (Pipe et al. 2011). Typically, k-space undersampling is performed by pseudo-

randomly skipping a subset of phase-encoded lines in a Cartesian acquisition or projections in a non-Cartesian acquisition (as shown in Figure 4.16), such as a variable-density sampling scheme (Greiser & von Kienlin 2003; Marseille et al. 1996), resulting in reduced scan times. The undersampling artefacts exhibit a noise-like pattern in the image domain and even more so in a properly chosen sparse domain. 3D non-Cartesian sampling, such as FLORET (Figure 4.16f), provides better sparsity and thus yields higher CS performance than conventional 2D Cartesian sampling characterised by incoherently undersampled phase-encodes and fully-sampled readouts (Figure 4.16a). This enables 3D non-Cartesian sampling as an outstanding candidate for CS-based acceleration (Lustig et al. 2007, 2008).

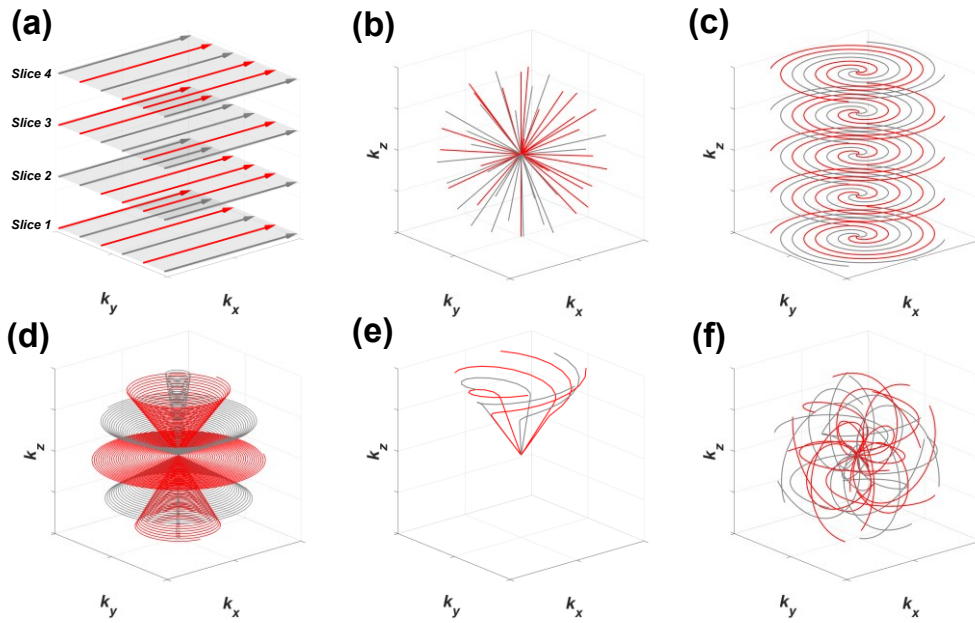


**Figure 4.16** k-space trajectories with two-fold incoherent undersampling. Grey phase-encoded lines or projections are skipped, while red ones are measured. **(a)** 2D Cartesian trajectories with pseudo-randomly undersampled phase-encoded lines and fully-sampled readouts. **(b-f)** 3D non-Cartesian UTE k-space trajectories that are often used in sodium MRI: **(b)** 3D radial, **(c)** stacks of spirals, **(d)** 3D cones, **(e)** TPI and **(f)** FLORET. **Source:** (Chen et al. 2021) with permission from John Wiley and Sons (License No. 5745420106236).

### Non-linear Iterative Reconstruction

In the case of the above undersampling, only  $n$  linear measurements ( $n < m$ ) of the unknown signal,  $x \in \mathbb{C}^m$ , with  $m$  samples, are obtained, expressed as:

$$y_i = a_i x, \quad i = 1, \dots, n \quad \text{or} \quad y = Ax, \quad (4.58)$$

where  $a_i \in \mathbb{C}^m$  is a known sampling vector in the  $i^{\text{th}}$  measurement;  $A \in \mathbb{C}^{n \times m}$  is the sampling matrix of dimension  $n \times m$ ;  $y \in \mathbb{C}^n$  is the measured dataset with  $n$  samples from  $n$  measurements by applying the sampling matrix,  $A$ . A more intuitive interpretation of this

undersampling is presented in Figure 4.15b. Of special interest is the exact recovery of signal  $x$  in the extremely undersampled situation, where the number of unknowns ( $m$ ) is much larger than the number of the observations ( $n$ ), which at first glance might seem impossible. (Candès et al. 2006c, 2006a; Candès & Tao 2005) proposed that the signal of interest,  $x$ , can be exactly recovered by solving the following  $\ell_1$ -convex problem if the sampling matrix,  $A$ , has the restricted isometry property (Candès et al. 2006a):

$$\min_x \|x\|_1 \quad \text{subject to} \quad y = Ax, \quad (4.59)$$

where the  $\ell_1$ -norm is the sum of the amplitudes of vector  $x$ . More specifically, for a given restricted isometry constant,  $\delta_{2k}$ , a sampling matrix,  $A$ , has a  $k$ -restricted isometry property if it meets the following condition for all  $k$ -sparse vectors  $x_1$  and  $x_2$  for  $\mathbb{C}^m$ :

$$(1 - \delta_{2k})\|x_1 - x_2\|_2^2 \leq \|Ax_1 - Ax_2\|_2^2 \leq (1 + \delta_{2k})\|x_1 - x_2\|_2^2. \quad (4.60)$$

There is a high probability of satisfying this condition if the undersampling scheme is incoherent and if the amount of measurements is larger than a given constant that is determined from the number of samples,  $m$ , and the sparsity value,  $k$  (Candès & Tao 2005).

In clinical routine, the signal  $x$  is usually transformed onto a specific domain to enhance its sparsity as much as possible, thereby decreasing the number of unknowns to achieve near-optimal image reconstruction, as shown in the unconstrained formula adapted from Eq. (4.59):

$$\hat{x} = \arg \min_x \{ \|\Psi x\|_1 + \lambda \|y - Ax\|_2^2 \}, \quad (4.61)$$

where  $x$  is the iteratively reconstructed image;  $\hat{x}$  is the final reconstructed image;  $y$  is the acquired k-space raw data;  $A$  is the Fourier transform operator;  $\Psi$  is the sparsifying transform operator that makes  $\Psi x$  sparse; and  $\lambda$  is a regularisation parameter to balance the  $\ell_1$ -norm (i.e. the sum of the absolute values of the vector) and  $\ell_2$ -norm (i.e. the square root of the sum of the squared vector values). Minimising the  $\ell_1$ -norm improves sparsity, whereas the  $\ell_2$ -norm constraint ensures data consistency. In other words, among all potential solutions consistent with the measured data,  $y$ , Eq. (4.61) finds one that is compressible with transform  $\Psi$ . Furthermore, the Total Variation (TV) norm (i.e. the  $\ell_1$ -norm of the variations of neighbouring pixels or voxels) can facilitate image restoration since the finite difference operator acts as an edge-preserving filter to smooth regions with constant intensity (Rudin et al. 1992). Therefore, to enforce the image sparsity in both the transform domain and the finite-difference domain, a TV penalty is added to Eq. (4.61), as follows:

$$\hat{x} = \arg \min_x \{ \alpha \text{TV}(x) + \|\Psi x\|_1 + \lambda \|y - Ax\|_2^2 \}, \quad (4.62)$$

where  $\alpha$  is the weighing factor for the TV penalty.

#### 4.4.4 Reconstruction Performance Evaluation

Researchers face a crucial hurdle – the difficulty of evaluating CS reconstruction performance since the true assessment of a reconstruction relies on the diagnostic value of resulting images, which clearly cannot be known in a development cycle. Therefore, the quantitative and qualitative methods and statistical analysis mentioned below are often used as proxies.

The quantitative method calculates image metrics by comparing resulting images with ground truth images acquired from fully-sampled k-space data by using the standard NUFFT algorithm. Common image metrics include Structural SIMilarity (SSIM) in terms of degradation of structural information (Adlung et al. 2021; Behl et al. 2016; Blunck et al. 2019; Lachner et al. 2019; Lachner, Ruck, et al. 2020; Wang et al. 2004), normalised root-mean-square error for measuring numerical similarity (Lachner, et al. 2020; Utzschneider et al. 2020, 2021; Weingärtner et al. 2015), SNR difference to ground truth (Adlung et al. 2021; Gnahn et al. 2014; Gnahn & Nagel 2015; Madelin et al. 2012; Zhao et al. 2021) and peak SNR (Behl et al. 2016). Moreover, quantitative sodium MRI provides Total Sodium Concentration that is linked to cellular integrity and tissue viability (Boada et al. 2005; Madelin et al. 2014; Thulborn et al. 2009; Winkler 1990). Accordingly, the error of TSC to the ground truth can be set as an image metric unique to sodium MRI techniques (Adlung et al. 2021; Utzschneider et al. 2021).

However, for the clinical establishment of an advanced reconstruction technique, its ability to show specific pathologies and anatomical structures is more critical to radiologists than mathematical matching to a ground truth that might still be flawed. Thus, a qualitative assessment is recommended in clinical studies with blinded image quality grading by multiple radiologists (Sandino et al. 2020). Image quality can be assessed against a set of criteria, including overall image quality, residual artefacts, sharpness, image contrast, perceived SNR and diagnostic confidence, with specifically defined scores ranging from 1 (non-diagnostic) to 5 (excellent) (Adlung et al. 2021; Chen et al. 2018; Sandino et al. 2020). However, even this is only a proxy for a true assessment of diagnostic accuracy in clinical practice.

Suppose the number of consecutive scans is meaningful in statistics (typically greater than 20). In this case, statistical analysis can be performed to show the differences between two sets of images or two reconstruction approaches (Madelin et al. 2018). Since image metrics (such as

TSC error and SSIM) regarding ground truth generally follow a normal distribution, a paired Student's t-test can be applied to assess the statistical significance of image metrics from two reconstruction techniques (Adlung et al. 2021). The difference in image quality scores between two sets of images can be statistically evaluated by a non-parametric statistical test, e.g. a Wilcoxon test, which can check whether the scores of two different reconstructions originate from the same distribution (Sandino et al. 2020). Ideally, a CS-based reconstruction for undersampled k-space data should yield results from the same distribution as the ground truth images.



# **DEVELOPMENT AND IMPLEMENTATION**

MQF SODIUM MRI: INVESTIGATION OF DATA  
ACQUISITION AND IMAGE RECONSTRUCTION



## 5 Multiple-Quantum-Filtered Sodium MRI at 7T: Optimisation of the Enhanced SISTINA Sequence Using FLORET K-space Trajectories

### *Data Acquisition*

#### **Abstract**

**Purpose** Multiple-Quantum-Filtered sodium Magnetic Resonance Imaging, such as enhanced Simultaneous Single-quantum and Triple-quantum-filtered imaging of  $^{23}\text{Na}$ , enables images to be weighted towards restricted sodium – a promising biomarker in clinical practice. However, MQF sodium MRI suffers from clinically infeasible measurement times and low image quality. This work aims to optimise the enhanced SISTINA sequence to promote its potential for image quality improvement and imaging acceleration.

**Method** The conventional enhanced SISTINA sequence with Three-Dimensional radial Ultra-short Echo Time readouts and 3D Cartesian MQF readouts was optimised at 7T using Fermat Looped, Orthogonally Enhanced Trajectories k-space trajectories with high k-space filling efficiency and good undersampling potential. The 3D radial (Cartesian) scheme was replaced with a dense (sparse) 3D FLORET scheme for UTE (MQF) acquisitions. A qualitative comparison of image quality between the conventional and optimised enhanced SISTINA was conducted in three phantom measurements.

**Result** The sequence optimisation using FLORET k-space trajectories greatly improved the visual quality of UTE images, while maintaining the visual performance of MQF images. Furthermore, it introduced incoherence to the MQF raw data, which satisfied one of the requirements for applying Compressed Sensing to accelerate enhanced SISTINA.

**Conclusion** Successful implementation of an optimised enhanced SISTINA sequence with an incoherent sampling scheme at 7T was demonstrated. This sequence optimisation improved/maintained the visual quality of images and met the prerequisite for applying CS techniques to enhanced SISTINA for faster acquisition in future.

Part of the work presented in this chapter was published in: **Chen Q.**, Worthoff W. A., Shah N. J.: Triple-Quantum-Filtered Sodium MRI at 7T: Optimization of the Enhanced SISTINA Sequence Using FLORET k-space Trajectories. Proc. 29th Annu. Meet. ISMRM (2021).

### **5.1 Introduction**

Sodium ( $^{23}\text{Na}$ ) plays a key role in cellular metabolism via the regulation of the intracellular and extracellular sodium concentration gradient (Madelin et al. 2014; Rose & Valdes 1994). The increased intracellular sodium caused by abnormal sodium ion homeostasis is often considered a sensitive early indicator of various pathological conditions (Madelin et al. 2014). Multiple-Quantum-Filtered sodium Magnetic Resonance Imaging was proposed as a non-invasive tool

to study the in vivo pathological processes at the cellular level by monitoring the restricted (mostly intracellular)-weighted sodium content (Choi et al. 2020; Jaccard et al. 1986; Rooney & Springer 1991; Shymanskaya et al. 2020; Worthoff et al. 2020). However, MQF sodium MRI still needs to improve on the interrelated issues of relatively low image quality and long measurement times (often more than 10 minutes). Simultaneous Single-quantum and Triple-quantum-filtered imaging of  $^{23}\text{Na}$  is a delicate MQF sodium MRI technique that can simultaneously acquire Single-Quantum and Triple-Quantum coherence signals from sodium nuclei (Figure 3.7) as well as total sodium-weighted signal (Fiege et al. 2013). This work aims to optimise the conventional enhanced SISTINA (Worthoff et al. 2019) sequence by employing the highly efficient incoherent FLORET (Section 4.3.2) sampling scheme, thus promoting its potential for image quality improvement and imaging acceleration.

## 5.2 Materials and Methods

### 5.2.1 Multiple-Quantum Filter

A multiple-quantum filter with a twelve-step phase cycling scheme (Worthoff et al. 2019) was employed in the enhanced SISTINA sequence. The filter consists of three RF hard pulses with flip angles of  $\theta_1 = \theta_2 = \theta_3 = \pi/2$ , as shown in Figure 5.1.

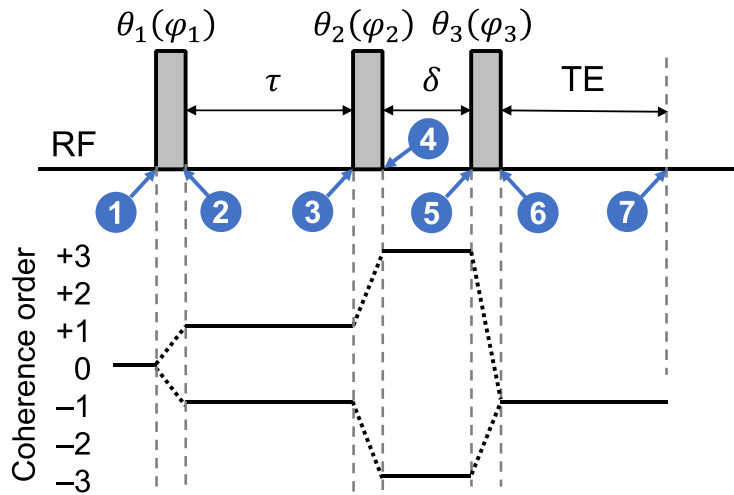


**Figure 5.1** Multiple-quantum filter of the enhanced SISTINA sequence. The filter consists of three  $\pi/2$ -RF hard pulses with an application of a twelve-step phase cycling scheme. The diagram shows two possible coherence transfer pathways to yield signals from TQ coherences. Here,  $\tau$  is the preparation time, and  $\delta$  is the evolution time. Time points are indicated by numbers within blue circles.

The diagram in Figure 5.1 shows two possible coherence transfer pathways for signals originating from TQ coherences. The evolution of the density matrix in terms of spherical tensor operators along the TQ pathways is described step-by-step as follows.

1. Before  $t_1$ , i.e. before any RF pulses is applied, the spin system is in equilibrium with a density operator of  $T_{10}$ .
2. From  $t_1$  to  $t_2$ , the first RF pulse  $\theta_1(\varphi_1)$  converts  $T_{10}$  to transverse magnetisation  $T_{1\pm 1}$ :

$$T_{10} \xrightarrow{\theta_1(\varphi_1)} -\frac{i}{\sqrt{2}}(T_{1+1}e^{i\varphi_1} + T_{1-1}e^{-i\varphi_1}). \quad (5.1)$$

3. From  $t_2$  to  $t_3$ , i.e. between the first and second RF pulses, the rank-1 SQ coherence,  $T_{11}$ , evolves and partially transforms into the rank-2 and rank-3 SQ coherences:

$$T_{11} \xrightarrow{\tau} f_{11}^1(\tau)T_{11} + f_{21}^1(\tau)T_{21} + f_{31}^1(\tau)T_{31}. \quad (5.2)$$

4. From  $t_3$  to  $t_4$ , the second RF pulse converts the rank-3 SQ coherence,  $T_{31}$ , into the TQ coherence,  $T_{33}$ :

$$T_{31} \xrightarrow{\theta_2(\varphi_2)} -\frac{1}{4}T_{31} + \frac{\sqrt{15}}{4}T_{33}. \quad (5.3)$$

However, the rank-1 and rank-2 SQ coherences ( $T_{11}$  and  $T_{21}$ ) are not affected by the second RF pulse, because there is a phase shift of  $\pi/2$  between the first and second RF pulses.

5. From  $t_4$  to  $t_5$ , i.e. between the second and third RF pulses, neither the coherence order nor the rank is changed:

$$T_{33} \xrightarrow{\delta} f_{33}^3(\delta)T_{33}. \quad (5.4)$$

As only the rank-1 SQ coherences,  $T_{11}$ , can be detected, a third RF pulse is required to convert the rank-3 TQ coherence,  $T_{33}$ , back to the rank-3 SQ coherence,  $T_{31}$ , that evolves into the detectable SQ coherence,  $T_{11}$ , during the Echo Time.

6. From  $t_5$  to  $t_6$ , the third RF pulse converts the rank-3 TQ coherence,  $T_{33}$ , to the rank-3 SQ coherence,  $T_{31}$ :

$$T_{33} \xrightarrow{\theta_3(\varphi_3)} \frac{1}{4}T_{33} + \frac{\sqrt{15}}{4}T_{31}. \quad (5.5)$$

7. From  $t_6$  to  $t_7$ , i.e. during TE, the final detectable signal is generated:

$$T_{31} \xrightarrow{TE} f_{13}^1(TE)T_{11} + f_{23}^1(TE)T_{21} + f_{33}^1(TE)T_{31}. \quad (5.6)$$

Therefore, the final TQ-filtered signal is  $S_{\text{TQF}} \propto \frac{15}{16} f_{31}^1(\tau) f_{33}^2(\delta) f_{33}^1(TE)$ , where  $f_{31}^1(\cdot)$ ,  $f_{33}^2(\cdot)$  and  $f_{33}^1(\cdot)$  are scaling factors relative to the quadrupolar frequency and the fast and slow transverse relaxation rates (Benkhedah et al. 2013).

Similarly, there are seven possible pathways for signals originating from SQ coherences, listed in Table 5.1.

**Table 5.1** Seven SQ coherence pathways.

$S_{\text{SQF}}$	Equilibrium	$\theta_1(\varphi_1)$	$\tau$	$\theta_2(\varphi_2)$	$\delta$	$\theta_3(\varphi_3)$	$TE$
$f_{11}^1(\tau) f_{11}^1(\delta) f_{11}^1(TE)$	$T_{10}$	$T_{11}$	$T_{11}$	$T_{11}$	$T_{11}$	$T_{11}$	$T_{11}$
$-\frac{1}{4} f_{11}^1(\tau) f_{31}^1(\delta) f_{31}^1(TE)$	$T_{10}$	$T_{11}$	$T_{11}$	$T_{11}$	$T_{31}$	$T_{31}$	$T_{11}$
$-\frac{1}{16} f_{31}^1(\tau) f_{33}^1(\delta) f_{31}^1(TE)$	$T_{10}$	$T_{11}$	$T_{31}$	$T_{31}$	$T_{31}$	$T_{31}$	$T_{11}$
$-\frac{1}{4} f_{31}^1(\tau) f_{31}^1(\delta) f_{11}^1(TE)$	$T_{10}$	$T_{11}$	$T_{31}$	$T_{31}$	$T_{11}$	$T_{11}$	$T_{11}$
$-f_{11}^1(\tau) f_{21}^1(\delta) f_{21}^1(TE)$	$T_{10}$	$T_{11}$	$T_{11}$	$T_{11}$	$T_{21}$	$T_{21}$	$T_{11}$
$f_{21}^1(\tau) f_{22}^1(\delta) f_{21}^1(TE)$	$T_{10}$	$T_{11}$	$T_{21}$	$T_{21}$	$T_{21}$	$T_{21}$	$T_{11}$
$-f_{21}^1(\tau) f_{22}^1(\delta) f_{11}^1(TE)$	$T_{10}$	$T_{11}$	$T_{21}$	$T_{21}$	$T_{11}$	$T_{11}$	$T_{11}$

A twelve-step phase cycling scheme is applied in this filter to separate signals originating from SQ coherences and TQ coherences (Worthoff et al. 2019): the first RF phase,  $\varphi_1 = \left\{ \frac{\pi}{6}, \frac{\pi}{2}, \frac{5\pi}{6}, \frac{7\pi}{6}, \frac{3\pi}{2}, \frac{11\pi}{6}, \frac{7\pi}{6}, \frac{3\pi}{2}, \frac{11\pi}{6}, \frac{\pi}{6}, \frac{\pi}{2}, \frac{5\pi}{6} \right\}$ , the second RF phase,  $\varphi_2 = \varphi_1 + \frac{\pi}{2}$ , the third RF phase,  $\varphi_3 = 0$  and the receiver phase,  $\varphi_{\text{rec}} = \{0, \pi, 0, \pi, 0, \pi, 0, \pi, 0, \pi, 0, \pi\}$ . The numerical phase used for filtering TQ signal is  $\varphi_{\text{TQ, num}} = \{0, 0, 0, 0, 0, 0, \pi, \pi, \pi, \pi, \pi, \pi\}$ . The numerical phase for filtering SQ signal with coherence order of +1 after the second RF pulse is  $\varphi_{\text{SQ\_p1, num}} = \left\{ -\frac{7\pi}{6}, -\frac{5\pi}{2}, -\frac{11\pi}{6}, -\frac{19\pi}{6}, -\frac{5\pi}{2}, -\frac{23\pi}{6}, -\frac{13\pi}{6}, -\frac{7\pi}{2}, -\frac{17\pi}{6}, -\frac{25\pi}{6}, -\frac{7\pi}{2}, -\frac{29\pi}{6} \right\}$ . The numerical phase for filtering SQ signal with coherence order of -1 after the second RF pulse is  $\varphi_{\text{SQ\_n1, num}} = \left\{ \frac{2\pi}{3}, 0, \frac{4\pi}{3}, \frac{2\pi}{3}, 0, \frac{4\pi}{3}, \frac{5\pi}{3}, \pi, \frac{7\pi}{3}, \frac{5\pi}{3}, \pi, \frac{7\pi}{3} \right\}$ . These two filtered SQ signals were summed in post-processing to form the final SQ signal.

### 5.2.2 Enhanced SISTINA Sequence Implementation

A conventional enhanced SISTINA sequence with two readout trains (Figure 5.2a) was implemented based on the multiple-quantum filter described in Section 5.2.1.

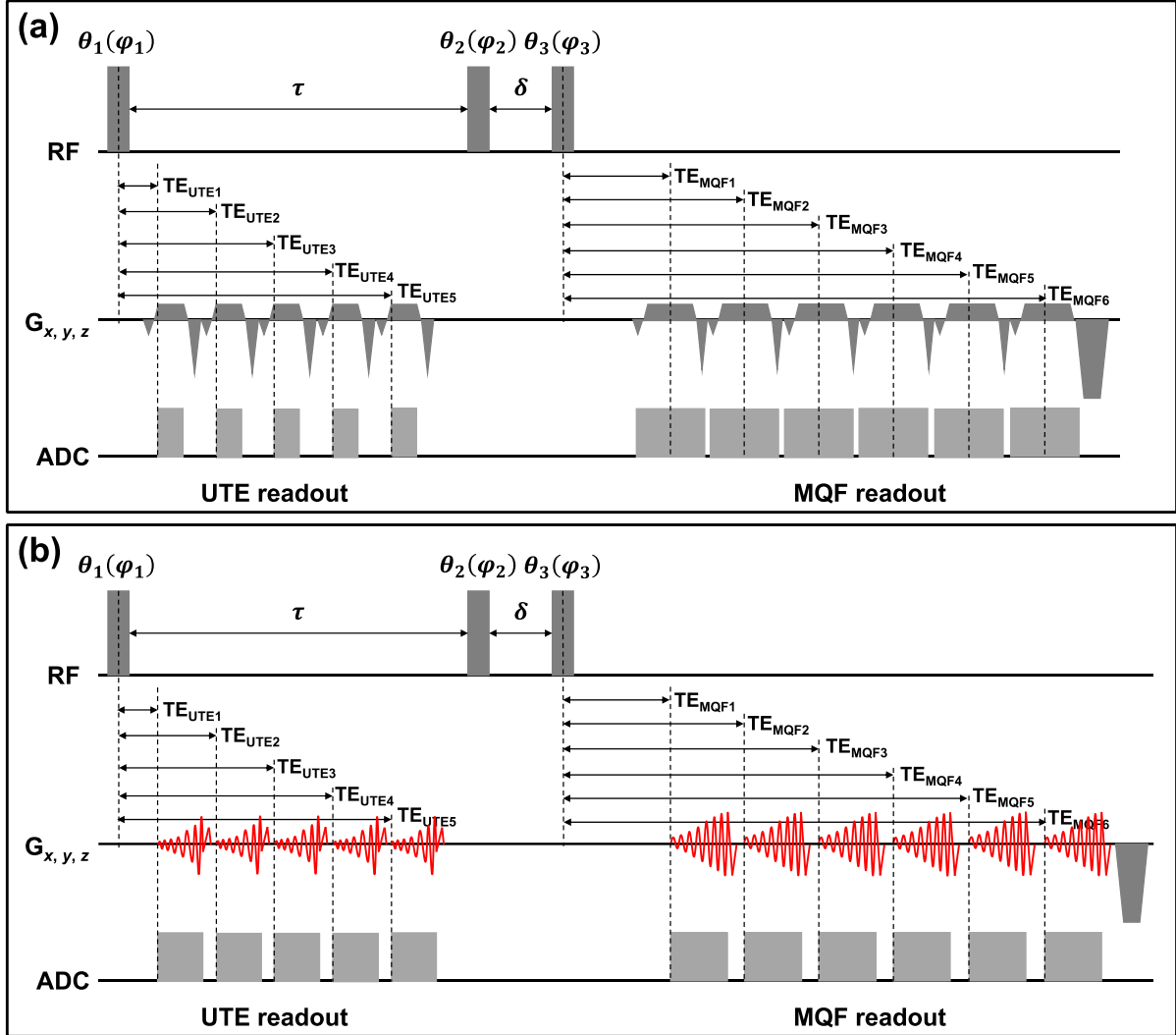


**Figure 5.2** Diagrams of enhanced SISTINA sequences. **(a)** Conventional enhanced SISTINA sequence with DISCOBALL UTE and MGRE MQF readouts. **(b)** Optimised enhanced SISTINA sequence with FLORET UTE and FLORET MQF readouts. **Source:** (Chen et al. 2021).

As shown in Figure 5.2a, the multiple-quantum filter consists of three  $\pi/2$ -hard pulses separated by a preparation time of  $\tau = 10$  ms and an evolution time of  $\delta = 50$   $\mu$ s. During the preparation time, a five-echo Three-Dimensional-radial Direction Scheme Obtained By Aligning points on Latitudes (DISCOBALL) (Figure 5.3a) UTE readout train delivers information on total sodium distribution. After the third RF pulse, a multi-echo gradient echo (MGRE) MQF readout train provides information on multiple quantum coherences. The gradient moment is completely rewound after each readout to mitigate the interference of residual magnetisation

on SQ and TQ coherences. Furthermore, after the last MQF readout, a strong gradient is applied to spoil the residual transverse magnetisation.

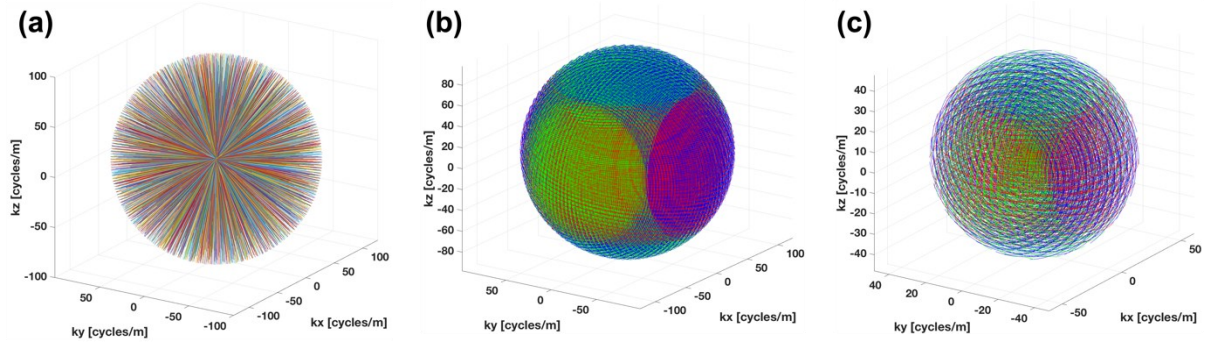


**Figure 5.3** k-space trajectories of enhanced SISTINA. **(a)** DISCOBALL trajectories (4452 projections) for UTE readouts of conventional enhanced SISTINA in the first measurement. FLORET trajectories for **(b)** UTE readouts (4464 projections) and **(c)** MQF readouts (372 projections) of the optimised enhanced SISTINA in the third measurement. *Source:* (Chen et al. 2021).

The conventional enhanced SISTINA sequence was optimised by employing two sets of 3D spiral-based FLORET k-space trajectories (Figure 5.2b). The FLORET trajectories were calculated and implemented based on the user-defined parameters of maximum slew rate, maximum gradient strength, Field-Of-View, resolution and the number of projections, aiming to improve the quality of UTE images and introduce high incoherence to SQ and TQ raw data. The FLROET with 4464 projections (Figure 5.3b) was used to replace the 3D-radial DISCOBALL, and the FLORET with 372 projections (Figure 5.3c) was employed as the 3D-Cartesian MGRE. The sequence parameters for the conventional and optimised enhanced SISTINA are listed in Table 5.2.



**Table 5.2** Enhanced SISTINA sequence parameters for three measurements (repetition time = 213.5 ms, total acquisition time = ~16 min). FWHM: full width at half maximum of the point spread function, calculated using the MIRT toolbox. *Source:* (Chen et al. 2021).

Measure ment	Readout module	TE (ms)	Bandwidth (Hz/pixel)	Voxel size (mm <sup>3</sup> )	FOV (mm <sup>3</sup> )	Sampling scheme	FWHM (mm)	Total projection
<b>1</b>	UTE	0.37, 2.27, 4.17, 6.07, 7.97	1000	5 iso	320 iso	DISCOBALL	10.3	4452
	MQF	10.0, 19.13, 28.26, 37.39, 46.52, 55.65	120	10 iso	320 × 240 × 200	MGRE		
<b>2</b>	UTE	0.36, 2.26, 4.16, 6.06, 7.96	840	5 iso	320 iso	FLORET	6.8	4452
	MQF	10.0, 19.13, 28.26, 37.39, 46.52, 55.65	120	10 iso	320 × 240 × 200	MGRE		
<b>3</b>	UTE	0.36, 2.26, 4.16, 6.06, 7.96	840	5 iso	320 iso	FLORET	6.8	4464
	MQF	10.0, 13.2, 16.4, 19.6, 22.8, 26.0	375	10 iso	320 iso	FLORET	14.0	372

### 5.2.3 Data Acquisition

All MRI images were acquired on a Siemens 7T Terra scanner (SIEMENS Healthineers, Erlangen, Germany) with a maximum gradient of 80 mT/m and a maximum slew rate of 200 mT/(m\*ms). Agarose phantoms (Figure 5.4) were scanned for the validation of the conventional and optimised enhanced SISTINA sequences using a dual-tuned single-channel <sup>1</sup>H/<sup>23</sup>Na transmit-receive birdcage coil (RAPID Biomedical, Germany). This phantom consists of multiple tubes with various sodium chloride concentrations in mmol/L and agarose weights per deionised water volume in percent for the simulation of less-restricted (2% and 3% agarose) and restricted (6% and 10% agarose) environments. Three measurements were conducted to evaluate the performance of enhanced SISTINA with different implementations of k-space trajectories. The sequence parameters for these three measurements are listed in Table 5.2. A conventional enhanced SISTINA (Figure 5.2a) with 3D-radial DISCOBALL (Figure 5.3a) UTE readouts and MGRE MQF readouts was performed in the first measurement, and DISCOBALL was replaced by 3D-spiral FLORET in the subsequent measurement. In the last measurement, both DISCOBALL and MGRE were replaced by FLORET (Figure 5.2a). The FLORET k-space trajectories for UTE and MQF readouts are shown in Figure 5.3b and Figure 5.3c, respectively. Non-Cartesian UTE, SQ and TQ raw data were reconstructed using Jeff

Fessler's Michigan Image Reconstruction Toolbox (MIRT) (Fessler & Sutton 2003).  $B_0$  mapping was performed with a dual-echo 3D spoiled gradient-echo sequence, and flip-angle maps were obtained using a phase-sensitive  $B_1$  mapping sequence (Allen et al. 2011; Morrell 2008) with a gradient-echo readout.  $B_0$  and  $B_1$  maps with a resolution of 10 mm cubic were acquired to correct SQ and TQ images and were gridded to 5 mm cubic to correct UTE images in post-processing (Worthoff et al. 2019).

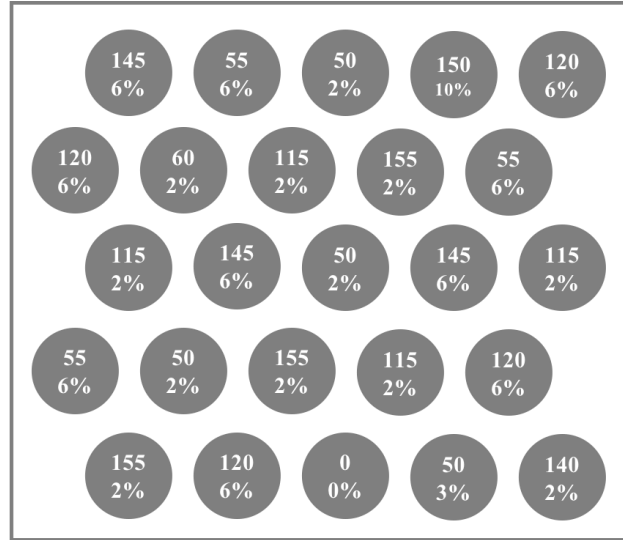


**Figure 5.4** Agarose phantoms. The schematic presents sodium concentrations in mmol/L and agarose concentrations in percent (e.g. 2% indicates 2 grams of agarose powder per 100 ml of deionised water). The 2% and 3% agarose phantoms simulate the less-restricted environment, whereas the 6% and 10% agarose phantoms mimic the restricted environment. **Source:** (Chen et al. 2021).

### 5.3 Results

Figure 5.5 shows the first-echo UTE, SQ and TQ images after  $B_0$  and  $B_1$  field correction (Worthoff et al. 2019) from the abovementioned three measurements. As can be observed in all measurements, UTE images exhibit higher signal intensity in phantoms with higher sodium concentrations (e.g. 145 mmol/L) regardless of the agarose concentration, indicating UTE images are weighted towards total sodium. SQ images are weighted towards less-restricted sodium (2% and 3% agarose) since the restricted sodium (6% and 10% agarose) is more likely to evolve from SQ into TQ coherences through the excitation of the multiple-quantum filter. As expected, the 2% agarose phantoms show much higher SQ signal intensity than the 6% and 10% agarose phantoms at similar sodium concentrations. In contrast, the TQ images are weighted towards restricted sodium. As expected, the 6% agarose phantoms with a sodium concentration of 145 mmol/L present high TQ signal intensity, whereas the TQ signal from 2% and 3% agarose phantoms is well-suppressed. The signal intensity of the 10% agarose phantom

in the TQ image might be degraded by the fast  $T_2^*$  relaxation but is still higher than that in the SQ image. The above observations suggest that the employment of FLORET sampling schemes does not affect the quantum mechanics of the enhanced SISTINA sequence.

Compared with the first measurement (Figure 5.5a), the replacement of DISCOBALL UTE readouts (Full Width at Half Maximum of Point Spread Function = 10.3mm) with FLORET (FWHM = 6.8mm) in the second measurement (Figure 5.5b) effectively reduces the image blurring and promotes the visual performance of the UTE image (Figure 5.5b left) without introducing noticeable difference to the SQ and TQ images (Figure 5.5d middle and right).

In the last measurement (Figure 5.5c), the substitution of FLORET for MGRE MQF readouts has little effect on the UTE images, given the noise-like UTE image difference between the second and third measurements (Figure 5.5d left). Furthermore, SQ and TQ images obtained from FLORET MQF readouts agree well with those from MGRE MQF readouts. This indicates that the non-Cartesian sampling and reconstruction do not significantly affect the visual performance of MQF images obtained from FLORET readouts. More importantly, the non-Cartesian MQF sampling introduces incoherence to SQ and TQ raw data, which satisfies one of the requirements for applying CS for scan acceleration.

## 5.4 Discussion

Motivated by the fact that the clinical application of MQF sodium MRI is hindered by long measurement times and low image quality, this work implements a novel enhanced SISTINA sequence with an incoherent sampling scheme at 7T and demonstrates that the novel enhanced SISTINA has better visual performance than the conventional enhanced SISTINA in a phantom study. The contrasts of UTE, SQ and TQ images remained unchanged across the three measurements. This suggests that modifications to the UTE and MQF sampling schemes have little impact on the functionality of the enhanced SISTINA sequence. The employment of FLORET to replace DISCOBALL in the UTE readouts can greatly improve UTE image quality without significantly affecting MQF data acquisition.

Furthermore, the introduction of FLORET as an alternative to 3D-Cartesian MGRE in the MQF readouts can maintain the performance of SQ and TQ images while preserving the quality of UTE images from visual inspection. Moreover, it introduces an incoherent pattern to the SQ and TQ raw data, which is required by the CS acceleration.

The ultra-high field system can offer a higher SNR for MRI images. The optimised enhanced SISTINA sequence has excellent potential for the simultaneous acquisition of higher-quality UTE, SQ and TQ images in an accelerated scan at 7T by using CS reconstruction, thereby promoting its applicability in scientific research and clinical practice.

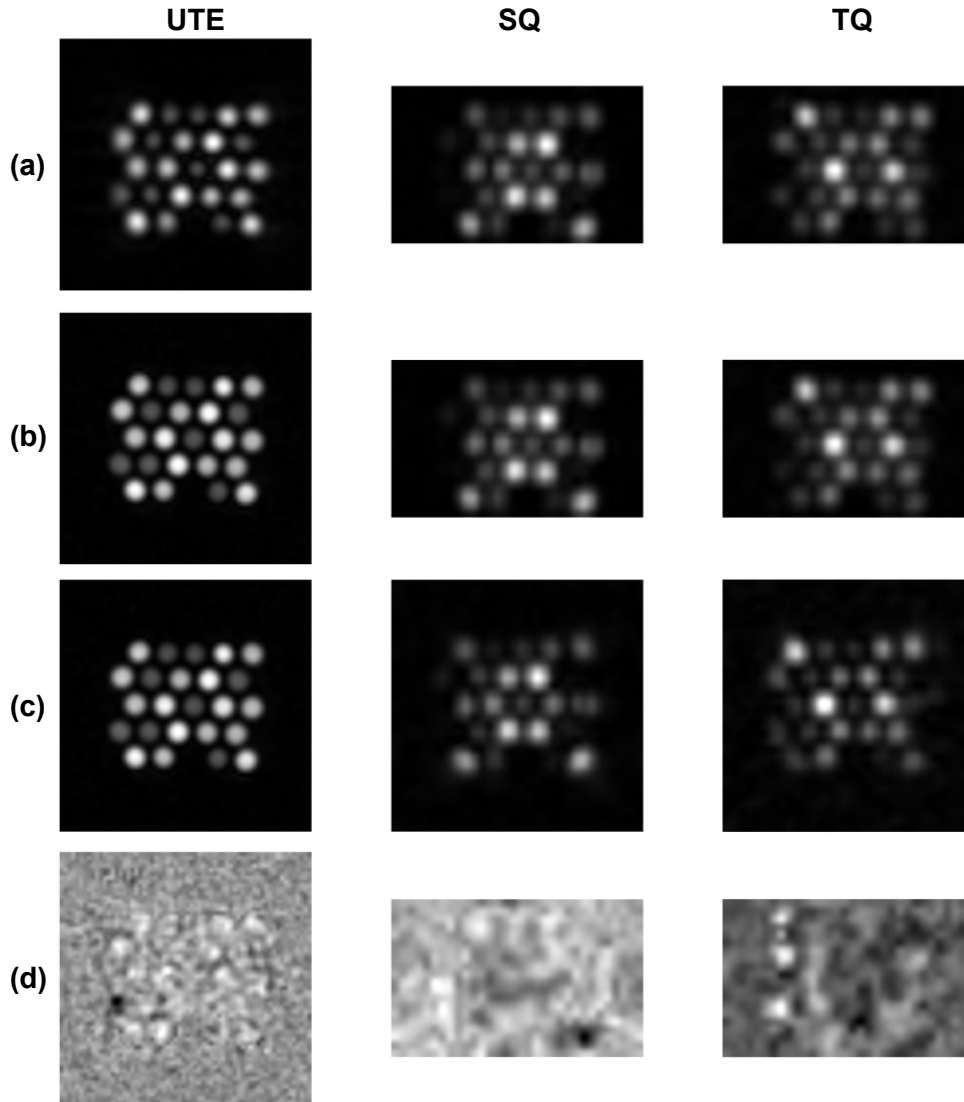


**Figure 5.5** The first-echo UTE, SQ and TQ images after B0 and B1 correction obtained from three measurements described in Table 5.2. *Source:* (Chen et al. 2021).

## 5.5 Conclusion

Successful implementation of an optimised enhanced SISTINA sequence with an incoherent sampling scheme at 7T was demonstrated in this study. The optimised enhanced SISTINA generally has better performance than the conventional enhanced SISTINA. This sequence optimisation satisfies the prerequisite for future application of CS reconstruction to accelerate MQF sodium MRI (Chapter 6).

## 6 Accelerated Enhanced Simultaneous Single-Quantum and Triple-Quantum-Filtered Sodium Magnetic Resonance Imaging Using Compressed Sensing at 7T

### *Image Reconstruction*

#### **Abstract**

**Purpose** Enhanced Simultaneous Single-quantum and Triple-quantum-filtered imaging of  $^{23}\text{Na}$  enables images to be weighted towards restricted sodium – a sensitive biomarker for metabolic cellular dysfunction. However, enhanced SISTINA often suffers from low image quality and associated clinically infeasible acquisition times. This study aims to alleviate the above limitation by applying Compressed Sensing to accelerate enhanced SISTINA acquisitions at 7T without a noticeable loss of information.

**Methods** Fully sampled data were acquired from one phantom and ten healthy subjects at 7T using an optimised enhanced SISTINA sequence with a Three-Dimensional spiral-based sampling scheme. The fully sampled data were then retrospectively undersampled by various undersampling factors. Quantitative evaluation was performed by comparing undersampled CS reconstructions to fully sampled and undersampled Non-Uniform Fast Fourier Transform reconstructions. Reconstruction performance was assessed using Signal-to-Noise Ratio, Structural SIMilarity, weightings towards total and compartmental sodium and in vivo quantitative estimates.

**Results** CS-based images have lower noise levels and better structural delineation, while maintaining the weightings towards total, non-restricted (mainly extracellular) and restricted (mainly intracellular) sodium. CS generally performs better than NUFFT, with higher SNR and greater SSIM, except for the SSIM in TQ brain images, which may be due to massive noise contamination. With an undersampling factor of up to two, CS enables relatively reliable in vivo quantitative estimates with less than 15% errors.

**Conclusions** Compared with NUFFT, CS can accelerate enhanced SISTINA by up to twofold at 7T with reduced noise levels, while maintaining primary structural information, reasonable weightings towards total and compartmental sodium and relatively accurate in vivo quantification. The associated acquisition time reduction has the potential to promote the applicability of enhanced SISTINA in clinical practice.

The work presented in this chapter mainly comes from: **Chen Q.,\*** Worthoff W. A.,\* Shah N. J.: Accelerated Multiple-Quantum-Filtered Sodium Magnetic Resonance Imaging Using Compressed Sensing at 7T. *Magn. Reson. Imaging* (2024) 1–22.

### **6.1 Introduction**

Chapter 5 applied enhanced Simultaneous Single-quantum and Triple-quantum-filtered imaging of  $^{23}\text{Na}$  technique for restricted (mostly intracellular) sodium-weighted imaging,

indicating its potential of non-invasive investigation on in vivo pathological processes at the cellular level (Choi et al. 2020; Jaccard et al. 1986; Rooney & Springer 1991; Shymanskaya et al. 2020; Worthoff et al. 2020). However, the clinical application of enhanced SISTINA is hindered by the interrelated issues of relatively low image quality and long acquisition times (often more than ten minutes) due to multiple factors (Chapter 5). Compressed Sensing (Session 4.4.3) has been shown to speed up sodium Magnetic Resonance Imaging and improve the quality of sodium images in various studies (Chen et al. 2022). Since the applicability of CS in sodium MRI was first demonstrated in 2012 (Madelin et al. 2012), it has been utilised to improve sodium MRI on various anatomical regions, including the human knee (Madelin et al. 2012), brain (Adlung et al. 2021; Behl et al. 2016; Blunck et al. 2019; Gnahn et al. 2014; Gnahn & Nagel 2015; Kratzer et al. 2020, 2021; Weingärtner et al. 2015; Zhao et al. 2021), breast (Lachner et al. 2019, 2020), skeletal muscle (Utzschneider et al. 2020, 2021) and human torso (Platt et al. 2018). Furthermore, its clinical potential has been preliminarily demonstrated in several pathological conditions, such as ischemic stroke (Adlung et al. 2021; Weingärtner et al. 2015), multiple sclerosis (Gnahn & Nagel 2015) and brain tumours (Regnery et al. 2020; Zhao et al. 2021). However, these studies have only sped up conventional total sodium-weighted imaging. Intracellular sodium-weighted images are less compressible than total sodium-weighted images due to high noise contamination and low image resolution. CS acceleration of intracellular sodium-weighted imaging, which may provide greater clinical implications, has not been studied. This proof-of-concept study investigated the feasibility of using CS to accelerate enhanced SISTINA acquisitions (Fiege et al. 2013; Worthoff et al. 2019) at 7T. The optimised enhanced SISTINA sequence introduced in Chapter 5 was used for data acquisition (Chen et al. 2021). Fully sampled enhanced SISTINA data were first obtained from a phantom and ten healthy subjects and then retrospectively undersampled over various UnderSampling Factors (USFs). Finally, CS-based images were compared with fully sampled and undersampled images reconstructed using Non-Uniform Fast Fourier Transform to assess the impact of CS on image quality, weightings towards total and compartmental sodium, as well as in vivo quantitative estimates.

## 6.2 Materials and Methods

### 6.2.1 Optimised Enhanced SISTINA Sequence

The optimised sequence for enhanced SISTINA acquisitions (Chen et al. 2021) is schematically shown in Figure 5.2b. This sequence employs two sets of Three-Dimensional spiral-based

FLORET k-space trajectories, introducing high incoherence into UTE, SQ and TQ raw data for CS reconstruction. The sequence has a Repetition Time of 150 ms and a total acquisition time of 11 min 10 s. The multiple-quantum filter in this sequence consists of three hard RF pulses separated by a preparation time of  $\tau = 9.5$  ms and an evolution time of  $\delta = 60$   $\mu$ s. The flip angles are  $\theta_1 = \theta_2 = \theta_3 = 90^\circ$  and the RF phases are  $\varphi_1$ ,  $\varphi_2$  and  $\varphi_3$  with the application of an appropriate twelve-step phase cycling scheme (Worthoff et al. 2019). Table 6.1 lists the parameters of the optimised enhanced SISTINA sequence.

**Table 6.1** Sequence parameters of the optimised enhanced SISTINA. TE = echo time; FOV = field-of-view; FWHM = full width at half maximum; UTE = ultra-short echo time; MQF = multiple-quantum-filtered; Voxel size = nominal resolution of the reconstructed image.

Readout module	TE (msec)	Bandwidth (Hz/pixel)	Voxel size (mm <sup>3</sup> )	FOV (mm <sup>3</sup> )	FWHM (mm)	Total projection	Average
UTE	0.56, 2.41, 4.26, 6.11, 7.96	840	5 cubic	320 cubic	6.8	4464	1
MQF	10.50, 19.63, 28.76, 37.89, 47.02, 56.15	130	10 cubic	320 cubic	13.7	372	12

### 6.2.2 Data Acquisition

All MRI raw data were acquired on a Siemens 7T Terra scanner (SIEMENS Healthineers, Erlangen, Germany) with an 80 mT/m maximum gradient amplitude and a 200 mT/m/ms maximum slew rate. A single-channel transmit-receive dual-tuned  $^1\text{H}/^{23}\text{Na}$  RF coil (RAPID Biomedical, Germany) was utilised for both hydrogen and sodium imaging. A cylindrical phantom (radius = 9 cm, height = 14 cm) (Figure 6.2a) was scanned to validate the optimised enhanced SISTINA sequence. This phantom comprises six compartments with various sodium chloride concentrations of {50, 100, 140} mmol/L and agarose weights per deionised water volume of {0%, 2%, 6%} to simulate non-restricted (compartments 1 – 2) and restricted (compartments 3 – 6) environments. Brain imaging of ten healthy volunteers (3 females,  $29.6 \pm 3.8$  years) was performed to investigate the in vivo performance of the optimised enhanced SISTINA sequence. All human imaging was performed with the approval of the ethics committee of RWTH Aachen University, Aachen, Germany. Written informed consent was obtained from all volunteers before their participation in the study. In addition,  $B_0$  shimming,  $B_0$  and  $B_1$  field mapping, and hydrogen anatomical imaging were conducted during the

measurement. The entire measurement took about 30 minutes under the First-Level controlled operating mode.

$B_0$  shimming was applied based on a vendor-supplied 3D shimming routine with hydrogen excitation to decrease static field inhomogeneity. For optimisation, the “standard” shimming routine was performed two times, followed by the “advanced” shimming routine three times.  $B_0$  and  $B_1$  field maps with a nominal resolution of 10 mm cubic were obtained to correct SQ and TQ images and were then gridded to 5 mm cubic to correct UTE images in post-processing.

Hydrogen anatomical information was acquired to support White Matter segmentation of sodium images using an MP2RAGE sequence (Marques et al. 2010) with parameters: inversion times of 1 s and 3.2 s;  $4^\circ$  flip angles ; TR of about 8.2 s; TE of 1.91 ms; GRAPPA factor = 1; Field-Of-View =  $240 \times 224 \times 144$  mm<sup>3</sup>; resolution = 2 mm cubic; and acquisition time of about 15 minutes.

### 6.2.3 Data Undersampling

Before undersampled image reconstruction, retrospective undersampling was conducted on the fully sampled UTE, SQ and TQ k-space raw data by pseudo-randomly dropping a subset of projections with five USFs = {1.5, 2, 3, 4, 5}, resulting in decreased numbers of UTE projections = {2976, 2232, 1488, 1116, 888}, reduced numbers of Multiple-Quantum-Filtered projections = {248, 186, 124, 93, 74} and accelerated measurement times = {447, 335, 224, 168, 134} s. Figure 6.1b and Figure 6.1i show the FLORET k-space trajectories of UTE and MQF readouts with original fully Nyquist sampling, respectively. The variously undersampled UTE and MQF k-spaces are present in Figure 6.1c-g and Figure 6.1j-n, respectively. The pseudo-random undersampling was performed offline on MATLAB 2019a (Mathworks, Natick, MA, USA). This undersampling scheme produces noise-like undersampling artefacts, which are added incoherently to the sparse representation of FLORET non-Cartesian raw data with low coherence. Therefore, the above undersampling combined with the FLORET sampling scheme is greatly desirable for CS acceleration.



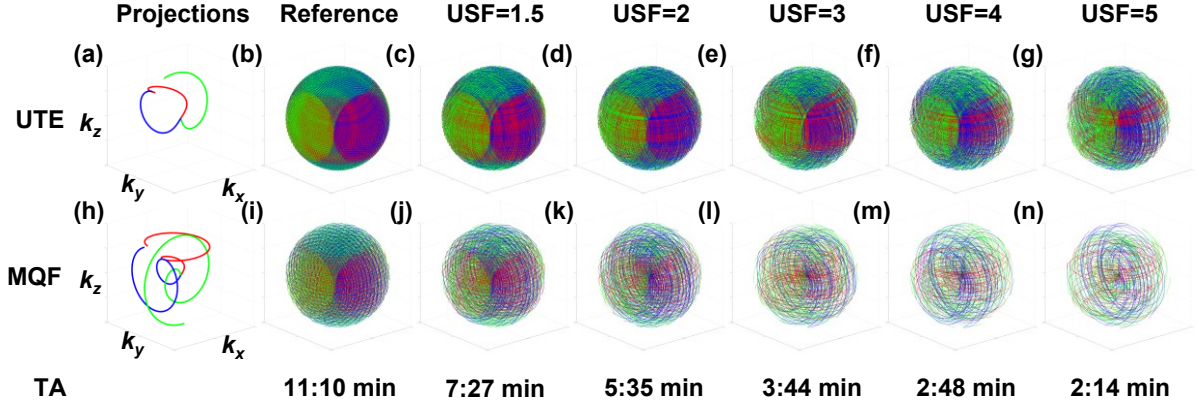


**Figure 6.1** FLORET k-space trajectories. (a) and (h) present the first (in red), middle (in green) and last (in blue) projections of UTE and MQF FLORET, respectively. Fully sampled (b) UTE and (i) MQF FLORET k-space trajectories were pseudo-randomly and retrospectively undersampled by factors of  $\{1.5, 2, 3, 4, 5\}$ : undersampled (c-g) UTE and (j-n) MQF k-spaces. TA = total acquisition time. **Source:** (Chen et al. 2024).

### 6.2.4 Image Reconstruction

The traditional non-linear iterative algorithm proposed by (Lustig et al. 2007) was employed for CS reconstruction, formulated as a constrained optimisation problem:

$$\hat{x} = \arg \min_x \{ \|y - F_u x\|_2^2 + \lambda_1 \|\Psi x\|_1 + \lambda_2 TV(x) \}, \quad (6.1)$$

where  $\|\cdot\|_1$  and  $\|\cdot\|_2$  represent the  $l_1$ - and  $l_2$ -norms, respectively;  $x$  is the iteratively generated image;  $\hat{x}$  is the final reconstructed image;  $y$  is the measured k-space data;  $F_u$  is the undersampled NUFFT operator;  $\Psi$  is the sparsifying transform operator such that  $\Psi x$  becomes sparse;  $TV$  is the finite difference operator that promotes image restoration (Rudin et al. 1992); and  $\lambda_1$  and  $\lambda_2$  are the weighting factors of the transform sparsity and finite difference, respectively. The first term enforces data consistency. The second and third terms promote image sparsity in the sparsifying transform domain and finite-difference domain, respectively.

The minimisation problem in Eq. (6.1) was solved for 320 iterations using a non-linear conjugate gradient method with a wavelet transform operator (Lustig et al. 2007). The optimal weighting factors,  $\lambda_1$  and  $\lambda_2$ , can be different for dataset types; in addition,  $\lambda_1$  and  $\lambda_2$  might vary slightly over echoes, subjects and USFs due to differences in raw data. Therefore, an empirical search for the best regularisation parameters was conducted for each reconstruction in a range of weightings:  $\lambda_1 = [0, 1.0]$ , step size of 0.1; for UTE and SQ,  $\lambda_2 = \{0, 0.0001, 0.0005, 0.001, 0.005, 0.01, 0.05, 0.1, 0.2, 0.3, 0.4, 0.5\}$ ; and for TQ,  $\lambda_2 = \{0, 0.0001, 0.0005, 0.001, 0.005, 0.01, 0.05, 0.1, 0.2, 0.3, 0.4, 0.5, 0.6, 0.7, 0.8, 0.9, 1.0\}$ . The

weighting factors that produced the highest Structural SIMilarity (Wang et al. 2004) were selected.

NUFFT was used to reconstruct fully sampled and undersampled UTE, SQ and TQ raw data based on the Michigan Image Reconstruction Toolbox (Fessler & Sutton 2003). The fully sampled NUFFT-based images acted as reference images. Each reconstructed image was scaled by its maximum intensity to produce an intensity range from 0 to 1 for image comparison. All reconstructions were conducted offline on MATLAB 2019a.

### 6.2.5 Image Segmentation

Hydrogen WM was extracted from high-resolution MP2RAGE images. Then, the hydrogen WM was binarily masked and linearly coregistered to the UTE reference to produce UTE WM. Similarly, the UTE WM was binarily masked and then linearly coregistered to SQ reference to obtain WM for SQ and TQ data. Hydrogen WM segmentation and linear coregistration were performed with the FAST and FLIRT functions in FSL software (FMRIB, Oxford, UK). The resulting partial volume effect maps were thresholded at 0.9, 0.8 and 0.7 to generate binary WM masks for MP2RAGE, UTE and SQ/TQ images, respectively. The brain region was masked manually with caution to exclude the skull. Likewise, the phantom masks were obtained manually with care to avoid partial volume effects.

### 6.2.6 Image Evaluation

SSIM and SNR were employed to assess overall image quality. SSIM compared a test image to a reference image via pixel-by-pixel correlation to obtain the structural degradation of an undersampled reconstruction. The SSIM value (from 0 to 1) was computed over a certain support region (e.g. the entire brain region) to avoid background noise interference. A large SSIM value indicates a high similarity between the test and reference images. The signal amplitude was corrected in each reconstruction to reduce the noise effect and thus obtain an unbiased SNR. The corrected signal is given as  $\Theta = \sqrt{|\text{mean}(\text{signal})^2 - \sigma_{\text{noise}}^2|}$ , where  $\sigma_{\text{noise}}$  is the standard deviation of the noise distribution, which is assumed to follow a Rayleigh distribution. The unbiased SNR provided by  $\Theta \cdot \sigma_{\text{noise}}^{-1}$  was determined in a specific region of interest (e.g. WM).

Contrasts of total, non-restricted and restricted sodium were examined to investigate whether SISTINA images retain weightings towards total and compartmental sodium after CS acceleration. According to the quantum mechanics of SISTINA (Fiege et al. 2013), UTE

images exhibit contrast proportional to total sodium content, regardless of the mobility of sodium ions. Furthermore, since restricted sodium is more likely to evolve from SQ coherences to TQ coherences under multiple-quantum filter excitation, SQ images are weighted towards non-restricted sodium, whereas TQ images are weighted towards restricted sodium (Jaccard et al. 1986).

To investigate the CS effect on in vivo quantitative estimates, the Total Sodium Concentration,  $T_{2f}^*$  and  $T_{2s}^*$  of WM in all undersampled reconstructions were calculated and compared to those values from reference reconstructions. The TSC value in WM,  $TSC_{WM}$ , was determined as  $TSC_{WM} = TSC_{ref} \cdot SNR_{WM}/SNR_{ref}$ , where the SNR of the vitreous humour of the eyes was taken as a reference,  $SNR_{ref}$ , with a fixed TSC,  $TSC_{ref} = 135$  mmol/L (Coe 1969).  $SNR_{ref}$  was calculated based on the top five high-intensity voxels in the vitreous humour to reduce partial volume effects. Both  $SNR_{WM}$  and  $SNR_{ref}$  were obtained from the first-echo UTE images to mitigate signal loss due to relaxation.  $T_{2f}^*$  of WM was determined from the UTE fit given by (Worthoff et al. 2019):

$$SNR_{UTE} = A \cdot \exp\left(-\frac{TE_{UTE}}{T_{2f}^*}\right) + B \cdot \exp\left(-\frac{TE_{UTE}}{T_{2,fix}^*}\right), \quad (6.2)$$

where  $A$  and  $B$  are constants;  $SNR_{UTE}$  and  $TE_{UTE}$  are UTE SNR of WM and UTE echo times, respectively. The first term represents the fast relaxation component ( $T_{2f}^*$  from restricted sodium). The second term accounts for the slow relaxation component ( $T_2^*$  from non-restricted sodium and  $T_{2s}^*$  from restricted sodium), assumed to have a fixed slow relaxation time  $T_{2,fix}^* = 35$  ms. The  $T_{2s}^*$  of WM was obtained from the TQ fit given by (Worthoff et al. 2020):

$$SNR_{TQ} = C \cdot \left[ \exp\left(-\frac{TE_{MQF}}{T_{2f}^*}\right) - \exp\left(-\frac{TE_{MQF}}{T_{2s}^*}\right) \right] \cdot \left[ \exp\left(-\frac{\lambda + \tau}{T_{2f}^*}\right) - \exp\left(-\frac{\lambda + \delta}{T_{2s}^*}\right) \right], \quad (6.3)$$

where  $C$  is a constant;  $SNR_{TQ}$  and  $TE_{MQF}$  are the TQ SNR of WM and MQF echo times, respectively;  $\lambda = 1$  ms is the RF pulse duration;  $\tau = 9.5$  ms is the preparation time, and  $\delta = 60$  us is the evolution time.  $T_{2f}^*$  is the value from UTE fit in Eq. (6.2). If UTE fit was unreliable (i.e. the fit error was greater than 50%) or if the fit did not converge, Eq. (6.3) was used to obtain both  $T_{2f}^*$  and  $T_{2s}^*$  values (Worthoff et al. 2020).

Statistical analysis was utilised to evaluate the in vivo CS performance. A paired right-tailed Student's t-test was used to compare SSIM and SNR values between NUFFT and CS

undersampled reconstructions in ten healthy subjects. A Wilcoxon right-tailed rank sum test was applied if SSIM or SNR did not follow a normal distribution (examined by a Lilliefors test).  $P$ -values of 0.05 or less were considered significant. Descriptive statistics for all quantitative parameters (TSC,  $T_{2f}^*$  and  $T_{2s}^*$ ) were provided as means and standard deviations over all subjects. In vivo quantitative performance was assessed by calculating the difference in mean quantitative values between test and reference reconstructions. For example, the difference (in %) in TSC from CS is given by  $\Delta = (\text{TSC}_{\text{CS}} - \text{TSC}_{\text{ref}})/\text{TSC}_{\text{ref}}$ , where  $\text{TSC}_{\text{CS}}$  and  $\text{TSC}_{\text{ref}}$  are the mean TSC values over all subjects obtained from CS and reference reconstructions, respectively. The quantification of the test reconstruction was considered relatively reliable if the absolute differences of these three quantitative parameters were less than 15%.

## 6.3 Results

### 6.3.1 Phantom Results

The NUFFT and CS reconstructions of the first-echo enhanced SISTINA data from a sodium agarose phantom (Figure 6.2a) with various USFs are shown in Figure 6.2b. In the case of undersampling, CS is generally superior to NUFFT, with noticeably reduced noise and overall better preservation of structures present in the reference images. Moreover, the CS-based SQ/TQ images and highly undersampled CS-based UTE images show less noise than the corresponding reference images. However, as USFs increase, more blurring occurs in CS-based images, which may lead to a loss of information and contrast.

As shown in Figure 6.2b, for both NUFFT and CS, UTE images show contrast proportional to sodium concentration and independent of agarose concentration. However, SQ and TQ images show contrast dependent on the agarose concentration: SQ signal intensity decreases, whereas TQ signal intensity increases with increasing agarose concentrations. Moreover, the TQ signal of sodium liquids with a non-restricted environment is well suppressed. These observations align with the quantum mechanics of SISTINA (Fiege et al. 2013).

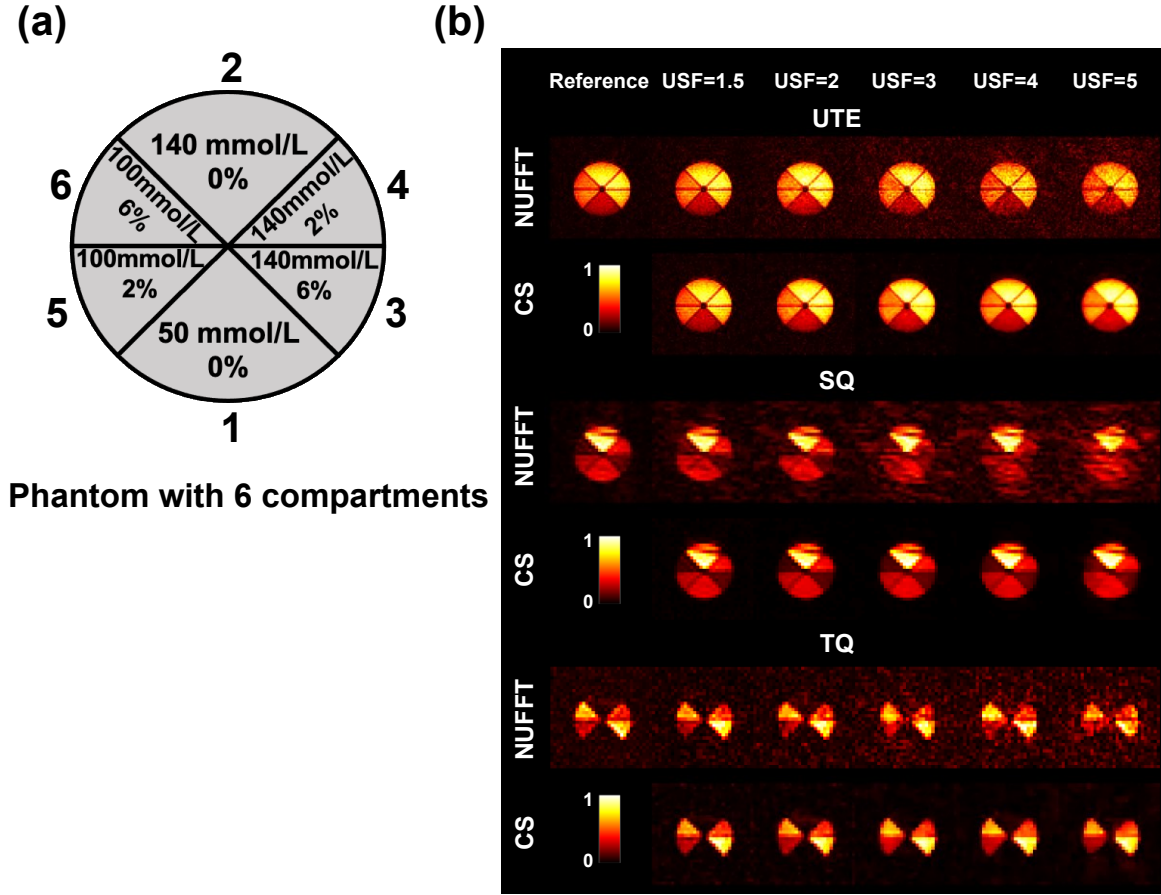


**Figure 6.2** Schematic and first-echo enhanced SISTINA images of a phantom. **(a)** The schematic displays sodium chloride concentration in mmol/L and agarose weight/deionised water volume in percentage. **(b)** Visual comparison between NUFFT and CS across all USFs on the first-echo UTE, SQ and TQ images of the phantom. *Source:* (Chen et al. 2024).

Figure 6.3 presents the quantitative image quality measures for both CS and NUFFT reconstructions of phantom data across all USFs and echoes. In various cases of undersampling, CS yields better SSIM and SNR values than NUFFT, except that four SQ/TQ SSIM values from CS are slightly lower than the values from NUFFT but still show relatively high values of approximately 0.9. Moreover, the CS-based SNR values are even greater than the reference values in most reconstructions (especially for SQ and TQ). In the case of CS with increasing USFs, SNR tends to increase while SSIM decreases slightly, possibly due to blurring and loss of small structures caused by strong undersampling.

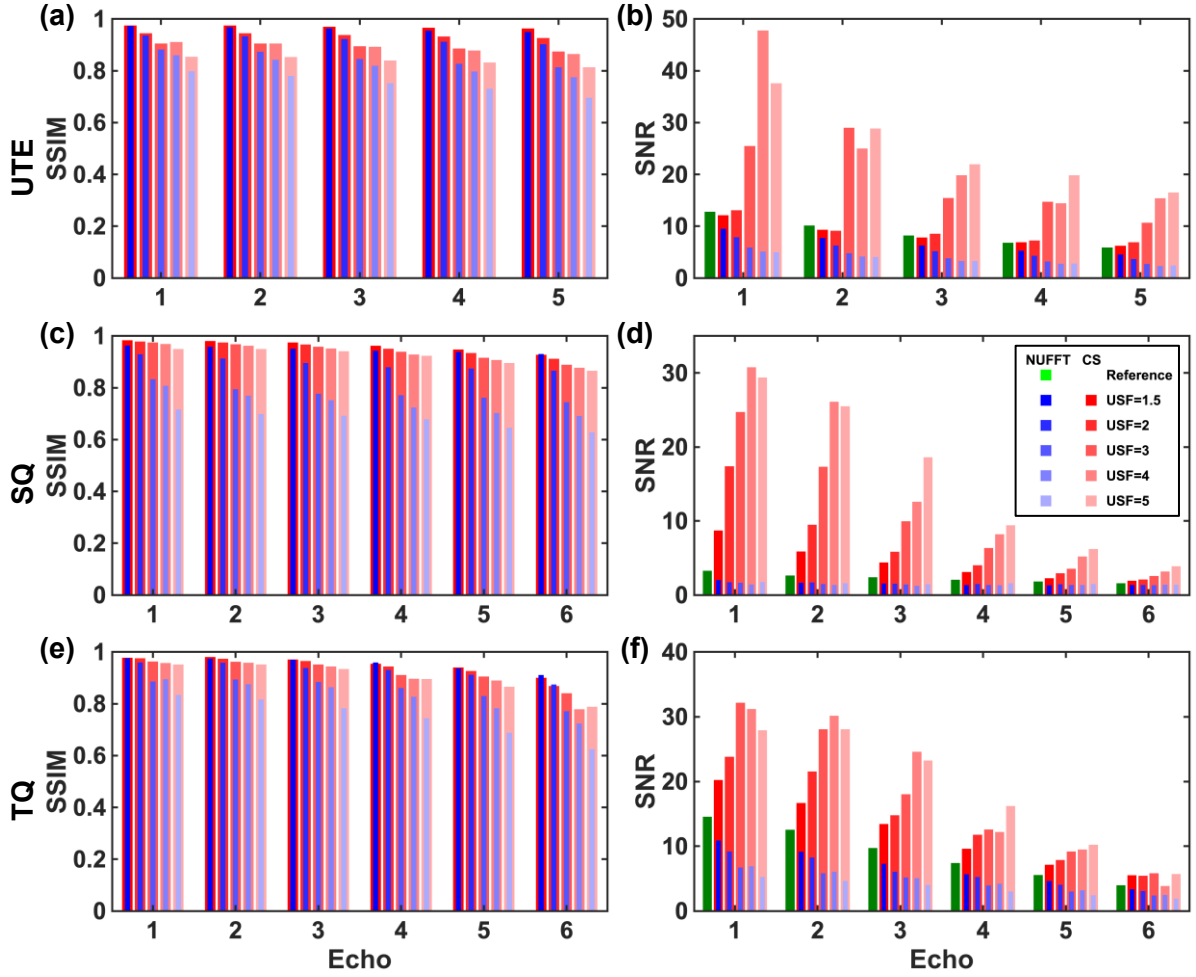


**Figure 6.3** Image quality measures for NUFFT and CS reconstructions of phantom (Figure 6.2a) data across all USFs and echoes. The fully sampled NUFFT reconstructions were used as references (**green**). NUFFT (**blue**) and CS (**red**) reconstructions with various USFs are represented by different colour gradients. SSIM values were computed over the entire phantom for **(a)** UTE and **(c)** SQ images, and over the phantom compartments 3 – 6 for **(e)** TQ images. SNR was computed over the phantom compartment 6 for **(b)** UTE, **(d)** SQ and **(f)** TQ images. The legend in **(d)** applies to all other subplots. *Source:* (Chen et al. 2024).

### 6.3.2 In Vivo Results

Figure 6.4 shows NUFFT and CS reconstructions of an in vivo dataset with five USFs. From visual inspection, CS generally yields remarkably reduced noise and better structure delineation than NUFFT at different USFs. It should be noted that the information contained in the TQ reference image may be affected by severe noise contamination, which makes it difficult to compare the CS-based undersampled TQ image with the TQ reference image. At high USFs (e.g. USF = 4 or 5), even large structures like grey matter are barely visible in NUFFT due to the high noise level, whereas grey matter can be reliably delimited in CS. However, a loss of contrast and information resulting from excessive smoothing can be observed in CS with high undersampling.

In Figure 6.4, as expected, the CerebroSpinal Fluid region with the highest sodium concentration exhibits the highest brightness in all UTE and SQ images. In contrast, the signal from the CSF region with a non-restricted environment is well suppressed in all TQ images. In addition, in all TQ images, brain tissues (consisting of grey matter and WM) with both non-restricted and restricted environments yield higher signal intensity than the CSF region despite the relatively low tissue sodium concentration (Madelin et al. 2014). The weightings towards total, non-restricted and restricted sodium in in vivo images (Figure 6.4) agree well with those in phantom images (Figure 6.2b).

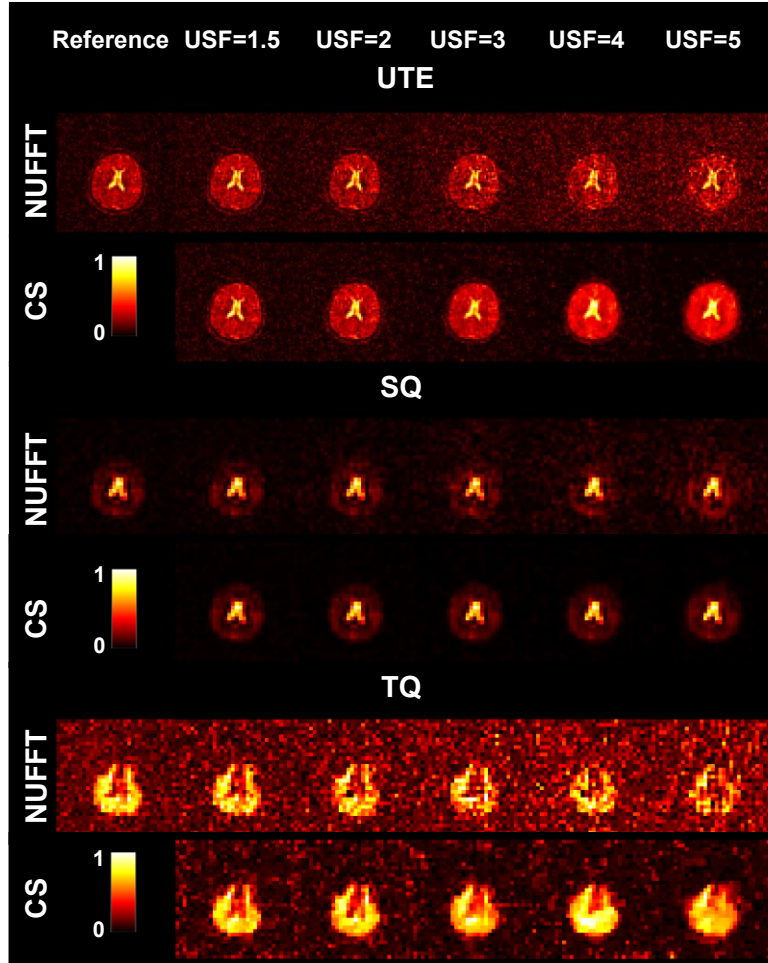


**Figure 6.4** Visual comparison between NUFFT and CS on the first-echo in vivo images across all USFs. The UTE, SQ and TQ data were obtained from the brain of a 32-year-old healthy female. **Source:** (Chen et al. 2024).

Reconstruction of data from other volunteers and other echoes yielded similar results. Figure 6.5 illustrates the quantitative evaluation of NUFFT and CS reconstruction performance using SSIM and SNR over ten healthy subjects across all echoes and all USFs. CS produces significantly ( $p \leq 0.05$ ) higher SNR values than NUFFT in UTE, SQ and TQ images for all USFs and all echoes (Figure 6.5b, d, f). Moreover, the CS-based SNR values are higher than

the reference values in most cases. As USF increases, NUFFT-based SNR decreases due to undersampling, whereas CS-based SNR rises because CS tends to over-smooth at high USFs. As shown in Figure 6.5a and c, in UTE and SQ images, CS-based SSIM values are significantly better than those from NUFFT, except for a few cases where CS-based SSIM is only comparable to NUFFT-based SSIM, but with a sufficiently high value of around 0.9. However, in TQ images, most CS reconstructions lead to similar or even worse SSIM compared to NUFFT (Figure 6.5e), although CS generally outperforms NUFFT with better preservation of the primary structural information for all USFs based on visual inspection (Figure 6.4). Both NUFFT-based and CS-based SSIM values decrease as USFs increase, but CS-based SSIM decreases more slowly than NUFFT-based SSIM due to the denoising property of CS.

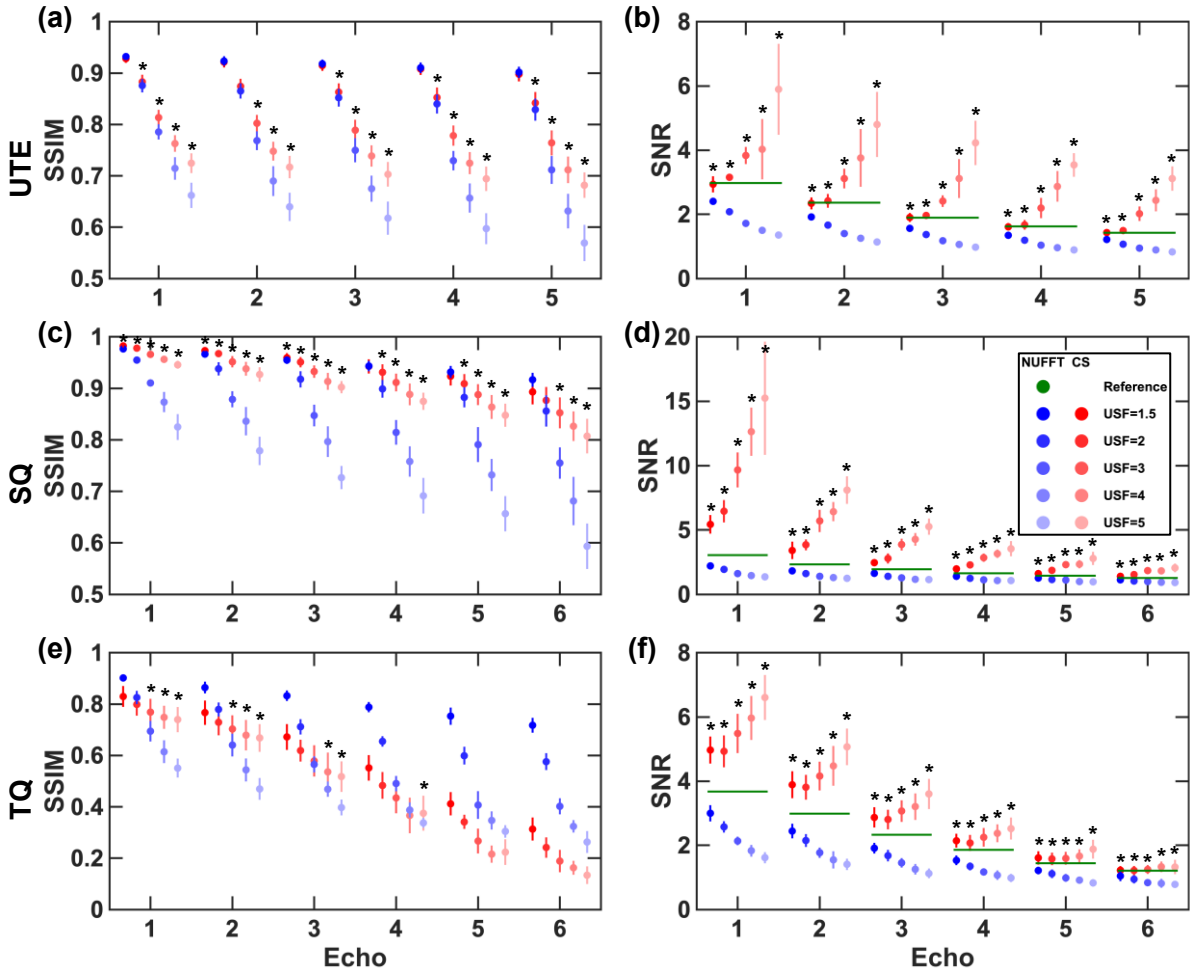


**Figure 6.5** Image quality measures for both NUFFT and CS of in vivo data across all subjects, echoes and USFs. SSIM and SNR values were calculated from reference (green), undersampled NUFFT (blue) and undersampled CS (red) reconstructions. The means and standard deviations of SSIM and SNR values over ten healthy subjects are indicated by dots and whiskers, respectively. SSIM (a, c, e) and SNR (b, d, f) were calculated over the whole brain region and the WM region, respectively. An asterisk (\*) is marked if the CS-based SSIM or SNR value is significantly ( $p \leq 0.05$ ) higher than that from NUFFT. The legend in (d) applies to all other subplots. *Source:* (Chen et al. 2024).



Table 6.2 presents the summary statistics for the quantitative analysis of ten healthy subjects. The reference values for WM calculated from original, fully sampled NUFFT-based reconstructions are:  $T_{2f}^* = 4.8 \pm 0.3$  ms,  $T_{2s}^* = 29.9 \pm 2.0$  ms and  $TSC = 41.9 \pm 1.2$  mmol/L. These values are comparable to values in literatures:  $T_{2f}^*$  from 0.5 ms to 5 ms,  $T_{2s}^*$  from 15 ms to 30 ms and TSC of  $43 \pm 3$  mmol/L (Inglese et al. 2010; Niesporek et al. 2015). NUFFT yields less than 15% bias in both  $T_{2f}^*$  and TSC for all USFs, whereas quantification of  $T_{2f}^*$  and TSC with CS is only reliable at low USFs (1.5 and 2). However, it is worth noting that for all USFs, the CS-based  $T_{2s}^*$  values agree well with the reference values, whereas the NUFFT-based  $T_{2s}^*$  values are overestimated with a difference greater than 15%.

**Table 6.2** Summary statistics for quantitative analysis of ten healthy subjects. Quantitative parameters ( $T_{2f}^*$ ,  $T_{2s}^*$  and TSC) obtained from fully sampled NUFFT-based reconstructions, are provided as reference values. Values in the form of (mean  $\pm$  std) represent the means and standard deviations of quantitative parameters over ten healthy subjects. Differences between quantitative estimates and reference values are provided in parentheses. Differences within the range from  $-15\%$  to  $15\%$  are marked in bold. *Source:* (Chen et al. 2024).

		Reference	USF = 1.5	USF = 2	USF = 3	USF = 4	USF = 5
$T_{2f}^*$ (ms)	NUFFT	$4.8 \pm 0.3$	<b><math>4.5 \pm 0.4</math> (−5%)</b>	<b><math>4.3 \pm 0.4</math> (−9%)</b>	<b><math>4.3 \pm 0.5</math> (−9%)</b>	<b><math>4.1 \pm 0.5</math> (−14%)</b>	<b><math>4.1 \pm 0.5</math> (−14%)</b>
	CS	-	<b><math>4.3 \pm 1.4</math> (−9%)</b>	<b><math>4.1 \pm 1.2</math> (−13%)</b>	$3.2 \pm 1.1$ (−33%)	$3.3 \pm 1.7$ (−31%)	$3.3 \pm 1.6$ (−31%)
$T_{2s}^*$ (ms)	NUFFT	$29.9 \pm 2.0$	$36.6 \pm 2.9$ (22%)	$38.7 \pm 2.8$ (30%)	$43.4 \pm 3.9$ (45%)	$43.5 \pm 3.6$ (46%)	$44.9 \pm 4.1$ (50%)
	CS	-	<b><math>28.6 \pm 3.3</math> (−4%)</b>	<b><math>27.8 \pm 3.3</math> (−7%)</b>	<b><math>28.9 \pm 2.3</math> (−3%)</b>	<b><math>28.3 \pm 3.0</math> (−5%)</b>	<b><math>28.3 \pm 3.6</math> (−5%)</b>
TSC (mmol/L)	NUFFT	$41.9 \pm 1.2$	<b><math>42.0 \pm 1.2</math> (0%)</b>	<b><math>41.6 \pm 1.8</math> (−1%)</b>	<b><math>42.1 \pm 1.1</math> (1%)</b>	<b><math>41.4 \pm 1.8</math> (−1%)</b>	<b><math>41.0 \pm 2.3</math> (−2%)</b>
	CS	-	<b><math>41.9 \pm 1.2</math> (0%)</b>	<b><math>43.7 \pm 1.7</math> (4%)</b>	<b><math>47.9 \pm 0.8</math> (14%)</b>	$52.8 \pm 1.5$ (26%)	$54.1 \pm 2.3$ (29%)

## 6.4 Discussion

In this work, CS had three advantages that were especially suitable for accelerating enhanced SISTINA. First, CS improved the image quality of undersampled SISTINA images through extensive noise suppression and sound structural information recovery. The visual performance of CS was better than NUFFT at various USFs, with remarkably reduced noise in both phantom (Figure 6.2b) and in vivo (Figure 6.4) measurements, which was confirmed by SNR measures (Figure 6.3b, d, f and Figure 6.5b, d, f). Most undersampled CS reconstructions yielded even greater SNR values than reference reconstructions. The remarkable noise reduction facilitated the delineation of structures in CS, whereas these structures were difficult to distinguish from the heavy noise contamination in NUFFT. Consequently, CS generally performed better than NUFFT in SSIM measures of phantom (Figure 6.3a, c, e) and in vivo (Figure 6.5a, c) images,

except for TQ brain images (Figure 6.5e). One possible explanation for the inferior in vivo performance of TQ SSIM is that severe noise contamination in TQ brain images may lead to biased estimates of SSIM and, in particular, the CS-based SSIM was underestimated by comparison of greatly denoised CS-based TQ brain images with heavily noisy TQ reference brain images. Despite the lack of reliable metrics, CS generally yielded better visual performance than NUFFT in TQ reconstructions across various USFs in both phantom (Figure 6.2b) and in vivo (Figure 6.4) studies.

The second advantage of CS was that it had little effect on the weightings towards total, non-restricted and restricted sodium in SISTINA images from both phantom (Figure 6.2b) and in vivo (Figure 6.4) measurements. This implied that with CS-based acceleration, the enhanced SISTINA sequence can still maintain its performance in producing UTE images weighted towards total sodium and SQ (TQ) images weighted towards non-restricted (restricted) sodium.

Third, CS enabled relatively reliable quantification of  $T_{2f}^*$ ,  $T_{2s}^*$  and TSC values at a USF of up to two, whereas NUFFT failed in this quantification due to  $T_{2s}^*$  overestimation (Table 6.2). A possible explanation for the overestimation of  $T_{2s}^*$  is that the SNR values obtained from undersampled NUFFT-based TQ brain images were too low for the signal decay fit routine to get reliable  $T_{2s}^*$ .

Despite the abovementioned advantages, there were three prominent limitations and considerations in practice when applying CS to enhanced SISTINA. First, no gold standard exists for SNR and structure preservation calculations in non-linear iterative reconstructions, which makes it difficult to compare different algorithms. Common methods for determining SNR values rely on a spatially uniform noise distribution with known statistical characteristics. For example, the approach used in this work required a Rayleigh noise distribution. Unlike NUFFT-based noise profiles sufficiently described by the Rayleigh distribution, the statistical and spatial properties of noise from non-linear iterative reconstructions remain unclear. This may introduce bias to the estimation of SNR values (Figure 6.3b, d, f and Figure 6.5b, d, f) and other relative parameters, such as  $T_{2f}^*$ ,  $T_{2s}^*$  and TSC obtained from CS (Table 6.2). SSIM was chosen to measure the degradation of structural delineation, but it is only meaningful if the ground truth image is known. Since ground truth images were not available in this work, reference images were used as an alternative for SSIM calculation. This may result in unreliable SSIM values if the reference image is not in line with the ground truth, such as the TQ reference brain image being substantially contaminated by noise (Figure 6.4, Figure 6.5e). The structural

degradation could be better investigated by calculating a local Point Spread Function (Wech et al. 2012). However, it cannot be directly applied to non-Cartesian FLORET k-space data because the image reconstruction involves gridding interpolation.

The second limitation was long reconstruction times and difficult parameterisation of CS. CS requires complex iterative algorithms to resolve non-linear optimisation problems, resulting in long processing times (often hours). Additionally, manual tuning of regularisation parameters was performed in every reconstruction, leading to an excessive computational burden. It was observed that CS showed poor generalisation across data types but good generalisation across echoes, subjects and USFs. Therefore, the regularisation parameters ( $\lambda_1$  and  $\lambda_2$ ) can remain constant for different echoes, subjects and USFs to mitigate this computational burden. Moreover, the CS reconstruction performance was sensitive to parameter tuning. The rigid manual tuning based on empirical search may have led to image quality dispersion among different echoes and subjects, which may have biased the TSC estimation and echo fit for  $T_{2f}^*$  and  $T_{2s}^*$ . Deep learning has been proposed to enable rapid and accurate reconstruction of undersampled data without manual parameter tuning and might be an option to alleviate this limitation (Adlung et al. 2021; Wang et al. 2016).

Third, the noise level reduced with increasing USFs (Figure 6.3b, d, f and Figure 6.5b, d, f), while the errors in image contrast (Figure 6.3a, c, e, and Figure 6.5a, c, e) and quantitative analysis (Table 6.2) increased. Therefore, consideration must be given to choosing a proper USF that balances the above two factors. In this study, CS only enabled a USF of up to two for enhanced SISTINA with reduced noise and appropriate maintenance of structural information and quantitative estimation with error below 15%. Compared with hydrogen MRI, the achievable USF in non-hydrogen MRI is limited, primarily due to the strong noise caused by the relatively low NMR sensitivity of non-hydrogen nuclei. Previous studies have indicated that the CS performance (Eq. (6.1)) in sodium MRI can be further promoted by incorporating hydrogen anatomical constraints (Gnahm et al. 2014; Gnahm & Nagel 2015; Zhao et al. 2021) or sparsity in learned dictionaries (Behl et al. 2016; Kratzer et al. 2020, 2021). Furthermore, providing prior knowledge about the temporal evolution of signal allowed for a more accurate estimation of transverse relaxation times for CS in hydrogen MRI (Zimmermann et al. 2018). The above constraints can be added to the CS cost function in Eq. (6.1), which might enable a higher USF for enhanced SISTINA.

## 6.5 Conclusion

Driven by the interest in acquisition time reduction for enhanced SISTINA, this proof-of-concept study demonstrated the feasibility of applying CS to accelerate enhanced SISTINA acquisitions of the human brain at 7T. The experimental results on retrospectively undersampled k-space data show that CS accelerated enhanced SISTINA by up to twofold at 7T in this study with higher SNR and better structure preservation compared to NUFFT, while maintaining relatively reliable in vivo quantitative estimates and reasonable weightings towards total and compartmental sodium. The feasibility of the reduction in acquisition times may have the potential to facilitate the applicability of enhanced SISTINA in scientific research and clinical practice.

## 7 Conclusion

The hydrogen nucleus has been the target nucleus for standard MRI applications, with descriptive interpretation mainly focusing on tissue contrasts and signal appearance. However, the indirect association of the hydrogen nucleus with biochemical processes renders it a rather unspecific correlate for various pathologies and makes the traditional MRI inherently challenging.

Sodium MRI, particularly Multiple-Quantum-Filtered sodium MRI, with its essential role in various biochemical processes, could significantly improve medical diagnosis and treatment planning possibilities. Its direct link to cell integrity and tissue viability allows specific interpretation of MQF sodium MRI acquisitions. With a suitable measurement protocol, MQF sodium MRI can be interpreted as a clinical biomarker and thus extend and complement current imaging techniques. For example, Enhanced SIMultaneous Single-quantum and TRIPLE-quantum-filtered imaging of  $^{23}\text{Na}$  is one of the MQF sodium MRI techniques that can selectively detect the distribution of restricted (mostly intracellular) sodium, which may be sensitive to metabolic cellular dysfunction.

MQF sodium MRI has great potential but faces similarly significant challenges. The disadvantage is that the clinical application of MQF sodium MRI is mainly hampered by its low image quality and long acquisition times. Alleviating these limitations has been the primary focus of recent developments in MQF sodium MRI and is also the focus of this thesis. In the following, the novel contributions of this work will be summarised, and suggestions for future research will be proposed.

### 7.1 Thesis Contribution

This work has emphasised two main aspects of MRI: data acquisition and image reconstruction. The main contributions are briefly recapitulated in the following:

**Chapter 5 Data Acquisition** In this work, the enhanced SISTINA sequence was optimised for 7T using Fermat Looped, ORthogonally Encoded Trajectories, which have high k-space filling efficiency and good undersampling potential. A qualitative comparison of image quality between the optimised enhanced SISTINA sequence and the conventional sequence was conducted in phantom measurements. The experimental results showed that the optimised enhanced SISTINA sequence greatly improved Ultra-short Echo Time image quality, while maintaining MQF image performance and introducing incoherence to the raw data. The

sequence optimisation satisfies the prerequisite for applying Compressed Sensing technique to enhanced SISTINA for faster scanning.

**Chapter 6 Image Reconstruction** In this work, the CS technique was applied to the optimised enhanced SISTINA proposed in Chapter 5 to achieve faster acquisition without significantly degrading image quality. Quantitative validation of reconstruction performance was conducted in both phantom and in vivo measurements. The undersampled CS-based SISTINA images were compared to fully sampled and undersampled Non-Uniform Fast Fourier Transform-based images. The experimental results showed that CS accelerated enhanced SISTINA acquisitions by up to twofold in this work with less noise and better structure preservation than NUFFT, while maintaining relatively accurate in vivo quantification and proper contrasts of total and compartmental sodium. The acquisition time reduction might have the potential to improve the applicability of enhanced SISTINA in scientific research and clinical practice.

In a nutshell, the presented work mitigates the challenges of MQF sodium MRI by (1) optimising the enhanced SISTINA sequence for improving image quality and introducing incoherence to raw data and (2) applying CS reconstruction to reduce enhanced SISTINA acquisition times. Together these findings indicate the potential of MQF sodium MRI in a clinical setting.

## 7.2 Future Research

In the future, the clinical potential of CS-based accelerated MQF sodium MRI may be further explored in several areas. For example, since the resolution of conventional enhanced SISTINA images is commonly sacrificed in favour of shorter acquisition times and a higher Signal-to-Noise Ratio, the application of CS to achieve MQF sodium MRI with a higher resolution while maintaining an acceptable protocol duration offers the potential to yield a clinical significance.

Furthermore, since the intracellular sodium concentration, volume fraction and molar fraction can provide valuable information for medical diagnosis or medical treatment (Shymanskaya et al. 2020; Worthoff et al. 2019, 2020), it is worthwhile to investigate the effect of CS on intracellular sodium quantification.

Finally, CS is not limited to sodium MRI but can also be applied to other nuclei with even lower Nuclear Magnetic Resonance sensitivity, such as potassium ( $^{39}\text{K}$ ), chlorine ( $^{35}\text{Cl}$ ) and oxygen ( $^{17}\text{O}$ ) (Hu et al. 2020).

## APPENDIX

### A1 Slice-Selective Excitation

In the presence of gradients, two steps are required to uniquely excite a slice in Two-Dimensional MRI. First, a slice-selective gradient is applied along an axis perpendicular to the desired slice plane, resulting in a linear variation of spin precession frequencies in that direction. Second, a specially tailored RF pulse is imposed simultaneously, whose frequency components match the narrow range of frequencies contained in the desired slice. The combination of these two steps ensures that only nuclei within the selected slice are excited.

As shown in the figure below, each slice has a different centre frequency,  $\omega_c$ , determined by its position,  $z$ , along the slice-selective gradient,  $G_z$ , given by:

$$\omega_c = \gamma(B_0 + z \cdot G_z) = \omega_0 + \gamma \cdot z \cdot G_z, \quad (\text{A1})$$

where  $B_0$  is the main magnetic field strength and  $\omega_0$  is its corresponding Larmor frequency.

Each slice has a finite width,  $\Delta z$ , and therefore, it contains a range of spin precession frequencies centred around  $\omega_c$ . These quantities are related by the equation below:

$$\Delta\omega = \gamma \cdot \Delta z \cdot G_z. \quad (\text{A2})$$

In common practice,  $\Delta\omega$  is held constant (on the order of 1-2 kHz) and slice thickness  $\Delta z$  is changed by adjusting  $G_z$ . Stronger gradients result in thinner slices, and vice versa.

In this way, the frequency-encoding gradient uniquely identifies a slice using the centre frequency,  $\omega_c$ , to determine the slice position and using the frequency range,  $\Delta\omega$ , to determine the slice thickness,  $\Delta z$ .

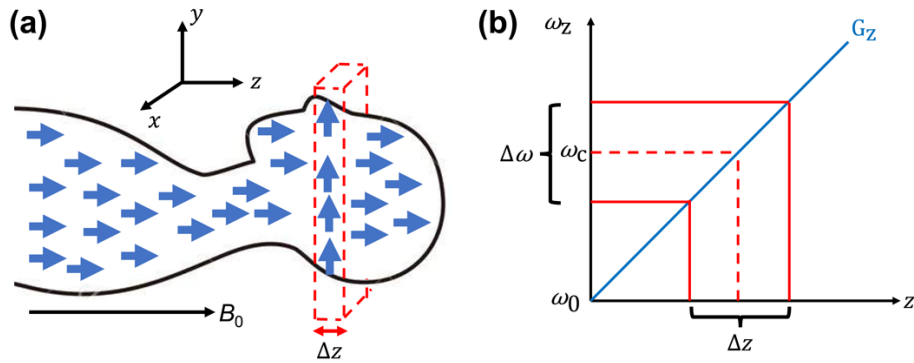


**Figure A1** Slice-selective excitation. **(a)** An excited slice of the human brain (red dashed box). **(b)** the relationship between the slice position ( $z$ ) and the spin precession frequency ( $\omega$ ) in the presence of the slice-selective gradient,  $G_z$ .

The next step is to stimulate the slice with an RF pulse, which uniformly excites a specific range of frequencies. The ideal RF excitation to achieve this frequency profile is a so-called sinc pulse because it denotes a rectangular spectral profile along an axis. In practice, the sinc pulse is modified by a process called apodisation to limit the number of side lobes and change its shape. Other pulse shapes, including those with a Gaussian envelope, are also used in practice.

## A2 Noise in MRI

### *Origin of Noise*

According to Faraday's law, the magnetic flux produced by the rotating magnetic moments creates an electromotive force (emf) in the receive coil. Generally, the noise voltage mainly derives from random fluctuations in the receive coil electronics and the sample. The variance of the fluctuating noise voltage is given by:

$$\text{var}(\text{emf}_{\text{noise}}) \equiv \sigma_{\text{thermal}}^2 \overline{(\text{emf}_{\text{noise}} - \overline{\text{emf}_{\text{noise}}})^2} = 4kT \cdot R \cdot BW, \quad (\text{A3})$$

where the horizontal bar over a value implies an average value;  $R$  is the effective resistance of the coil loaded by the body, and  $BW$  is the bandwidth of the noise-voltage detecting system. As represented in Eq. (A3), the random thermal fluctuations in the measured signal are called white fluctuations with a Gaussian distribution.

### *Improving SNR by Signal Averaging*

It is well-known that the SNR can be improved by repeating an entire imaging experiment  $N_{\text{acq}}$  times and averaging the signal over these  $N_{\text{acq}}$  measurements. The averaged k-space signal,  $S_{\text{m,av}}(k)$ , of  $S_{\text{m}}(k)$  is:

$$S_{\text{m,av}}(k) = \frac{1}{N_{\text{acq}}} \sum_{i=1}^{N_{\text{acq}}} S_{\text{m},i}(k). \quad (\text{A4})$$

The individual  $N_{\text{acq}}$  measurements are assumed to be statistically independent from each other. Therefore, the mean signal remains unchanged:

$$\overline{S_{\text{m,av}}(k)} = \frac{1}{N_{\text{acq}}} \sum_{i=1}^{N_{\text{acq}}} \overline{S_{\text{m},i}(k)} = \frac{1}{N_{\text{acq}}} (N_{\text{acq}} S(k)) = S(k). \quad (\text{A5})$$

As a result, the noise variance from each measurement,  $\sigma_{\text{thermal}}^2$ , adds in quadrature to the total noise variance of the average signal,  $S_{\text{m,av}}(k)$ :



$$\sigma_{\text{thermal,av}}^2(k) \equiv \text{var}\left(S_{\text{m,av}}(k)\right) = \frac{1}{N_{\text{acq}}} \sum_{i=1}^{N_{\text{acq}}} \text{var}\left(S_{\text{m,i}}(k)\right) = \frac{\sigma_{\text{thermal}}^2(k)}{N_{\text{acq}}}. \quad (\text{A6})$$

Therefore,

$$\sigma_{\text{thermal,av}}(k) = \frac{\sigma_{\text{thermal}}(k)}{\sqrt{N_{\text{acq}}}}. \quad (\text{A7})$$

The SNR of the k-space signal becomes:

$$\text{SNR}(k) = \frac{\overline{S_{\text{m,av}}(k)}}{\sigma_{\text{thermal,av}}(k)} = \sqrt{N_{\text{acq}}} \frac{S(k)}{\sigma_{\text{thermal}}(k)}. \quad (\text{A8})$$

Hence, if the noise is uncorrelated from one experiment to the next, the standard noise deviation is reduced by a factor of  $1/\sqrt{N_{\text{acq}}}$ . This yields an increase in SNR by a factor of  $\sqrt{N_{\text{acq}}}$ .

### ***Signal and Noise in Magnitude Images***

The signal in magnitude images,  $\tilde{\rho}$ , follows a Rician distribution:

$$p_{\tilde{\rho}} = \frac{\tilde{\rho}}{\sigma_{\text{thermal}}^2} \exp\left\{-\frac{\tilde{\rho}^2 + \rho^2}{2\sigma_{\text{thermal}}^2}\right\} I_0\left(\frac{\tilde{\rho}\rho}{\sigma_{\text{thermal}}^2}\right), \quad (\text{A9})$$

where  $I_0$  is the modified Bessel function and  $\rho$  is the signal from the background. The Rician distribution becomes a Rayleigh distribution in the case of a signal-free background, i.e.  $\rho \rightarrow 0$ :

$$p_{\tilde{\rho}} = \frac{\tilde{\rho}}{\sigma_{\text{thermal}}^2} \exp\left\{-\frac{\tilde{\rho}^2}{2\sigma_{\text{thermal}}^2}\right\}. \quad (\text{A10})$$

The Rayleigh distribution facilitates the estimation of the standard noise deviation,  $\sigma_{\text{thermal}}$ , from the magnitude image. The mean and variance in regions without NMR signal are determined analytically by:

$$\bar{\tilde{\rho}} = \sigma_{\text{thermal}} \sqrt{\frac{\pi}{2}}, \quad \sigma_{\tilde{\rho}}^2 = \left(2 - \frac{\pi}{2}\right) \sigma_{\text{thermal}}^2. \quad (\text{A11})$$

For an unbiased estimate of SNR, the Rician noise needs to be considered. Typically, this is achieved by a simple correction of the magnitude image intensities, as suggested by (Gudbjartsson & Patz 1995):

$$\rho \approx \sqrt{|\tilde{\rho} - \sigma_{\text{thermal}}|}. \quad (\text{A12})$$

### A3 Non-Cartesian Sampling

#### *Twisted Projection Imaging*

Twisted Projection Imaging (TPI) aims to reduce acquisition time by sampling spirally along the concentric cones in k-space. Although this implies longer trajectories from the k-space centre to  $k_{max}$ , the twisted trajectory design can be optimised to mitigate sampling inefficiency simultaneously. The original concept was proposed in 2D by (Jackson et al. 1992), who showed that a more uniform sampling density could be achieved by twisting spokes.

Boada et al. extended this idea into 3D in 1997 (Boada, et al. 1997b). The 3D TPI is shown in Figure A2. To ensure spherically symmetric sampling in k-space, the number of sampling points inside a spherical shell needs to be proportional to the volume of the shell. TPI consists of two main steps:

1. The sampled sphere in k-space is divided into multiple latitudinal rings. According to the Nyquist criterion, the spacing between each circle is designated as  $FOV^{-1}$ . Together with the centre of k-space, each ring defines a cone over which the sampling points should be uniformly distributed.
2. Due to hardware limitations and the initial condition  $k_0 \neq 0$ , the twisting trajectory starts after a fraction  $p$  of the spoke, i.e. sampling starts radially from the centre of k-space and traverses in a twisted way after  $pk_{max}$ .

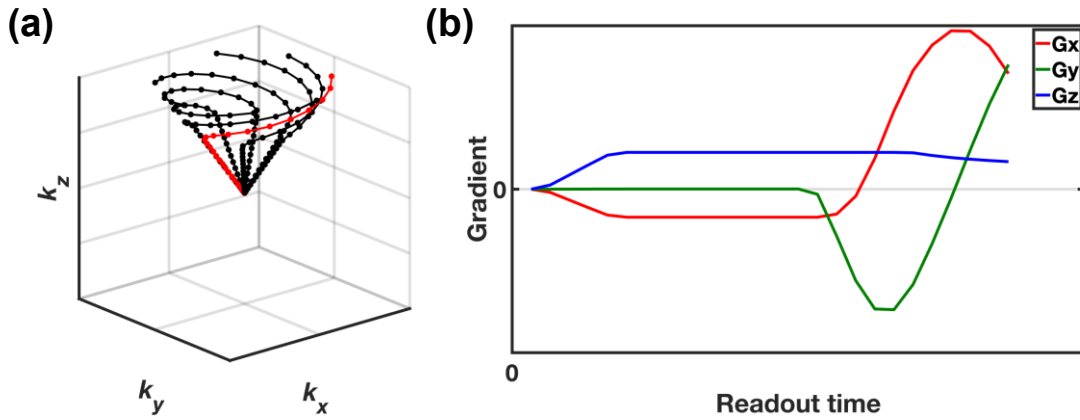


**Figure A2** Twisted projection imaging. **(a)** Multiple projections on a concentric cone in k-space. **(b)** The gradient waveforms of a representative projection.

The choice of  $p$  affects the number of projections required to achieve uniform sampling distributions on each cone. A lower fraction of radial sampling trajectory will reduce the number of required projections by a factor of  $p$ , thus reducing the total data acquisition time by a factor of  $1 - p$ . However, a lower  $p$  requires a higher slew rate of the readout gradient.

Another consideration in choosing  $p$  is the desired readout time. A lower fraction leads to more twisting and longer sampling trajectories. The highest traversal speed through k-space is limited by the achievable gradient strength and is thus another design parameter in TPI acquisitions. It should be noted that  $p$  is kept constant throughout the entire acquisition to ensure an isotropic PSF.

TPI significantly reduces acquisition times and provides a uniform sampling pattern for good SNR efficiency. However, the complicated k-space trajectory design poses challenges to implementation and hardware. Furthermore, the readout trajectory length is inherently limited due to the fast decay of the sodium NMR signal. Nevertheless, TPI yielded improved image quality compared to standard sodium acquisition schemes with fixed readout durations and measurement times (Romanzetti et al. 2014).

### 3D Cones

TPI consists of two components with different sampling strategies: (1)  $k < k_0$  is acquired radially, and (2)  $k > k_0$  is sampled along spiral cone trajectories. The transition between radial and twisted sampling usually marks the point of maximum slew rate constraint. Gurney et al. proposed the 3D cones in 2006 (Gurney et al. 2006), as shown in Figure A3. 3D cones utilise a numerical algorithm for radial and twisted trajectories in 3D, focusing on slew rate constraints. The application of 3D cones in sodium MRI has been demonstrated by (Riemer et al. 2014; Staroswiecki et al. 2010).

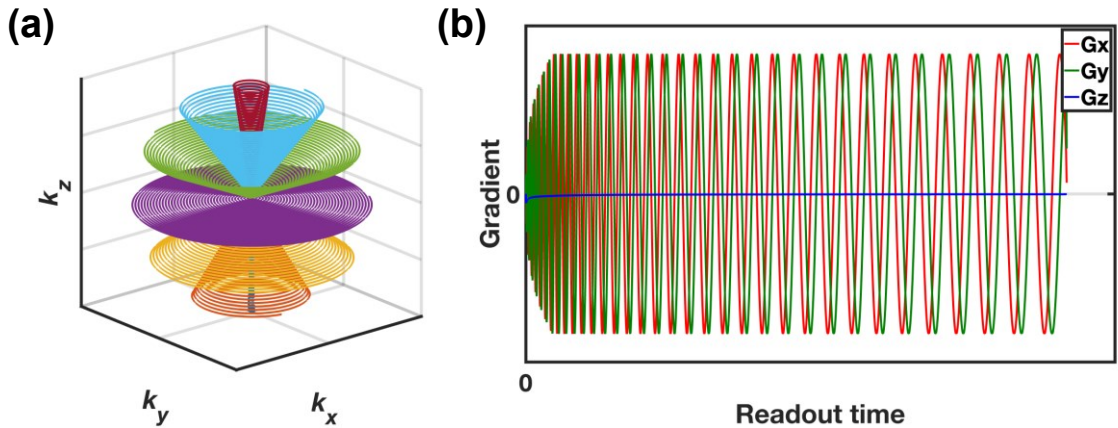


**Figure A3** 3D cone trajectories. (a) part of the k-space. (b) the gradient waveforms of a representative projection.

The 3D cones trajectories emphasise hardware limitations and provides elegant descriptions of gradient waveforms. However, the condition of uniform sampling density is less stringently pursued, and therefore, the SNR efficiency is lower compared to TPI and density-adapted radial

acquisitions. Furthermore, the length of each projection varies between different cones, making data acquisition difficult.

---

**REFERENCES**

- Adlung A., Paschke N. K., Golla A. K., Bauer D., Mohamed S. A., Samartzi M., Fatar M., Neumaier-Probst E., Zöllner F. G., Schad L. R.:  $^{23}\text{Na}$  MRI in ischemic stroke: acquisition time reduction using postprocessing with convolutional neural networks. *NMR Biomed.* (2021) 34: e4474.
- Allen S. P., Morrell G. R., Peterson B., Park D., Gold G. E., Kaggie J. D., Bangerter N. K.: Phase-Sensitive Sodium B1 Mapping. *Magn. Reson. Med.* (2011) 65: 1125–1130.
- Aue W. P., Bartholdi E., Ernst R. R.: Two-dimensional spectroscopy. Application to nuclear magnetic resonance. *J. Chem. Phys.* (1976) 64: 2229–2246.
- Bangerter N. K., Tarbox G. J., Taylor M. D., Kaggie J. D.: Quantitative sodium magnetic resonance imaging of cartilage, muscle, and tendon. *Quant. Imaging Med. Surg.* (2016) 6: 699–714.
- Bansal N., Germann M. J., Lazar I., Malloy C. R., Sherry A. D.: In vivo Na-23 MR imaging and spectroscopy of rat brain during TmDOTP5– infusion. *J. Magn. Reson. Imaging* (1992) 2: 385–391.
- Behl N. G. R., Gnahn C., Bachert P., Ladd M. E., Nagel A. M.: Three-dimensional dictionary-learning reconstruction of  $^{23}\text{Na}$  MRI data. *Magn. Reson. Med.* (2016) 75: 1605–1616.
- Benkhedah N., Bachert P., Semmler W., Nagel A. M.: Three-Dimensional Biexponential Weighted  $^{23}\text{Na}$  Imaging of the Human Brain with Higher SNR and Shorter Acquisition Time. *Magn. Reson. Med.* (2013) 70: 754–765.
- Bjartmar C., Trapp B. D.: Axonal and neuronal degeneration in multiple sclerosis: Mechanisms and functional consequences. *Curr. Opin. Neurol.* (2001) 14: 271–278.
- Bloch F., Hansen W., Packard M.: The Nuclear Induction Experiment. *Phys. Rev.* (1946) 70: 474–485.
- Blunck Y., Josan S., Taqdees S. W., Moffat B. A., Ordidge R. J., Cleary J. O., Johnston L. A.: 3D-multi-echo radial imaging of  $^{23}\text{Na}$  (3D-MERINA) for time-efficient multi-parameter tissue compartment mapping. *Magn. Reson. Med.* (2018) 79: 1950–1961.
- Blunck Y., Kolbe S. C., Moffat B. A., Ordidge R. J., Cleary J. O., Johnston L. A.: Compressed sensing effects on quantitative analysis of undersampled human brain sodium MRI. *Magn. Reson. Med.* (2019) 83: 1025–1033.

## REFERENCES

---

- Boada F. E., Gillen J. S., Shen G. X., Chang S. Y., Thulborn K. R.: Fast Three Dimensional Sodium Imaging. *Magn. Reson. Med.* (1997) a 37: 706–715.
- Boada F. E., Gillen J. S., Shen G. X., Chang S. Y., Thulborn K. R.: Fast Three Dimensional Sodium Imaging. *Magn. Reson. Med.* (1997) b 37: 706–715.
- Boada F. E., LaVerde G., Jungreis C., Nemoto E., Tanase C., Hancu I.: Loss of cell ion homeostasis and cell viability in the brain: what sodium MRI can tell us. *Curr. Top. Dev. Biol.* (2005) 70: 77–101.
- Boada F. E., Qian Y., Nemoto E., Jovin T., Jungreis C., Jones S. C., Weimer J., Lee V.: Sodium MRI and the assessment of irreversible tissue damage during hyper-acute stroke. *Transl. Stroke Res.* (2012) 3: 236–245.
- Boada F. E., Shen G. X., Chang S. Y., Thulborn K. R.: Spectrally weighted twisted projection imaging: reducing T2 signal attenuation effects in fast three-dimensional sodium imaging. *Magn. Reson. Med.* (1997) 38: 1022–1028.
- Bodenhausen G., Kogler H., Ernst R. R.: Selection of Coherence-Transfer Pathways in NMR Pulse Experiments. *J. Magn. Reson.* (1984) 58: 370–388.
- Bottomley P. A.: Sodium MRI in human heart: a review. *NMR Biomed.* (2016) 29: 187–196.
- Brown R. W., Cheng Y. C. N., Haacke E. M., Thompson M. R., Venkatesan R.: *Magnetic Resonance Imaging: Physical Principles and Sequence Design* (2014) John Wiley & Sons, Inc.
- Burstein D., Springer C. S.: Sodium MRI Revisited. *Magn. Reson. Med.* (2019) 82: 521–524.
- Candès E. J., Romberg J. K., Tao T.: Stable Signal Recovery From Incomplete and Inaccurate Measurements. *Commun. Pure Appl. Math.* (2006) a 59: 1207–1223.
- Candès E. J., Romberg J., Tao T.: Robust uncertainty principles: exact signal reconstruction from highly incomplete frequency information. *IEEE Trans. Inf. Theory* (2006) b 52: 489–509.
- Candès E. J., Romberg J., Tao T.: Robust Uncertainty Principles: Exact Signal Reconstruction From Highly Incomplete Frequency Information. *IEEE Trans. Inf. Theory* (2006) c 52: 489–509.
- Candes E. J., Tao T.: Decoding by linear programming. *IEEE Trans. Inf. Theory* (2005) 51: 4203–4215.

## REFERENCES

---

- Chen F., Taviani V., Malkiel I., Cheng J. Y., Tamir J. I., Shaikh J., Chang S. T., Hardy C. J., Pauly J. M., Vasanawala S. S.: Variable-density single-shot fast spin-echo MRI with deep learning reconstruction by using variational networks. *Radiology* (2018) 289: 366–373.
- Chen Q., Shah N. J., Worthoff W. A.: Compressed Sensing in Sodium Magnetic Resonance Imaging: Techniques, Applications, and Future Prospects. *J. Magn. Reson. Imaging* (2022) 55: 1340–1356.
- Chen Q., Worthoff W. A., Shah N. J.: Triple-Quantum-Filtered Sodium MRI at 7T : Optimization of the Enhanced SISTINA Sequence Using FLORET k-space Trajectories. *Proc. 29th Annu. Meet. ISMRM* (2021).
- Chen Q., Worthoff W. A., Shah N. J.: Accelerated multiple-quantum-filtered sodium magnetic resonance imaging using compressed sensing at 7 T. *Magn. Reson. Imaging* (2024) 107: 138–148.
- Choi C. H., Stegmayr C., Shymanskaya A., Worthoff W. A., da Silva N. A., Felder J., Langen K. J., Shah N. J.: An in vivo multimodal feasibility study in a rat brain tumour model using flexible multinuclear MR and PET systems. *EJNMMI Phys.* (2020) 7: 50.
- Clausen T.: Na<sup>+</sup>-K<sup>+</sup> Pump Regulation and Skeletal Muscle Contractility. *Physiol. Rev.* (2003) 83: 1269–1324.
- Coe J. I.: Postmortem Chemistries on Human Vitreous Humor. *Am J Clin Pathol* (1969) 51: 741–750.
- Cooley J. W., Tukey J. W.: An Algorithm for the Machine Calculation of Complex Fourier Series. *Math. Comput.* (1965) 19: 297.
- Damadian R.: Tumor Detection by Nuclear Magnetic Resonance. *Sci.* (1971) 171: 1151–1153.
- Damadian R., Goldsmith M., Minkoff L.: NMR in Cancer: XVI. FONAR Image of the Live Human Body. *Physiol. Chem. Phys.* (1977) 9: 97–109.
- Donoho D. L.: Compressed Sensing. *IEEE Trans. Inf. Theory* (2006) 52: 1289–1306.
- Fessler J. A., Sutton B. P.: Nonuniform Fast Fourier Transforms Using Min-Max Interpolation. *IEEE Trans. Signal Process.* (2003) 51: 560–574.
- Fiat D., Hankiewicz J., Liu S., Trbovic S., Brint S.: 17O magnetic resonance imaging of the human brain. *Neurol. Res.* (2004) 26: 803–808.
- Fiege D. P., Romanzetti S., Mirkes C. C., Brenner D., Shah N. J.: Simultaneous single-quantum

## REFERENCES

---

- and triple-quantum-filtered MRI of  $^{23}\text{Na}$  (SISTINA). *Magn. Reson. Med.* (2013) 69: 1691–1696.
- Francis S., Buchanan C. E., Prestwich B., Taal M. W.: Sodium MRI: a new frontier in imaging in nephrology. *Curr. Opin. Nephrol. Hypertens.* (2017) 26: 435–441.
- Gnahm C., Bock M., Bachert P., Semmler W., Behl N. G. R., Nagel A. M.: Iterative 3D projection reconstruction of  $^{23}\text{Na}$  data with an  $^1\text{H}$  MRI constraint. *Magn. Reson. Med.* (2014) 71: 1720–1732.
- Gnahm C., Nagel A. M.: Anatomically weighted second-order total variation reconstruction of  $^{23}\text{Na}$  MRI using prior information from  $^1\text{H}$  MRI. *Neuroimage* (2015) 105: 452–461.
- Greiser A., von Kienlin M.: Efficient k-space sampling by density-weighted phase-encoding. *Magn. Reson. Med.* (2003) 50: 1266–1275.
- Grodd W., Klose U.: Sodium-MR-imaging of the brain: initial clinical results. *Neuroradiology* (1988) 30: 399–407.
- Gudbjartsson H., Patz S.: The rician distribution of noisy mri data. *Magn. Reson. Med.* (1995) 34: 910–914.
- Gurney P. T., Hargreaves B. A., Nishimura D. G.: Design and Analysis of a Practical 3D Cones Trajectory. *Magn. Reson. Med.* (2006) 55: 575–582.
- Hancu I., Boada F. E., Shen G. X.: Three-dimensional triple-quantum-filtered  $^{23}\text{Na}$  imaging of in vivo human brain. *Magn. Reson. Med.* (1999) 42: 1146–1154.
- Hilal S. K., Maudsley A. A., Ra J. B., Simon H. E., Roschmann P., Wittekoek S., Cho Z. H., Mun S. K.: In vivo NMR imaging of sodium-23 in the human head. *J. Comput. Assist. Tomogr.* (1985) 9: 1–7.
- Hu R., Kleimaier D., Malzacher M., Hoesl M. A. U., Paschke N. K., Schad L. R.: X-nuclei imaging: Current state, technical challenges, and future directions. *J. Magn. Reson. Imaging* (2020) 51: 355–376.
- Huhn K., Engelhorn T., Linker R. A., Nagel A. M.: Potential of sodium MRI as a biomarker for neurodegeneration and neuroinflammation in multiple sclerosis. *Front. Neurol.* (2019) 10: 84.
- Hutchison R. B., Malhotra D., Hendrick R. E., Chan L., Shapiro J. I.: Evaluation of the Double-Quantum Filter for the Measurement of Intracellular Sodium Concentration. *J. Biol. Chem.*



- (1990) 265: 15506–15510.
- Inglese M., Madelin G., Oesingmann N., Babb J. S., Wu W., Stoeckel B., Herbert J., Johnson G.: Brain tissue sodium concentration in multiple sclerosis: A sodium imaging study at 3 tesla. *Brain A J. Neurol.* (2010) 133: 847–857.
- Jaccard G., Wimperis S., Bodenhausen G.: Multiple-Quantum NMR Spectroscopy of  $S=3/2$  Spins in Isotropic Phase: A New Probe for Multiexponential Relaxation. *J. Chem. Phys.* (1986) 85: 6282–6293.
- Jackson J. I., Meyer C. H., Nishimura D. G., Macovski A.: Selection of a Convolution Function for Fourier Inversion Using Gridding. *IEEE Trans. Med. Imaging* (1991) 10: 473–478.
- Jackson J. I., Nishimura D. G., Macovski A.: Twisting Radial Lines with Application to Robust Magnetic Resonance Imaging of Irregular Flow. *Magn. Reson. Med.* (1992) 25: 128–139.
- Jelicks L. A., Gupta R. K.: Multinuclear NMR Studies of the Langendorff Perfused Rat Heart. *J. Biol. Chem.* (1989) 264: 15230–15235.
- Jelicks L. A., Gupta R. K.: On the Extracellular Contribution to Multiple Quantum Filtered  $^{23}\text{Na}$  NMR of Perfused Rat Heart. *Magn. Reson. Med.* (1993) 29: 130–133.
- Jones S. C., Kharlamov A., Yanovski B., Kim D. K., Easley K. A., Yushmanov V. E., Ziolkowski S. K., Boada F. E.: Stroke onset time using sodium MRI in rat focal cerebral ischemia. *Stroke* (2006) 37: 883–888.
- Kjemp-Harper R., Styles P., Wimperis S.: Three-Dimensional Triple-Quantum Filtration  $^{23}\text{Na}$  NMR Imaging. *J. Magn. Reson.* (1995) 108: 280–284.
- Kratzer F. J., Flassbeck S., Nagel A. M., Behl N. G. R., Knowles B. R., Bachert P., Ladd M. E., Schmitter S.: Sodium relaxometry using  $^{23}\text{Na}$  MR fingerprinting: a proof of concept. *Magn. Reson. Med.* (2020) 84: 2577–2591.
- Kratzer F. J., Flassbeck S., Schmitter S., Wilferth T., Magill A. W., Knowles B. R., Platt T., Bachert P., Ladd M. E., Nagel A. M.: 3D sodium ( $^{23}\text{Na}$ ) magnetic resonance fingerprinting for time-efficient relaxometric mapping. *Magn. Reson. Med.* (2021) 00: 1–14.
- Lachner S., Ruck L., Niesporek S. C., Utzschneider M., Lott J., Hensel B., Dörfler A., Uder M., Nagel A. M.: Comparison of optimized intensity correction methods for  $^{23}\text{Na}$  MRI of the human brain using a 32-channel phased array coil at 7 Tesla. *Z. Med. Phys.* (2020)

30: 104–115.

Lachner S., Utzschneider M., Zaric O., Minarikova L., Ruck L., Zbýň Š., Hensel B., Trattinig S., Uder M., Nagel A. M.: Compressed sensing and the use of phased array coils in  $^{23}\text{Na}$  MRI: a comparison of a SENSE-based and an individually combined multi-channel reconstruction. *Z. Med. Phys.* (2020) 31: 48–57.

Lachner S., Zaric O., Utzschneider M., Minarikova L., Zbýň Š., Hensel B., Trattinig S., Uder M., Nagel A. M.: Compressed sensing reconstruction of 7 Tesla  $^{23}\text{Na}$  multi-channel breast data using  $^1\text{H}$  MRI constraint. *Magn. Reson. Imaging* (2019) 60: 145–156.

Lauterbur P. .: Image Formation by Induced Local Interactions: Examples Employing Nuclear Magnetic Resonance. *Nature* (1973) 242: 190–191.

Levitt M. H.: *Spin dynamics: Basics of Nuclear Magnetic Resonance* (2008) John Wiley & Sons, Ltd.

Liao J. R., Pauly J. M., Brosnan T. J., Pelc N. J.: Reduction of Motion Artifacts in Cine MRI Using Variable-Density Spiral Trajectories. *Magn. Reson. Med.* (1997) 37: 569–575.

Lu A., Atkinson I. C., Claiborne T. C., Damen F. C., Thulborn K. R.: Quantitative sodium imaging with a flexible twisted projection pulse sequence. *Magn. Reson. Med.* (2010) 63: 1583–1593.

Lustig M., Donoho D. L., Santos J. M., Pauly J. M.: Compressed sensing MRI. *IEEE Signal Process. Mag.* (2008) 25: 72–82.

Lustig M., Donoho D., Pauly J. M.: Sparse MRI: the application of compressed sensing for rapid MR imaging. *Magn. Reson. Med.* (2007) 58: 1182–1195.

Madelin G., Chang G., Otazo R., Jerschow A., Regatte R. R.: Compressed sensing sodium MRI of cartilage at 7T : Preliminary study. *J. Magn. Reson.* (2012) 214: 360–365.

Madelin G., Lee J.-S., Inati S., Jerschow A., Regatte R. R.: Sodium inversion recovery MRI of the knee joint in vivo at 7T. *J. Magn. Reson.* (2010) 207: 42–52.

Madelin G., Lee J.-S., Regatte R. R., Jerschow A.: Sodium MRI: methods and applications. *Prog. Nucl. Magn. Reson. Spectrosc.* (2014) 79: 14–47.

Madelin G., Xia D., Brown R., Babb J., Chang G., Krasnokutsky S., Regatte R. R.: Longitudinal study of sodium MRI of articular cartilage in patients with knee osteoarthritis: initial experience with 16-month follow-up. *Eur. Radiol.* (2018) 28: 133–

142.

- Mansfield P., Grannel P. K.: NMR “diffraction” in solids? *J. Phys. C Solid State Phys.* (1973) 6: L422–L426.
- Marques J. P., Kober T., Krueger G., van der Zwaag W., Van de Moortele P. F., Gruetter R.: MP2RAGE, a self bias-field corrected sequence for improved segmentation and T1-mapping at high field. *Neuroimage* (2010) 49: 1271–1281.
- Marseille G. J., De Beer R., Fuderer M., Mehlkopf A. F., Van Ormondt D.: Nonuniform phase-encode distributions for MRI scan time reduction. *J. Magn. Reson. - Ser. B* (1996) 111: 70–75.
- McLachlan A. D.: Line widths of electron resonance spectra in solution. *Proc. R. Soc. Lond. A* (1964) 280: 271–288.
- Mellon E. A., Pilkinton D. T., Clark C. M., Elliott M. A., Witschey W. R., Borthakur A., Reddy R.: Sodium MR Imaging Detection of Mild Alzheimer Disease: Preliminary Study. *Am. J. Neuroradiol.* (2009) 30: 978–984.
- Mirkes C., Shajan G., Bause J., Buckenmaier K., Hoffmann J., Scheffler K.: Triple-quantum-filtered sodium imaging at 9.4 Tesla. *Magn. Reson. Med.* (2016) 75: 1278–1289.
- Morrell G. R.: A Phase-Sensitive Method of Flip Angle Mapping. *Magn. Reson. Med.* (2008) 60: 889–894.
- Müller N., Bodenhausen G., Ernst R. R.: Relaxation-Induced Violations of Coherence Transfer Selection Rules in Nuclear Magnetic Resonance. *J. Magn. Reson.* (1987) 75: 297–334.
- Nagel A. M., Amarteifio E., Lehmann-Horn F., Jurkat-Rott K., Semmler W., Schad L. R., Weber M. A.: 3 Tesla Sodium Inversion Recovery Magnetic Resonance Imaging Allows for Improved Visualization of Intracellular Sodium Content Changes in Muscular Channelopathies. *Invest. Radiol.* (2011) 46: 759–766.
- Nagel A. M., Bock M., Hartmann C., Gerigk L., Neumann J. O., Weber M. A., Bendszus M., Radbruch A., Wick W., Schlemmer H. P., Semmler W., Biller A.: The potential of relaxation-weighted sodium magnetic resonance imaging as demonstrated on brain tumors. *Invest. Radiol.* (2011) 46: 539–547.
- Nagel A. M., Laun F. B., Weber M. A., Matthies C., Semmler W., Schad L. R.: Sodium MRI using a density-adapted 3D radial acquisition technique. *Magn. Reson. Med.* (2009) 62:

- 1565–1573.
- Nagel A. M., Lehmann-Horn F., Weber M.-A., Jurkat-Rott K., Wolf M. B., Radbruch A., Umathum R., Semmler W.: In Vivo  $^{35}\text{Cl}$  MR Imaging in Humans: A Feasibility Study. *Radiology* (2014) 271: 585–595.
- Naritomi H., Kanashiro M., Sasaki M., Kuribayashi Y., Sawada T.: In vivo measurements of intra- and extracellular  $\text{Na}^+$  and water in the brain and muscle by nuclear magnetic resonance spectroscopy with shift reagent. *Biophys. J.* (1987) 52: 611–616.
- Niellès-Vallespin S., Weber M. A., Bock M., Bongers A., Speier P., Combs S. E., Wöhrle J., Lehmann-Horn F., Essig M., Schad L. R.: 3D radial projection technique with ultrashort echo times for sodium MRI: Clinical applications in human brain and skeletal muscle. *Magn. Reson. Med.* (2007) 57: 74–81.
- Niesporek S. C., Hoffmann S. H., Berger M. C., Benkhedah N., Kujawa A., Bachert P., Nagel A. M.: Partial volume correction for in vivo  $^{23}\text{Na}$ -MRI data of the human brain. *Neuroimage* (2015) 112: 353–363.
- Nishimura D. G.: *Principles of magnetic resonance imaging* (2010) Stanford Univ.
- Pipe J. G., Menon P.: Sampling Density Compensation in MRI: Rationale and an Iterative Numerical Solution. *Magn. Reson. Med.* (1999) 41: 179–186.
- Pipe J. G., Zwart N. R., Aboussouan E. A., Robison R. K., Devaraj A., Johnson K. O.: A new design and rationale for 3D orthogonally oversampled k-space trajectories. *Magn. Reson. Med.* (2011) 66: 1303–1311.
- Platt T., Umathum R., Fiedler T. M., Nagel A. M., Bitz A. K., Maier F., Bachert P., Ladd M. E., Wielpütz M. O., Kauczor H. U., Behl N. G. R.: In vivo self-gated  $^{23}\text{Na}$  MRI at 7 T using an oval-shaped body resonator. *Magn. Reson. Med.* (2018) 80: 1005–1019.
- Purcell E. M., Torrey H. C., Pound R. V.: Resonance Absorption by Nuclear Magnetic Moments in a Solid. *Phys. Rev.* (1946) 69: 37–38.
- Rabi I. I.: Space Quantization in a Gyating Magnetic Field. *Phys. Rev.* (1937) 51: 652–654.
- Rabi I. I., Zacharias J. R., Millman S., Kusch P.: A new method of measuring Nuclear Magnetic Moment. *Phys. Rev.* (1938) 53: 318.
- Rasche V., Proksa R., Sinkus R., Börnert P., Eggers H.: Resampling of Data Between Arbitrary Grids Using Convolution Interpolation. *IEEE Trans. Med. Imaging* (1999) 18: 385–392.

## REFERENCES

---

- Reetz K., Romanzetti S., Dogan I., Saß C., Werner C. J., Schiefer J., Schulz J. B., Shah N. J.: Increased brain tissue sodium concentration in Huntington's Disease - A sodium imaging study at 4T. *Neuroimage* (2012) 63: 517–524.
- Regnery S., Behl N. G. R., Platt T., Weinfurter N., Windisch P., Deike-Hofmann K., Sahm F., Bendszus M., Debus J., Ladd M. E., Schlemmer H. P., Rieken S., Adeberg S., Paech D.: Ultra-high-field sodium MRI as biomarker for tumor extent, grade and IDH mutation status in glioma patients. *NeuroImage Clin.* (2020) 28: 102427.
- Riemer F., Solanky B. S., Stehning C., Clemence M., Wheeler-Kingshott C. A. M., Golay X.: Sodium ( $^{23}\text{Na}$ ) Ultra-Short Echo Time Imaging in the Human Brain Using a 3D-Cones Trajectory. *Magn. Reson. Mater. Physics, Biol. Med.* (2014) 27: 35–46.
- Romanzetti S., Mirkes C. C., Fiege D. P., Celik A., Felder J., Shah N. J.: Mapping Tissue Sodium Concentration in the Human Brain: A Comparison of MR Sequences at 9.4 Tesla. *Neuroimage* (2014) 96: 44–53.
- Rooney W. D., Springer C. S. J.: A comprehensive approach to the analysis and interpretation of the resonances of spins  $3/2$  from living systems. *NMR Biomed.* (1991) 4: 209–226.
- Rose A. M., Valdes R.: Understanding the sodium pump and its relevance to disease. *Clin. Chem.* (1994) 40: 1674–1685.
- Rudin L. I., Osher S., Fatemi E.: Nonlinear total variation based noise removal algorithms. *Phys. D Nonlinear Phenom.* (1992) 60: 259–268.
- Saff E. B., Kuijlaars A. B. J.: Distributing Many points on a Sphere. *Math. Intell.* (1997) 19: 5–11.
- Sandino C. M., Cheng J. Y., Chen F., Mardani M., Pauly J. M., Vasanawala S. S.: Compressed sensing: from research to clinical practice with deep neural networks. *IEEE Signal Process. Mag.* (2020) 37: 117–127.
- Seshan V., Sherry A. D., Bansal N.: Evaluation of Triple Quantum-Filtered  $^{23}\text{Na}$  NMR Spectroscopy in the in Situ Rat Liver. *Magn. Reson. Med.* (1997) 38: 821–827.
- Shah N. J., Worthoff W. A., Langen K. J.: Imaging of sodium in the brain: A brief review. *NMR Biomed.* (2016) 29: 162–174.
- Shymanskaya A., , Worthoff W. A., , Cleary J. O., , Blunck Y., , Glarin R. K., Kolbe S., , Johnston L., , Shah N. J.: Multiple Quantum Filtered Sodium MRI of Multiple Sclerosis

## REFERENCES

---

- at 7T. Proc. 36th Annu. Meet. ESMRM (2019).
- Shymanskaya A., Worthoff W. A., Stoffels G., Lindemeyer J., Neumaier B., Lohmann P., Galldiks N., Langen K.-J., Shah N. J.: Comparison of [18F]Fluoroethyltyrosine PET and Sodium MRI in Cerebral Gliomas: a Pilot Study. *Mol. Imaging Biol.* (2020) 22: 198–207.
- Slichter C. P.: *Principles of Magnetic Resonance* (1990) Springer.
- Sørensen O. W., Eich G. W., Levitt M. H., Bodenhausen G., Ernst R. R.: Product Operator Formalism for the Description of NMR Pulse Experiments. *Prog. Nucl. Magn. Reson. Spectrosc.* (1984) 16: 163–192.
- Staroswiecki E., Bangerter N. K., Gurney P. T., Grafendorfer T., Gold G. E., Hargreaves B. A.: In Vivo Sodium Imaging of Human Patellar Cartilage with a 3D Cones Sequence at 3T and 7T. *J. Magn. Reson. Imaging* (2010) 32: 446–451.
- Stirnberg R., Stöcker T., Shah N. J.: A New and Versatile Gradient Encoding Scheme for DTI: a Direct Comparison with the Jones Scheme. Proc. 17th Annu. Meet. ISMRM (2009).
- Stobbe R., Beaulieu C.: In vivo sodium magnetic resonance imaging of the human brain using soft inversion recovery fluid attenuation. *Magn. Reson. Med.* (2005) 54: 1305–1310.
- Tauskela J. S., Dizon J. M., Whang J., Katz J.: Evaluation of Multiple-Quantum-Filtered  $^{23}\text{Na}$  NMR in Monitoring Intracellular Na Content in the Isolated Perfused Rat Heart in the Absence of a Chemical-Shift Reagent. *J. Magn. Reson.* (1997) 127: 115–127.
- Thulborn K. R.: Quantitative sodium MR imaging: a review of its evolving role in medicine. *Neuroimage* (2018) 168: 250–268.
- Thulborn K. R., Gindin T. S., Davis D., Erb P.: Comprehensive MR imaging protocol for stroke management: tissue sodium concentration as a measure of tissue viability in nonhuman primate studies and in clinical studies. *Radiology* (1999) 213: 156–166.
- Thulborn K. R., Lu A., Atkinson I. C., Damen F., Villano J. L.: Quantitative sodium MR imaging and sodium bioscales for the management of brain tumors. In *Neuroimaging Clinics of North America* (Vol. 19, Issue 4, pp. 615–624) Elsevier Ltd.
- Umatham R., Rösler M. B., Nagel A. M.: In Vivo  $^{39}\text{K}$  MR Imaging of Human Muscle and Brain. *Radiology* (2013) 269: 569–576.
- Utzschneider M., Behl N. G. R., Lachner S., Gast L. V., Maier A., Uder M., Nagel A. M.: Accelerated quantification of tissue sodium concentration in skeletal muscle tissue:

- quantitative capability of dictionary learning compressed sensing. *Magn. Reson. Mater. Physics, Biol. Med.* (2020) 33: 495–505.
- Utzschneider M., Müller M., Gast L. V., Lachner S., Behl N. G. R., Maier A., Uder M., Nagel A. M.: Towards accelerated quantitative sodium MRI at 7 T in the skeletal muscle: comparison of anisotropic acquisition- and compressed sensing techniques. *Magn. Reson. Imaging* (2021) 75: 72–88.
- Van Der Maarel J. R. C.: Thermal relaxation and coherence dynamics of spin 3/2. I. Static and fluctuating quadrupolar interactions in the multipole basis. *Concepts Magn. Reson. Part A* (2003) 19A: 97–116.
- Wang S., Su Z., Ying L., Peng X., Zhu S., Liang F., Feng D., Liang D.: Accelerating magnetic resonance imaging via deep learning. *IEEE 13th Int. Symp. Biomed. Imaging* (2016) 514–517.
- Wang Z., Bovik A. C., Sheikh H. R., Simoncelli E. P.: Image quality assessment: from error visibility to structural similarity. *IEEE Trans. Image Process.* (2004) 13: 600–612.
- Wech T., Stäb D., Budich J. C., Fischer A., Tran-Gia J., Hahn D., Köstler H.: Resolution evaluation of MR images reconstructed by iterative thresholding algorithms for compressed sensing. *Med. Phys.* (2012) 39: 4328–4338.
- Weingärtner S., Wetterling F., Konstandin S., Fatar M., Neumaier-Probst E., Schad L. R.: Scan time reduction in <sup>23</sup>Na-Magnetic Resonance Imaging using the chemical shift imaging sequence: Evaluation of an iterative reconstruction method. *Z. Med. Phys.* (2015) 25: 275–286.
- Wheaton A. J., Borthakur A., Shapiro E. M., Regatte R. R., Akella S. V. S., Kneeland J. B., Reddy R.: Proteoglycan Loss in Human Knee Cartilage: Quantitation with Sodium MR Imaging—Feasibility Study. *Radiology* (2004) 231: 900–905.
- Wimperis S., Wood B.: Triple-Quantum Sodium Imaging. *J. Magn. Reson.* (1991) 95: 428–436.
- Winkelmann S., Schaeffter T., Koehler T., Eggers H., Doessel O.: An Optimal Radial Profile Order Based on the Golden Ratio for Time-resolved MRI. *IEEE Trans. Med. Imaging* (2007) 26: 68–76.
- Winkler S. S.: Sodium-23 magnetic resonance brain imaging. *Neuroradiology* (1990) 32: 416–420.

## REFERENCES

---

- Winter P. M., Seshan V., Makos J. D., Sherry A. D., Malloy C. R., Bansal N.: Quantitation of intracellular  $[Na^+]$  in vivo by using TmDOTP5- as an NMR shift reagent and extracellular marker. *J. Appl. Physiol.* (1998) 85: 1806–1812.
- Wood C. S., Bennett S. C., Cho D., Masterson B. P., Roberts J. L., Tanner C. E., Wieman C. E.: Measurement of Parity Nonconservation and an Anapole Moment in Cesium. *Science* (80-. ). (1997) 275: 1759–1763.
- Worthoff W. A., Shymanskaya A., Lindemeyer J., Langen K. J., Shah N. J.: Relaxometry and quantification in sodium MRI of cerebral gliomas: A FET-PET and MRI small-scale study. *NMR Biomed.* (2020) 33: e4361.
- Worthoff W. A., Shymanskaya A., Shah N. J.: Relaxometry and quantification in simultaneously acquired single and triple quantum filtered sodium MRI. *Magn. Reson. Med.* (2019) 81: 303–315.
- Zaric O., Juras V., Szomolanyi P., Schreiner M., Raudner M., Giraudo C., Trattnig S.: Frontiers of sodium MRI revisited: from cartilage to brain imaging. *J. Magn. Reson. Imaging* (2021) 54: 58–75.
- Zhao Y., Guo R., Li Y., Thulborn K. R., Liang Z. P.: High-resolution sodium imaging using anatomical and sparsity constraints for denoising and recovery of novel features. *Magn. Reson. Med.* (2021) 86: 625–636.
- Zhu J. -M, Smith I. C. P.: Selection of Coherence Transfer Pathways by Pulsed-Field Gradients in NMR Spectroscopy. *Concepts Magn. Reson.* (1995) 7: 281–291.
- Zimmermann M., Abbas Z., Dzieciol K., Shah N. J.: Accelerated Parameter Mapping of Multiple-Echo Gradient-Echo Data Using Model-Based Iterative Reconstruction. *IEEE Trans. Med. Imaging* (2018) 37: 626–637.
- Zöllner F. G., Konstandin S., Lommen J., Budjan J., Schoenberg S. O., Schad L. R., Haneder S.: Quantitative sodium MRI of kidney. *NMR Biomed.* (2016) 29: 197–205.



## LIST OF PUBLICATIONS

The work presented in this thesis has produced the following publications and conference presentations.

### Journal papers

- **Chen Q.**, Shah N. J., Worthoff W. A.: Compressed Sensing in Sodium Magnetic Resonance Imaging: Techniques, Applications, and Future Prospects. *J. Magn. Reson. Imaging* (2022) 55: 1340–1356.
- **Chen Q.**,\* Worthoff W. A.,\* Shah N. J.: Accelerated multiple-quantum-filtered sodium magnetic resonance imaging using compressed sensing at 7 T. *Magn. Reson. Imaging* (2024) 107: 138–148.

### Conference abstracts

- **Chen Q.**, Worthoff W. A., Shah N. J.: Accelerated Enhanced Simultaneous Single-Quantum and Triple-Quantum-Filtered Sodium MRI Using Compressed Sensing at 7T. Proceedings of the 31st Annual Meeting of ISMRM (2023), Toronto, Canada.
- **Chen Q.**, Worthoff W. A., Shah N. J.: Triple-Quantum-Filtered Sodium MRI at 7T : Optimization of the Enhanced SISTINA Sequence Using FLORET k-space Trajectories. Proceedings of the 29th Annual Meeting of ISMRM (2021), Online.
- Worthoff W. A., **Chen Q.**, Filss C., Abbas Z., Langen K.-J., Shah N. J.: Advancing Brain Tumour Sodium Imaging: Prospectively Accelerated eSISTINA and Compressed Sensing at 7T. Proceedings of the 32nd Annual Meeting of ISMRM (2024), Singapore.
- Worthoff W. A., **Chen Q.**, Shah N. J.: Optimisation of Simultaneously Acquired Single and Triple Quantum Filtered Sodium MRI for Relaxometry at 7T. Proceedings of the 31st Annual Meeting of ISMRM (2023), Toronto, Canada.

\* The authors should be considered co-first authors.



### ACKNOWLEDGEMENTS

First and foremost, I am indebted to my outstanding supervisor, Prof. N. J. Shah, without whose guidance and support, I would not have been able to get this far. I am incredibly grateful to Prof. Shah for making all this possible by kindly allowing me to join the excellent and reputable MR Physics group in INM-4 in July 2019. I am very fortunate to have such a distinguished and admirable scientist training me in various aspects of MRI. Prof. Shah, thank you for your continuous support and immense generosity and for imparting your wealth of knowledge!

I would like to offer my deepest gratitude to my group leader, Dr. W. A. Worthoff, for his excellent supervision, thoughtful discussions and endless support. Thank you for your invaluable guidance through this challenging time, especially during the COVID-19 pandemic and for your tenacity in encouraging me to achieve my goals – Wieland, you are a brilliant supervisor!

My sincere thanks to Prof. L. Johnston and Dr. Y. Blunck from Australia for their strong support, constructive suggestions and enthusiastic encouragement. I would like to thank the Jülich – University of Melbourne Postgraduate Academy (JUMPA) for the financial support of my doctoral research.

I would like to express my great thanks my colleagues for their helpful scientific discussions: Dr. A. Shymanskaya, Dr. Z. Abbas, Dr. M. Zimmermann, Dr. S. D. Yun, Dr. H. Sbailhat, Dr. F. Kueppers, Dr. C.-H. Choi, Mr D. Thomas, and many more in FZ Jülich. Deep thanks go out to the MTRA team, especially to Ms A. Köth, Ms E. Bechholz and Ms P. Engels, for supporting me with the 7T measurements. Additional thanks go to Ms C. Roß, Ms W. Fladung, Ms C. Rick and Ms N. Malsbenden for their incredible administrative support.

I sincerely thank my family for their unwavering support, unconditional love and infinite belief in me during my long academic path – special thanks to my parents for giving me sufficient intelligence to study MRI.

Last but not the least, to my husband, Mr. Shangzhe YU: LOVE YOU.



**AFFIDAVIT REGARDING DATA RETENTION**

**Affidavit according to § 5 (1) for Data Retention**

I hereby declare that the original data forming the basis of this doctoral thesis are stored with my supervisor, Prof. Dr. N. Jon Shah, head of the Institute of Neuroscience and Medicine (INM-4), Forschungszentrum Jülich.

Qingping Chen



## AFFIDAVIT REGARDING ONE'S OWN CONTRIBUTION

---

### AFFIDAVIT REGARDING ONE'S OWN CONTRIBUTION

#### Affidavit according to § 5 (1) § 11 (3) 12 of the doctoral studies regulations

I, **Qingping Chen**, hereby declare on oath that I independently collected and prepared the following results portrayed in the dissertation “**Development and Implementation of Accelerated Multiple-Quantum-Filtered Sodium Magnetic Resonance Imaging Using Compressed Sensing at Ultra-High Field**”.

I had the following assistance with completing the dissertation. These are listed in the acknowledgments.

Names→	Qingping Chen	Dr. Wieland A. Worthoff	Prof. Dr. N. Jon Shah	Sum (%)
Study supervision		60	40	100
Study design/conception	20	40	40	100
Phantom production and volunteer recruitment	60	40		100
Sequence implementation	60	40		100
Data acquisition	60	40		100
Data analysis	60	40		100
Writing/draft	100			100

---

Signature of the doctoral candidate

As the supervisor of the above dissertation, I confirm the statements of Qingping Chen.

---

Signature of the doctoral supervisor





CURRICULUM VITAE

**Qingping CHEN**

❖ **Scientific Researcher**, Division of Medical Physics, Department of Radiology, University Medical Centre Freiburg, Freiburg, Germany **03.2023 – Present**

**Project:** “Open-Source, Vendor-Independent Sequence Development and Image Reconstruction Based on the Pulseseq Framework”

❖ **PhD studies at Medical Imaging Physics**, Institute of Neuroscience and Medicine – 4, Forschungszentrum Jülich, Jülich, Germany & Faculty of Medicine, RWTH Aachen University, Aachen, Germany **07.2019 – 02.2023**

**Thesis:** “Development and Implementation of Accelerated Multiple-Quantum-Filtered Sodium Magnetic Resonance Imaging Using Compressed Sensing at Ultra-High Field”

❖ **Master of Neurobiology**, Institute of Biophysics, University of Chinese Academy of Sciences, Beijing, China (double degree) **09.2016 – 06.2019**

❖ **Master of Neuroscience and Neuroimaging**, Faculty of Science and Technology, Aarhus University, Aarhus, Denmark (double degree) **09.2016 – 10.2018**

**Thesis:** “Sodium Magnetic Resonance Imaging Using Spiral Trajectories at Ultra-high Field” (Thesis grade: 12/12)

❖ **Academic Exchange**, Danish Research Centre for Magnetic Resonance & Technical University of Denmark, Copenhagen, Denmark **02.2018 – 04.2018**

**Project:** “Simulation of a 2D Spiral UTE Sequence Using Jülich Extensible MRI Simulator (JEMRIS)”

❖ **Bachelor of Biomedical Engineering**, Department of Electronic Engineering, Fudan University, Shanghai, China **09.2012 – 06.2016**